

**An Analysis of Star Formation in M31 Using Resolved
Stars and Ultraviolet Flux**

A DISSERTATION
SUBMITTED TO THE FACULTY OF THE GRADUATE SCHOOL
OF THE UNIVERSITY OF MINNESOTA
BY

Jacob E. Simones

IN PARTIAL FULFILLMENT OF THE REQUIREMENTS
FOR THE DEGREE OF
Doctor of Philosophy

Evan D. Skillman, Advisor

October, 2014

© Jacob E. Simones 2014
ALL RIGHTS RESERVED

Acknowledgements

I thank my adviser, Evan Skillman, for all of his time and effort spent guiding me to my PhD. He has provided me with many wonderful opportunities that have truly enriched my graduate school experience. I have met great people, traveled to exciting places, and worked on interesting projects all because of him, and I cannot imagine how my trajectory would be different had he not accepted me as a student so many years ago. He always has great advice, both academic and on life. Without the latter, this dissertation may never have been written. Above all, Evan is a patient and understanding person, and it has been a pleasure working for him. Plus, he's a riot at dinner.

I must also thank my graduate comrades, both those who are sill toiling away and those who have moved on to better things. Graduate school is not for the faint of heart, but good laughs and lots of beer make it easier. The friends I have made over the years have been vital for balancing the bad with the good, and have made this whole experience worth something more than just attaining a degree.

For my parents, words simply cannot express my love and gratitude. While I was growing up, Mom and Dad both taught me the importance of education and I always knew they expected me to go to college. However, I never felt pressured to pursue any given profession. They allowed me to discover myself on my own terms and actively fostered my interests, even when my interests were borderline ridiculous. (Remember when I thought I wanted to be a rockstar?) As for most young adults, life got hard when I started college, and even more so when I started graduate school. I quickly discovered my limits, that there is only so much I can do on my own, and my parents have helped me out on countless occasions along the way, allowing me to focus on my studies. The only reason I have made it this far is with their constant, unconditional support.

I give my most heartfelt thanks to my wife, Annie, who, for better or worse, has

stuck with me on this trying journey. I remember when we both started our professional studies. We were mostly care-free and could not have been happier chasing our ultimate academic goals – and we had no idea what challenges were ahead of us. The hours slowly grew longer, the dinners less frequent, and the stress became heavy. I even got my first gray hairs. Yet Annie has been there for me through all of it. She always made me feel better after a bad exam and shared my joy in my successes, and she is still the person I most look forward to seeing at the end of the day (and I miss her when I don't). She always inspired me to keep going and provided words of encouragement when I needed it – except when she didn't. After all, she has never been afraid to force me to think about what I really want in life and sometimes that meant having difficult conversations. Deep down she is pragmatic and I like her for that, too, because she makes me a better person. We have been through so much together and finally earning my degree is as much her victory as it is mine. She is my equal, my best friend, and the love of my life.

Dedication

For Annie – here's to what's next.

Abstract

We have used optical observations of resolved stars from the Panchromatic Hubble Andromeda Treasury (PHAT) to measure the recent (< 500 Myr) star formation histories (SFHs) of 33 FUV-bright regions in M31. The region areas ranged from $\sim 10^4$ to 10^6 pc 2 , which allowed us to test the reliability of FUV flux as a tracer of recent star formation on sub-kpc scales. The star formation rates (SFRs) derived from the extinction-corrected observed FUV fluxes were, on average, consistent with the 100-Myr mean SFRs of the SFHs to within the 1σ scatter. Overall, the scatter was larger than the uncertainties in the SFRs and particularly evident among the smallest regions. The scatter was consistent with an even combination of discrete sampling of the initial mass function and high variability in the SFHs. This result demonstrates the importance of satisfying both the full-IMF and the constant-SFR assumptions for obtaining precise SFR estimates from FUV flux. Assuming a robust FUV extinction correction, we estimate that a factor of 2.5 uncertainty can be expected in FUV-based SFRs for regions smaller than 10^5 pc 2 , or a few hundred pc. We also examined ages and masses derived from UV flux under the common assumption that the regions are simple stellar populations (SSPs). The SFHs showed that most of the regions are not SSPs, and the age and mass estimates were correspondingly discrepant from the SFHs. For those regions with SSP-like SFHs, we found mean discrepancies of 10 Myr in age and a factor of 3 to 4 in mass. It was not possible to distinguish the SSP-like regions from the others based on integrated FUV flux.

Starting from SFHs derived from the full PHAT photometric dataset, we have used stellar population synthesis to create maps of synthetic far- and near-ultraviolet (FUV and NUV) flux at sub-kpc resolution for the northeast quadrant of M31. The synthetic maps reproduced all of the main morphological features found in corresponding maps of observed FUV and NUV flux, including rings and large star-forming complexes. Comparing the flux maps pixel-by-pixel, we found the median synthetic-to-observed flux ratios to be $1.02 \pm 0.74/-0.43$ in FUV and $0.79 \pm 0.35/-0.24$ in NUV. The synthetic fluxes were therefore consistent overall with the observed fluxes in both filters. We used the observed fluxes and standard flux calibrations to derive star formation rate (SFR)

maps, which we compared with a map of the mean SFRs over the last 100 Myr of the star formation histories (SFHs). We determined a lower limit of $\text{SFR} \sim 10^{-5} M_{\odot} \text{ yr}^{-1}$ below which the commonly assumed linear relationship between UV flux and SFR appears to break down. Above this limit, we found the median ratios of the flux-based SFRs to the mean SFRs to be $0.57 +0.47/-0.26$ in FUV and $1.24 +0.88/-0.52$ in NUV. Both the FUV and NUV flux-based SFRs were therefore consistent overall with the mean SFRs derived from the SFHs. Integrating over the entire mean SFR map, we found a global SFR of $0.3 M_{\odot} \text{ yr}^{-1}$. The corresponding measurements from the flux-based SFR maps were factors of 0.74 (FUV) and 1.45 (NUV) of the global mean SFR value. It is not yet understood why the SFR ratios in the global case are larger than the median pixel-wise ratios. The primary source of uncertainty in both the synthetic flux maps and the flux-based SFR maps was most likely incomplete IMF sampling due to the small pixel areas. With the exception of the faintest areas of the galaxy, we did not identify any trends for flux or SFR with environment.

Contents

Acknowledgements	i
Dedication	iii
Abstract	iv
List of Tables	ix
List of Figures	x
1 Introduction	1
1.1 Evaluating ultraviolet flux as a star formation tracer on sub-kpc scales	1
1.2 From sub-kpc to galactic-scales: evaluating ultraviolet flux using synthetic ultraviolet flux maps of M31	2
2 The Panchromatic Hubble Andromeda Treasury. VI. The reliability of far-ultraviolet flux as a star formation tracer on sub-kpc scales (Simones et al., 2014).	5
2.1 Introduction	6
2.2 Observations and photometry	8
2.2.1 UV-Bright Regions in M31	8
2.2.2 PHAT photometry	12
2.2.3 Artificial star tests	14
2.3 The recent SFHs of UV-bright regions in M31	14
2.3.1 CMD modeling with MATCH	14

2.3.2	Extinction model	16
2.3.3	Results	18
2.3.4	Uncertainties	24
2.4	UV flux modeling	25
2.5	SFR estimates	28
2.6	Discussion	32
2.6.1	FUV magnitudes	32
2.6.2	SFR estimates from FUV flux	36
2.6.3	SSP ages and masses	39
2.7	Conclusion	42
3	Synthetic ultraviolet flux maps of M31 from resolved optical photometry.	45
3.1	Introduction	46
3.2	Synthetic UV flux maps	47
3.2.1	The spatially-resolved star formation history of M31	47
3.2.2	Broadband UV flux modeling	48
3.3	Observations	55
3.4	SFR estimates	55
3.5	Discussion	61
3.5.1	Modeled flux	61
3.5.2	SFR estimates from FUV flux	65
3.6	Conclusion	72
4	Summary	76
4.1	Tracing star formation with ultraviolet flux: results from sub-kpc regions	76
4.2	Modeling ultraviolet flux on sub-kpc scales and galactic scales simultaneously	78
4.3	Future work	80
4.3.1	More precise quantification and attribution of uncertainties	80
4.3.2	Putative flux ratio and SFR ratio outliers	81
4.3.3	Synthetic flux and flux-based SFR uncertainties as a function of scale	82

4.3.4	Synthetic flux and flux-based SFR uncertainties as a function of environment	82
4.3.5	Infrared flux as a test of dust emission models and as a SFR indicator	82
Bibliography		87

List of Tables

2.1	Observational properties of UV-bright regions in PHAT Brick 15.	11
2.1	Observational properties of UV-bright regions in PHAT Brick 15.	12
2.2	Region properties derived from the SFHs.	23
2.2	Region properties derived from the SFHs.	24
2.3	FUV and NUV magnitudes modeled from the SFHs.	27
2.3	FUV and NUV magnitudes modeled from the SFHs.	28
2.4	SFRs, ages, and masses from FUV and NUV fluxes.	31
2.4	SFRs, ages, and masses from FUV and NUV fluxes.	32
3.1	Filter constants and image names.	51

List of Figures

2.1	Two-color composite mosaic of M31 from the GALEX Deep Imaging Survey.	8
2.2	Closeup of Brick 15.	9
2.3	Optical color-magnitude diagrams of the UV-bright regions.	13
2.4	Observed CMD of region 4339, with the best-fit modeled CMD and the residual significance.	16
2.5	SFHs of UV-bright regions in M31.	20
2.5	<i>Cont.</i>	21
2.5	<i>Cont.</i>	22
2.6	The difference between the modeled reddened and observed FUV magnitudes versus deprojected area.	29
2.7	The log ratio of the FUV flux-based SFRs to the 100 Myr mean SFR of the SFHs versus deprojected region area.	33
2.8	The log ratio of the SSP masses based on UV color and luminosity to the total mass formed over the last 100 Myr of the SFHs versus deprojected region area.	40
3.1	PHAT survey map.	49
3.2	FUV flux map modeled from the SFHs.	53
3.3	NUV flux map modeled from the SFHs.	54
3.4	Observed and synthetic attenuated FUV flux maps.	56
3.5	Observed and synthetic attenuated NUV flux maps.	57
3.6	SFR maps from estimates based on observed fluxes compared with the mean SFR map from the SFHs.	59
3.7	SFR maps from estimates based on synthetic intrinsic fluxes compared with the mean SFR map from the SFHs.	60

3.8	Ratio of the synthetic flux to the observed flux in the FUV filter.	62
3.9	Ratio of the synthetic flux to the observed flux in the NUV filter.	63
3.10	Ratio of the SFR based on the observed extinction-corrected FUV flux to the 100 Myr mean SFR.	67
3.11	Ratio of the SFR based on the observed extinction-corrected NUV flux to the 100 Myr mean SFR.	68
3.12	Ratio of the SFR based on the synthetic intrinsic FUV flux to the 100 Myr mean SFR.	70
3.13	Ratio of the SFR based on the synthetic intrinsic NUV flux to the 100 Myr mean SFR.	71
4.1	Two-dimensional prototype sample.	83

Chapter 1

Introduction

1.1 Evaluating ultraviolet flux as a star formation tracer on sub-kpc scales

A common technique for estimating global star formation rates (SFRs) in individual galaxies is to measure the total flux at wavelengths known to trace recent star formation (SF), such as ultraviolet (UV) emission from intermediate- and high-mass stars. After correcting for dust extinction, an observed flux can be converted into a SFR using a suitable calibration, which is typically a linear scaling of intrinsic luminosity derived from population synthesis modeling. The modeling process requires a set of stellar evolution models and a stellar initial mass function (IMF), as well as a characterization of the star formation history (SFH; the evolution of SFR over time) and the metallicity of the population. These quantities are often not well-constrained for a given system and need to be assumed (see reviews by Kennicutt 1998, Kennicutt & Evans 2012, and references therein).

A set of flux calibrations widely used in extragalactic studies were presented by Kennicutt (1998, see Kennicutt & Evans, 2012 for updates). These calibrations are based on models of a generic population with solar metallicity, a fully populated IMF, and a SFR that has been constant over the lifetime of the tracer emission (~ 100 Myr for UV). The flux calibrations are therefore applicable to any population that can be assumed to approximate the generic population, such as spiral galaxies. In environments

with low total SF (i.e., low mass) or on subgalactic scales, however, the assumptions of a fully populated IMF and a constant SFR start to become tenuous. As a result, applying the flux calibrations in these situations can lead to inaccurate SFR estimates.

For populations located within a few Mpc, it is possible to measure SFRs more directly by fitting the color magnitude diagram (CMD) of the resolved stars to obtain a SFH (Dolphin, 2002). At its core, CMD fitting is a population synthesis technique just like flux calibration (albeit much more complex) and thus requires a set of stellar evolution models, an IMF, and an accounting of dust. The primary advantage of CMD fitting over the flux calibration method for obtaining SFRs, however, is the elimination of assumptions about the SFH and metallicity. CMD-based SFHs thus provide a relative standard for testing the accuracy of SFR estimates from commonly used flux calibrations, especially in applications where the underlying full-IMF and constant-SFR assumptions are not strictly satisfied. More generally, the SFHs can be used to test results from any other flux-based method, such as ages and masses derived under the simple stellar population (SSP) assumption.

With recent Hubble Space Telescope (HST) observations from the Panchromatic Hubble Andromeda Treasury (PHAT; Dalcanton et al., 2012), we have measured the recent SFHs (< 500 Myr) of 33 UV-bright regions in M31 and compared them with SFRs derived from UV flux. We also compared the SFHs with ages and masses derived from UV flux by treating the regions as SSPs. The UV-bright regions were cataloged by Kang et al. (2009, K09 hereafter) using Galaxy Evolution Explorer (GALEX) far-UV (FUV, $\lambda \sim 1540$ Å) flux and have areas ranging from 10^4 to 10^6 pc 2 . This range of sizes allowed us to test the reliability of the full-IMF, constant-SFR, and SSP assumptions on sub-kpc scales.

1.2 From sub-kpc to galactic-scales: evaluating ultraviolet flux using synthetic ultraviolet flux maps of M31

M31 is a well-studied, $\sim L_*$ galaxy and has been observed at a variety of wavelengths, e.g., in the ultraviolet (UV) by the Galaxy Evolution Explorer (GALEX; Morrissey et al., 2007), in the optical, including H α , for the Local Group Galaxies Survey (Massey et al., 2006), and in the infrared by the Spitzer Space Telescope (Gordon et al., 2006).

The wealth of high-quality data available for M31 provides a valuable opportunity to model various observations and test our current understanding of stellar astrophysics. In particular, the initial mass function (IMF), stellar evolution and spectra models, and extinction curves are all required to model the light produced by a galaxy.

A critical ingredient for modeling the flux from a galaxy is a detailed knowledge of its underlying SFH. Deriving SFHs by CMD analysis is a reliable method that can be used whenever photometry of resolved stars is available. An extensive optical photometric catalog for M31 has been compiled by PHAT (Dalcanton et al., 2012), and Lewis et al. (2014) have used these data to derive the spatially-resolved SFH of the northeast quadrant. With sub-kpc resolution, this SFH dataset is the ideal input for stellar population synthesis codes that model total flux given a population’s SFR and metallicity evolution. The result is a set of spatially-resolved maps of synthetic broadband flux in M31 which can be compared with observations.

The Lewis et al. (2014) SFHs can also be used to create temporally-averaged SFR maps. Because the SFHs were derived from the resolved stars without any prior assumptions about the SFHs, such maps provide a standard against which flux-based SFR estimates (e.g., using any of the calibrations from Kennicutt & Evans, 2012) can be tested. Using integrated flux to estimate SFRs for distant galaxies, where resolved stars are not available, is a common technique in extragalactic astronomy. Previous studies have investigated how flux-based SFR estimators hold up against resolved-star SFHs in sub-kpc UV-bright regions (Simones et al., 2014) and in low-metallicity dwarf galaxies (McQuinn et al., 2014). The SFHs of Lewis et al. (2014) based on data from PHAT make it possible to broaden this type of analysis to include a wide variety of environments in the most prominent local group spiral galaxy.

In this study, we have used the PHAT CMD-based SFHs and stellar population synthesis to create maps of synthetic ultraviolet (UV) flux at sub-kpc resolution for the northeast quadrant of M31. We then compared the synthetic flux maps with observations from GALEX. We have only focused on GALEX FUV and NUV (far and near UV), though this work can easily be extended to other wavelength regimes. In §3.2, we describe the SFH dataset and the production of the synthetic flux maps. §3.3 describes the process of producing observed flux maps from GALEX FUV and NUV images. The creation of SFR maps both from the SFHs and the observed fluxes using

common flux-SFR calibrations are described in §3.4. In §3.5, we compare the synthetic maps with the observations and compare mean SFR maps with SFRs estimated from observed flux. We conclude in §3.6.

Chapter 2

The Panchromatic Hubble Andromeda Treasury. VI. The reliability of far-ultraviolet flux as a star formation tracer on sub-kpc scales (Simones et al., 2014).

Abstract

We have used optical observations of resolved stars from the Panchromatic Hubble Andromeda Treasury (PHAT) to measure the recent (< 500 Myr) star formation histories (SFHs) of 33 FUV-bright regions in M31. The region areas ranged from $\sim 10^4$ to 10^6 pc 2 , which allowed us to test the reliability of FUV flux as a tracer of recent star formation on sub-kpc scales. The star formation rates (SFRs) derived from the extinction-corrected observed FUV fluxes were, on average, consistent with the 100-Myr mean SFRs of the SFHs to within the 1σ scatter. Overall, the scatter was larger than

the uncertainties in the SFRs and particularly evident among the smallest regions. The scatter was consistent with an even combination of discrete sampling of the initial mass function and high variability in the SFHs. This result demonstrates the importance of satisfying both the full-IMF and the constant-SFR assumptions for obtaining precise SFR estimates from FUV flux. Assuming a robust FUV extinction correction, we estimate that a factor of 2.5 uncertainty can be expected in FUV-based SFRs for regions smaller than 10^5 pc^2 , or a few hundred pc. We also examined ages and masses derived from UV flux under the common assumption that the regions are simple stellar populations (SSPs). The SFHs showed that most of the regions are not SSPs, and the age and mass estimates were correspondingly discrepant from the SFHs. For those regions with SSP-like SFHs, we found mean discrepancies of 10 Myr in age and a factor of 3 to 4 in mass. It was not possible to distinguish the SSP-like regions from the others based on integrated FUV flux.

2.1 Introduction

A common technique for estimating global star formation rates (SFRs) in individual galaxies is to measure the total flux at wavelengths known to trace recent star formation (SF), such as ultraviolet (UV) emission from intermediate- and high-mass stars. After correcting for dust extinction, an observed flux can be converted into a SFR using a suitable calibration, which is typically a linear scaling of intrinsic luminosity derived from population synthesis modeling. The modeling process requires a set of stellar evolution models and a stellar initial mass function (IMF), as well as a characterization of the star formation history (SFH; the evolution of SFR over time) and the metallicity of the population. These quantities are often not well-constrained for a given system and need to be assumed (see reviews by Kennicutt 1998, Kennicutt & Evans 2012, and references therein).

A set of flux calibrations widely used in extragalactic studies were presented by Kennicutt (1998, see Kennicutt & Evans, 2012 for updates). These calibrations are based on models of a generic population with solar metallicity, a fully populated IMF,

and a SFR that has been constant over the lifetime of the tracer emission (~ 100 Myr for UV). The flux calibrations are therefore applicable to any population that can be assumed to approximate the generic population, such as spiral galaxies. In environments with low total SF (i.e., low mass) or on subgalactic scales, however, the assumptions of a fully populated IMF and a constant SFR start to become tenuous. As a result, applying the flux calibrations in these situations can lead to inaccurate SFR estimates.

For populations located within a few Mpc, it is possible to measure SFRs more directly by fitting the color magnitude diagram (CMD) of the resolved stars to obtain a SFH (Dolphin, 2002). At its core, CMD fitting is a population synthesis technique just like flux calibration (albeit much more complex) and thus requires a set of stellar evolution models, an IMF, and an accounting of dust. The primary advantage of CMD fitting over the flux calibration method for obtaining SFRs, however, is the elimination of assumptions about the SFH and metallicity. CMD-based SFHs thus provide a relative standard for testing the accuracy of SFR estimates from commonly used flux calibrations, especially in applications where the underlying full-IMF and constant-SFR assumptions are not strictly satisfied. More generally, the SFHs can be used to test results from any other flux-based method, such as ages and masses derived under the simple stellar population (SSP) assumption.

With recent Hubble Space Telescope (HST) observations from the Panchromatic Hubble Andromeda Treasury (PHAT; Dalcanton et al., 2012), we have measured the recent SFHs (< 500 Myr) of 33 UV-bright regions in M31 and compared them with SFRs derived from UV flux. We also compared the SFHs with ages and masses derived from UV flux by treating the regions as SSPs. The UV-bright regions were cataloged by Kang et al. (2009, K09 hereafter) using Galaxy Evolution Explorer (GALEX) far-UV (FUV, $\lambda \sim 1540$ Å) flux and have areas ranging from 10^4 to 10^6 pc 2 . This range of sizes allowed us to test the reliability of the full-IMF, constant-SFR, and SSP assumptions on sub-kpc scales.

This paper is organized as follows. We describe our sample of UV-bright regions and show their CMDs from the PHAT photometry in §2.2. We summarize the CMD-fitting process, describe our extinction model, and present the resulting SFHs of the regions in §2.3. §2.4 describes the modeling of UV magnitudes from the SFHs, and §2.5 describes the total masses and the mean SFRs from the SFHs, as well as the SFRs based on

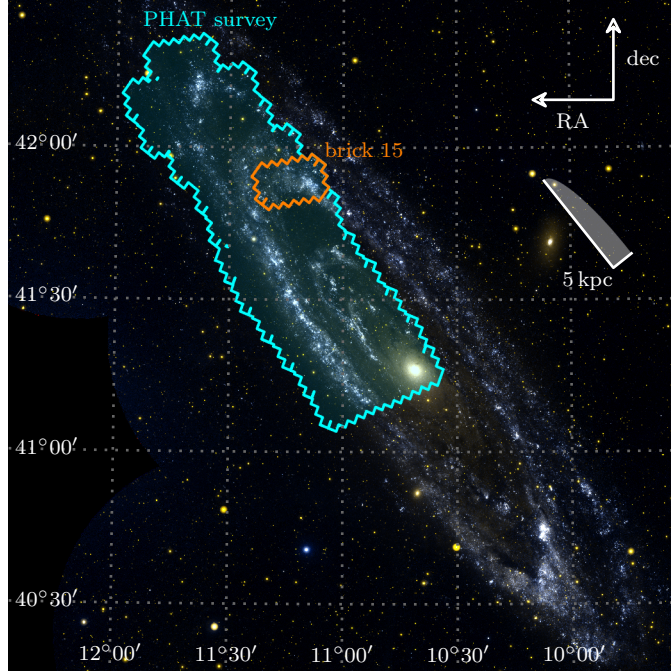


Figure 2.1 Two-color composite mosaic of M31 from the GALEX Deep Imaging Survey (FUV in blue, NUV in orange in the color version). The HST/ACS outlines of the PHAT survey area and Brick 15 are highlighted in black and gray (blue and orange in the color version), respectively. Brick 15 covers a portion of the 10-kpc star-forming ring. The scale bar indicates a distance of 5 kpc along both the major and minor axes of M31 assuming an inclination of 78 deg (Tully, 1994).

UV flux. In §2.6, we compare the UV flux-based SFRs, ages, and masses with the results from the SFHs, discuss the applicability of the full-IMF, constant-SFR, and SSP assumptions to our sample, and attempt to quantify the uncertainties associated with using UV flux to estimate SFRs, ages, and masses for sub-kpc UV-bright regions.

2.2 Observations and photometry

2.2.1 UV-Bright Regions in M31

A set of UV-bright regions in M31 were defined by K09 using FUV observations from GALEX. To summarize, K09 defined a region as any area covering at least 50 contiguous pixels (113 arcsec^2) with FUV surface brightness $\lesssim 25.9 \text{ mag arcsec}^{-2}$ (AB mag). For

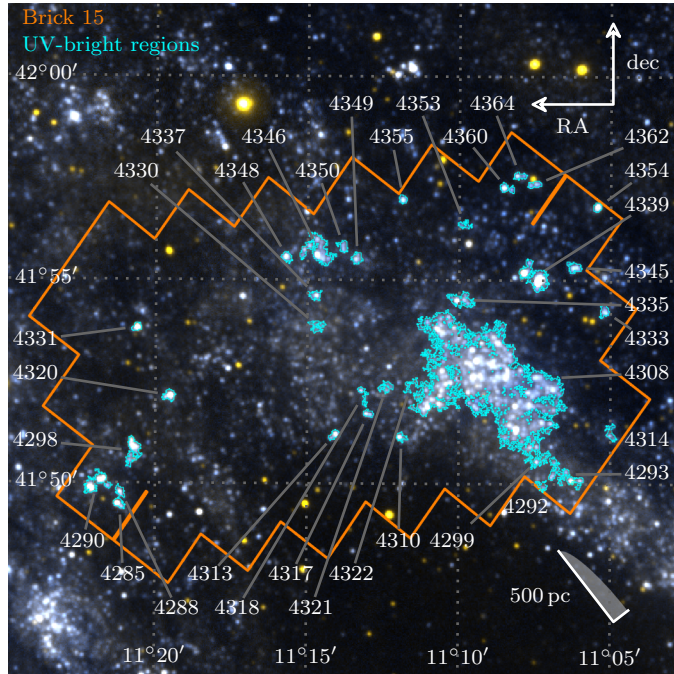


Figure 2.2 Closeup of Brick 15 from the same image in Figure 2.1. Brick 15 contains 33 of the UV-bright regions from the Kang et al. (2009) catalog (highlighted in blue in the color version), and are labeled by ID number (see Table 2.1). The region areas, deprojected assuming an inclination of 78 deg (Tully, 1994), range from $\sim 10^4$ to 10^6 pc 2 . The scale bar indicates a distance of 500 pc along both the major and minor axes of M31.

our sample, we selected the subset of these regions that were within “Brick 15” of the PHAT survey, a 0.15-deg^2 area consisting of 18 individual fields, or HST pointings, covering the 10-kpc star-forming ring (Figures 2.1 and 2.2). Of all the bricks comprising the PHAT survey area, Brick 15 contains the greatest amount of SF and the largest number regions – 33 total, with respect to the combined outline of its Advanced Camera for Surveys (ACS) images.

The identification numbers and locations of the regions in our sample as reported in K09 are given in Table 2.1. For each region, K09 measured the integrated FUV and NUV (near-UV, $\lambda \sim 2320\text{\AA}$) magnitudes and subtracted the local background estimated within a concentric annulus. We list the observed, background-subtracted FUV magnitudes, FUV_{obs} , and UV colors, $(\text{FUV} - \text{NUV})_{\text{obs}}$ in Table 2.1. Table 2.1 also lists the solid angles and deprojected physical areas of the regions, which we calculated assuming a distance to M31 of 785 kpc (McConnachie et al., 2005) and a disk inclination of 78 deg (Tully, 1994). The areas range from 7.9×10^3 to $7.3 \times 10^4\text{ pc}^2$, with one large outlier at $1.5 \times 10^6\text{ pc}^2$ (region 4308).

Table 2.1. Observational properties of UV-bright regions in PHAT Brick 15.

ID	RA ^a (deg)	dec ^a (deg)	area (10^2 arcsec 2)	area ^b (10^3 pc 2)	FUV _{obs} ^a (AB mag)	(FUV – NUV) _{obs} ^a (AB mag)
4285	11.352559	41.824921	1.6	11.2	18.570 ± 0.017	0.325 ± 0.019
4288	11.352191	41.830040	1.5	10.3	19.281 ± 0.025	0.147 ± 0.029
4290	11.364936	41.833477	5.6	38.7	17.377 ± 0.010	0.468 ± 0.011
4292	11.120670	41.833038	1.2	8.4	20.457 ± 0.052	-0.120 ± 0.064
4293	11.108700	41.837337	6.5	45.1	18.160 ± 0.016	0.388 ± 0.018
4298	11.345233	41.845989	4.9	33.7	17.859 ± 0.013	0.253 ± 0.015
4299	11.123035	41.843586	3.0	20.9	19.319 ± 0.030	0.087 ± 0.035
4308	11.152348	41.874954	216.5	1502.3	13.898 ± 0.002	0.181 ± 0.002
4310	11.197878	41.852535	1.2	8.2	19.411 ± 0.027	0.303 ± 0.030
4313	11.234838	41.853275	1.5	10.3	19.026 ± 0.022	0.290 ± 0.025
4314	11.082835	41.854801	1.8	12.2	19.714 ± 0.032	0.115 ± 0.037
4317	11.216114	41.862221	1.1	7.9	19.556 ± 0.029	0.259 ± 0.033
4318	11.218816	41.869392	1.3	8.9	19.978 ± 0.038	-0.058 ± 0.045
4320	11.325653	41.868969	2.1	14.8	18.200 ± 0.014	0.195 ± 0.016
4321	11.206724	41.872875	1.8	12.8	19.823 ± 0.037	0.118 ± 0.043
4322	11.193023	41.873569	1.2	8.2	20.810 ± 0.067	-0.164 ± 0.085
4330	11.244569	41.897583	2.1	14.7	19.848 ± 0.039	0.087 ± 0.046
4331*	11.343492	41.897060	1.3	9.1	18.411 ± 0.016	0.462 ± 0.017
4333*	11.086989	41.904243	1.8	12.5	18.811 ± 0.019	-0.271 ± 0.023
4335	11.165060	41.908730	4.6	32.0	18.172 ± 0.016	0.026 ± 0.018
4337	11.245595	41.910343	1.7	11.6	19.294 ± 0.026	0.014 ± 0.031
4339	11.125310	41.918499	9.5	66.0	16.591 ± 0.007	0.087 ± 0.008
4345*	11.103488	41.922085	2.3	15.8	18.625 ± 0.018	-0.182 ± 0.022
4346	11.244633	41.928699	10.5	73.0	17.194 ± 0.010	-0.007 ± 0.012
4348	11.261269	41.925659	1.6	11.4	18.717 ± 0.019	-0.129 ± 0.022
4349	11.222815	41.925503	1.9	12.9	19.313 ± 0.026	0.248 ± 0.030
4350	11.230723	41.930325	1.6	11.2	19.514 ± 0.030	0.062 ± 0.034
4353	11.163334	41.939396	1.2	8.5	20.168 ± 0.040	-0.241 ± 0.049
4354	11.090720	41.946636	1.3	8.9	18.454 ± 0.016	0.037 ± 0.018
4355*	11.197759	41.949593	1.1	7.9	19.008 ± 0.021	-0.289 ± 0.025
4360*	11.140469	41.954372	1.8	12.8	18.533 ± 0.017	-0.256 ± 0.020

Table 2.1 (cont'd)

ID	RA ^a (deg)	dec ^a (deg)	area (10 ² arcsec ²)	area ^b (10 ³ pc ²)	FUV _{obs} ^a (AB mag)	(FUV – NUV) _{obs} ^a (AB mag)
4362*	11.125412	41.955841	1.5	10.6	19.363 ± 0.026	-0.010 ± 0.030
4364	11.133373	41.959290	1.4	9.7	19.342 ± 0.025	0.122 ± 0.029
comb. ^c			83.6	580.3	14.764 ± 0.003	0.139 ± 0.004

^aKang et al. (2009). The magnitudes have not been corrected for extinction.

^bCalculated from the solid angles (areas in arcsec²) assuming a distance of 785 kpc (McConnachie et al., 2005) and deprojected assuming an inclination of 78 deg (Tully, 1994).

^cThe combination of all regions except for region 4308.

*SSP-like region (§2.6.3).

2.2.2 PHAT photometry

The resolved star photometry used in this study was taken from the PHAT Year 1 data release (Dalcanton et al., 2012). The PHAT photometric catalogs were generated using DOLPHOT, a version of HSTPHOT (Dolphin, 2000) with added ACS- and Wide Field Camera 3-specific modules. Although the wavelength coverage of PHAT extends from the UV to the near-infrared, we have used only the ACS optical images (F475W and F814W filters) since they contain the greatest numbers of stars and reach the deepest CMD features of the three PHAT cameras.

We applied quality cuts to the raw ACS photometric catalogs to minimize non-stellar contaminants in our CMDs. Specifically, we required that each object meet the following restrictions: $\text{SNR}_{\text{F}475\text{W}} \geq 4$, $\text{SNR}_{\text{F}814\text{W}} \geq 4$, $(\text{sharp}_{\text{F}475\text{W}}^2 + \text{sharp}_{\text{F}814\text{W}}^2) \leq 0.075$, and $(\text{crowd}_{\text{F}475\text{W}}^2 + \text{crowd}_{\text{F}814\text{W}}^2) \leq 1.0$, where **SNR**, **sharp**, and **crowd** refer to the DOLPHOT signal-to-noise, sharpness, and crowding parameters in each filter. These quality cuts are the “gst” cuts described in the main PHAT data release (Dalcanton et al., 2012).

We extracted all stars within the boundaries of the 33 UV-bright regions, combining photometry as needed for regions extending across multiple ACS fields. We did not take advantage of the improved signal-to-noise ratio where fields overlapped. The CMDs of the Brick 15 UV-bright regions are shown in Figure 2.3.

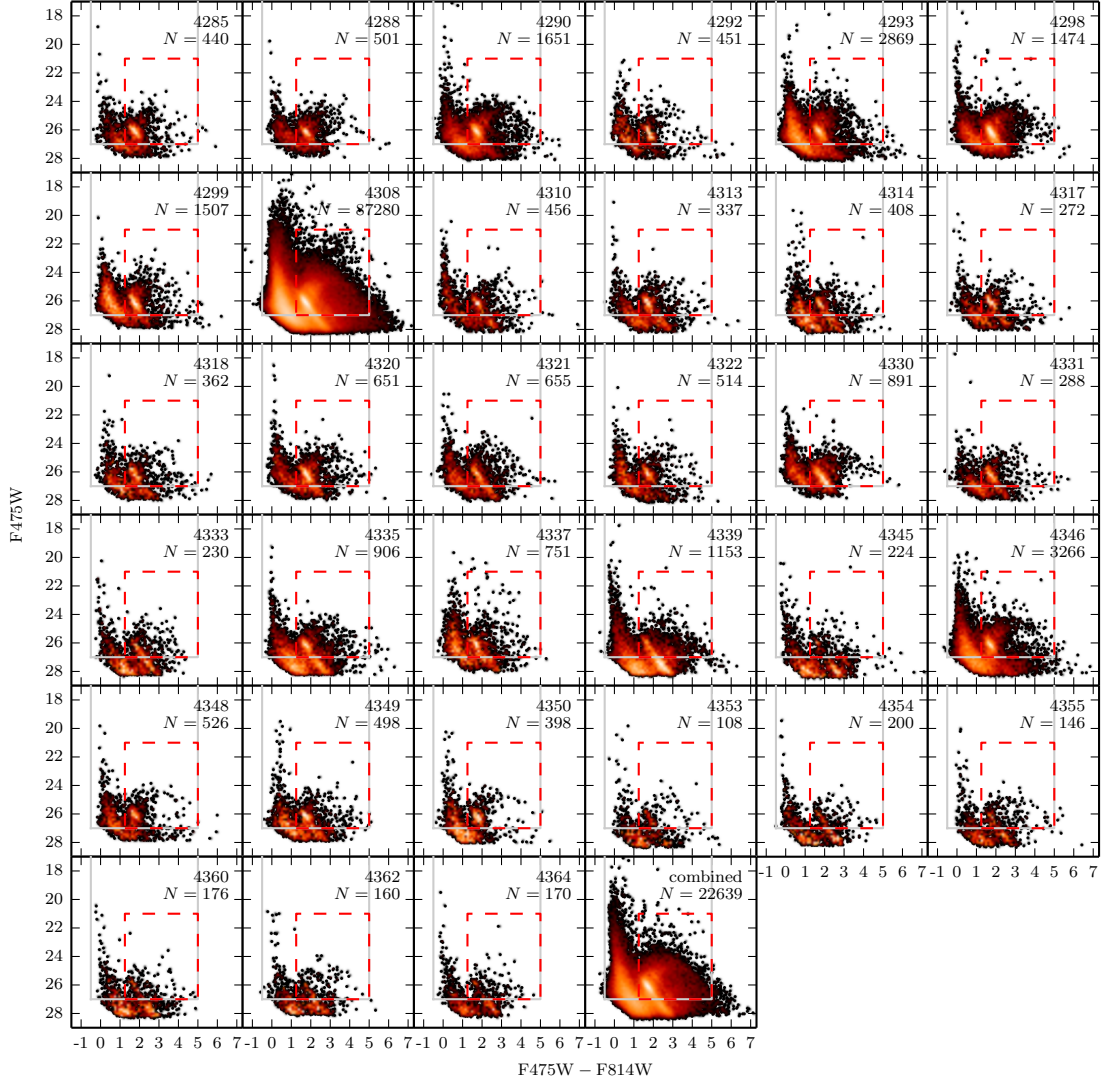


Figure 2.3 Optical color-magnitude diagrams (ACS/WFC filters F475W and F814W) of the UV-bright regions. Region ID numbers and the numbers of stars fit by MATCH are shown in each panel. The MATCH fit area is inside the solid gray line, where the faint end marks the 50% completeness limit in F475W. Stars within the dashed line (red in the color version) were excluded from the fit. The combined region includes all regions except 4308. The CMDs show broadening of the main sequence and other features, indicating that the regions are subject to nontrivial amounts of differential extinction from dust internal to M31.

2.2.3 Artificial star tests

To assess observational errors and characterize photometric completeness, we conducted $\sim 2.5 \times 10^4$ artificial star tests (ASTs) for each of the regions. The color and magnitude distributions for the ASTs were modeled after the CMDs of the individual regions. However, as discussed below in §2.3.2, we excluded the red giant branch (RGB) and red clump (RC) from the SFH analysis. We therefore only considered ASTs with properties similar to the blue portion of the CMDs, including the luminous main sequence (MS).

We used the ASTs to compute the photometric completeness functions for each of the 33 regions. The completeness functions were consistent throughout the sample, with an uncertainty of 0.06 mag in the mean 50% completeness limit in each filter. In addition, the photometric errors varied little between the regions. These consistencies allowed us to combine the ASTs from the individual regions for a total of 1.6×10^6 ASTs. This hundredfold increase in the number of ASTs available to each region provided a superior CMD error model for the SFH measurement process. The 50% completeness limits of the region sample are 27.0 mag in F475W and 26.2 mag in F814W.

2.3 The recent SFHs of UV-bright regions in M31

The derivation of the SFHs for the UV-bright regions is described in this section. The first subsection gives a brief discussion of the SFH code and describes the overall SFH measurement procedure from beginning to end. Details of the extinction model, the resulting SFHs, and our uncertainty analysis are discussed in the subsequent subsections.

2.3.1 CMD modeling with MATCH

We used the SFH code MATCH (Dolphin, 2002) to measure the SFHs of our sample of UV-bright regions. Assuming a stellar IMF, binary fraction, and a set of stellar evolution models, MATCH constructs a series of synthetic CMDs over given ranges in distance, age, metallicity, and extinction. The synthetic CMDs are convolved with the error model from the ASTs to account for observational errors. Linear combinations of the synthetic CMDs form a model which is assigned a fit value based on a comparison with the observed CMD. The SFH of the model CMD that minimizes the fit value is

considered the most likely SFH of the observed population given the input parameters. We emphasize that MATCH models the *distribution* of stars in the observed CMD, not the ages and masses of the individual stars.

The fit statistic used by MATCH is equal to $-2 \ln \Lambda_P$, where Λ_P is the Poisson likelihood ratio. According to Wilks' theorem, this statistic is asymptotically χ^2 distributed, allowing us to estimate the $n\sigma$ confidence limits in a set of SFH solutions using the condition $\text{fit} - \text{fit}_{\min} \leq n^2$, where fit_{\min} corresponds to the best-fit SFH. This method was used to estimate various uncertainties in §2.3.3 and §2.3.4.

We assumed the following for our SFH measurements:

1. A Kroupa IMF (Kroupa, 2001).
2. The Padova stellar evolution models for masses between 0.15 and $120 M_{\odot}$ (the IMF was normalized using masses down to $0.01 M_{\odot}$) including updated low-mass asymptotic giant branch tracks (Girardi et al., 2010).
3. A binary fraction of 0.35 with a uniform secondary mass distribution.
4. A distance modulus of 24.47 (McConnachie et al., 2005). The distance to M31 is fairly well-known, allowing us to fix this value and eliminate a free parameter in the CMD fitting process.
5. A set of 48 log-spaced age bins from $\log_{10}(\text{Age/ yr}) = 6.60$ to 9.00 dex with width $\Delta \log_{10}(\text{Age/ yr}) = 0.05$ dex (though as discussed in §2.3.3, we ultimately only consider the SFH out to 500 Myr, or $\log_{10}(\text{Age/ yr}) = 8.70$).
6. A metallicity range of $[\text{M}/\text{H}] = -2.3$ to 0.1 dex at a resolution of 0.1 dex with the requirement of a monotonically increasing chemical evolution model.

We also simulated the effects of intervening Galactic foreground populations using the TRILEGAL population synthesis model (Girardi et al., 2005). The solid angles of the regions were small enough, however, that no more than a few foreground stars were expected per CMD, implying a negligible impact on our final results.

Extinction was modeled using two parameters, A_{Vf} and dA_V , as described in §2.3.2. For each region, we sampled the extinction parameter surface using a combination of pattern search and grid search techniques, measuring the best-fit SFH at each point.

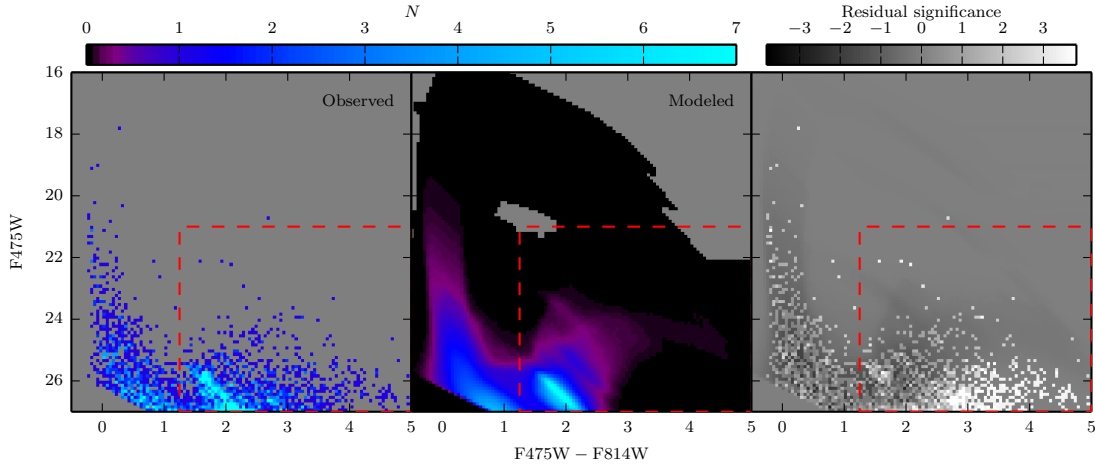


Figure 2.4 Observed CMD of region 4339, with the best-fit modeled CMD and the residual significance (the observed CMD minus the modeled CMD, weighted by the variance). The shading in the observed and modeled CMDs represents the number of stars, N , in each color and magnitude bin. The CMD limits correspond to the solid gray lines shown in Figure 2.3, and the dashed line (red in the color version) shows the area excluded from the fitting process. We find no systematic residuals in the MS, indicating that the model is a good fit to the data.

The search procedure resulted in an irregularly-sampled grid of MATCH fit values with a minimum step size of 0.05 mag in both A_{Vf} and dA_V .¹ We then compared the fit values across the grid to find the overall best-fit SFH. Figure 2.4 shows an example model CMD for the best-fit SFH of region 4339, along with the observed CMD and the residual significance.

2.3.2 Extinction model

K09 measured the average $E(B - V)$ reddening in each region using the reddening-free parameter Q and UBV photometry for individual OB stars, providing us with possible constraints on extinction for CMD fitting with MATCH. However, the CMDs in Figure 2.3 show broadening of the intrinsically narrow MS, indicating that the regions are subject to nontrivial amounts of differential extinction from dust internal to M31. In some regions the differential extinction is severe enough that the MS appears doubled.

¹ Computing fully-sampled grids for the regions at 0.05 mag resolution over reasonable ranges in A_{Vf} and dA_V was found to be computationally infeasible.

Differential extinction is also evident in the population of older stars, which we assume to be reasonably well-mixed throughout the galaxy, characterized by a broad RGB and an elongation of the RC along the reddening vector. These complexities lead to poor results when fitting an entire CMD with a single extinction value, such as that obtained from the average $E(B - V)$ in a region.

To fit the CMDs more accurately, we adopted a two-parameter extinction model consisting of a foreground dust component and a differential component. The total V-band extinction common to all stars in the CMD is set by the foreground parameter, A_{Vf} . Differential extinction is added to the stars in varying amounts following a uniform distribution from zero up to a maximum determined by the differential parameter, dA_V . Compared to the simplest case of optimizing a single extinction parameter, this extinction model provided much better fits for the observed CMDs while allowing MATCH to compute best-fit SFH solutions in a reasonable amount of time.

A specific shortcoming of the model, however, is that not all populations are expected to have the same extinction profile. Young stars tend to reside closer to the midplane of the galaxy and are likely to be physically associated with cold dense gas that hosts the dusty ISM. The older RGB and RC stars, which dominate the CMDs of the regions, can have a much larger scale height in comparison. To prevent the older populations from influencing the parameters of the extinction model we excluded all stars with both $F475W - F814W > 1.25$ and $F475W > 21.0$ mag (dashed lines in Figures 2.3 and 2.4) from the CMD fitting process. The SFHs and extinction parameters we derive from MATCH therefore correspond only to the distributions of massive MS stars (the primary producers of UV flux) as well as any blue and red He-burning stars in the CMDs.

By creating an exclusion area in the CMD, we necessarily place a limit on the total extinction that can be determined by MATCH. From the CMDs in Figure 2.3, the maximum amount of reddening a MS star can have before entering the exclusion area is $F475W - F814W \approx 1.7$ mag. Assuming the extinction curve from Cardelli et al. (1989, see §2.6.1), this amount of reddening corresponds to a total extinction of $A_{Vf} + dA_V \approx 2.8$ mag. CMD models with total extinction at this limit are indistinguishable from higher-extinction models because stars in the exclusion area do not affect the MATCH fit statistic. We therefore place an upper limit of 2.8 mag on the total extinction,

$A_{Vf} + dA_V$, during the optimization of the SFHs described in §2.3.1.

One caveat for our two-component model is that observational studies of the ISM routinely demonstrate log-normal, not uniform, density distributions (e.g., Berkhuijsen & Fletcher, 2008; Hill et al., 2008; Ballesteros-Paredes et al., 2011; Shetty et al., 2011; Dalcanton et al., 2014). Modeling the extinctions in M31 with log-normal distributions has been successful for producing extinction maps that agree with the emission from dust and gas (Dalcanton et al., 2014). Implementing such a model in MATCH would require a minimum of three parameters: a foreground component, and the mean and variance for the log-normal. A more realistic extinction model might account for the fraction of stars affected by the log-normal as well as the scale height of the stars relative to the gas in the disk, which can vary with age. With each additional parameter, however, the size of the search space increases exponentially and measuring the SFH of a single region quickly becomes impractical. It is difficult to assess how the derived SFHs are affected by our comparatively simple extinction model without repeating the measurements with a more sophisticated model. Even so, the quality of the residuals for the modeled CMDs (e.g., Figure 2.4) suggests that the two-component model is reasonably accurate.

2.3.3 Results

We present the SFHs of the UV-bright regions in Figure 2.5. The corresponding best-fit A_{Vf} and dA_V parameters are listed in Table 2.2. The uncertainties of the parameters for each region correspond to the minimum and maximum values among the set of SFHs within 1σ of the best-fit SFH on the A_{Vf}, dA_V surface (i.e., all SFHs for which $\text{fit} - \text{fit}_{\min} \leq 1$; see §2.3.1). The final metallicities of the best-fit SFHs for all regions ranged from $-1.30 \text{ dex} \leq [\text{M}/\text{H}] \leq 0.01 \text{ dex}$, with 80% of the values within 0.3 dex of the mean, $[\text{M}/\text{H}] = -0.3 \text{ dex}$.

The exclusion area in the CMDs and the 50% photometric completeness limit both restrict the age of the oldest population that can be fit by MATCH. Through synthetic CMD modeling, we found that a significant fraction of the stars in populations older than $\sim 500 \text{ Myr}$ are either within the exclusion area or below the 50% photometric completeness limit. In comparison, younger populations are well-represented in the MS/He-burning area of the CMD. We therefore adopted 500 Myr as the maximum reliable age of the SFHs.

Considering that the UV emission from an SSP becomes negligible after ~ 100 Myr (Gogarten et al., 2009; Leroy et al., 2012), we chose to display only the past 200 Myr of the SFHs. This was done to show as much of the overall history as possible while preserving sufficient detail in the 0 – 100 Myr range. Also, the SFHs are shown at a coarser time resolution than the actual resolution of $\Delta \log_{10}(\text{Age}/\text{yr}) = 0.05$ dex to simplify visual comparisons between the regions. *We use the full-resolution SFHs for all analyses that follow.*

The Padova stellar evolution models used to fit the CMDs do not include ages less than 4 Myr, creating a gap between the present time and the youngest age bin in the SFHs. To account for this, we extended the youngest bin to cover the ages in the gap and rescaled its SFR such that the total mass formed in the bin was conserved.

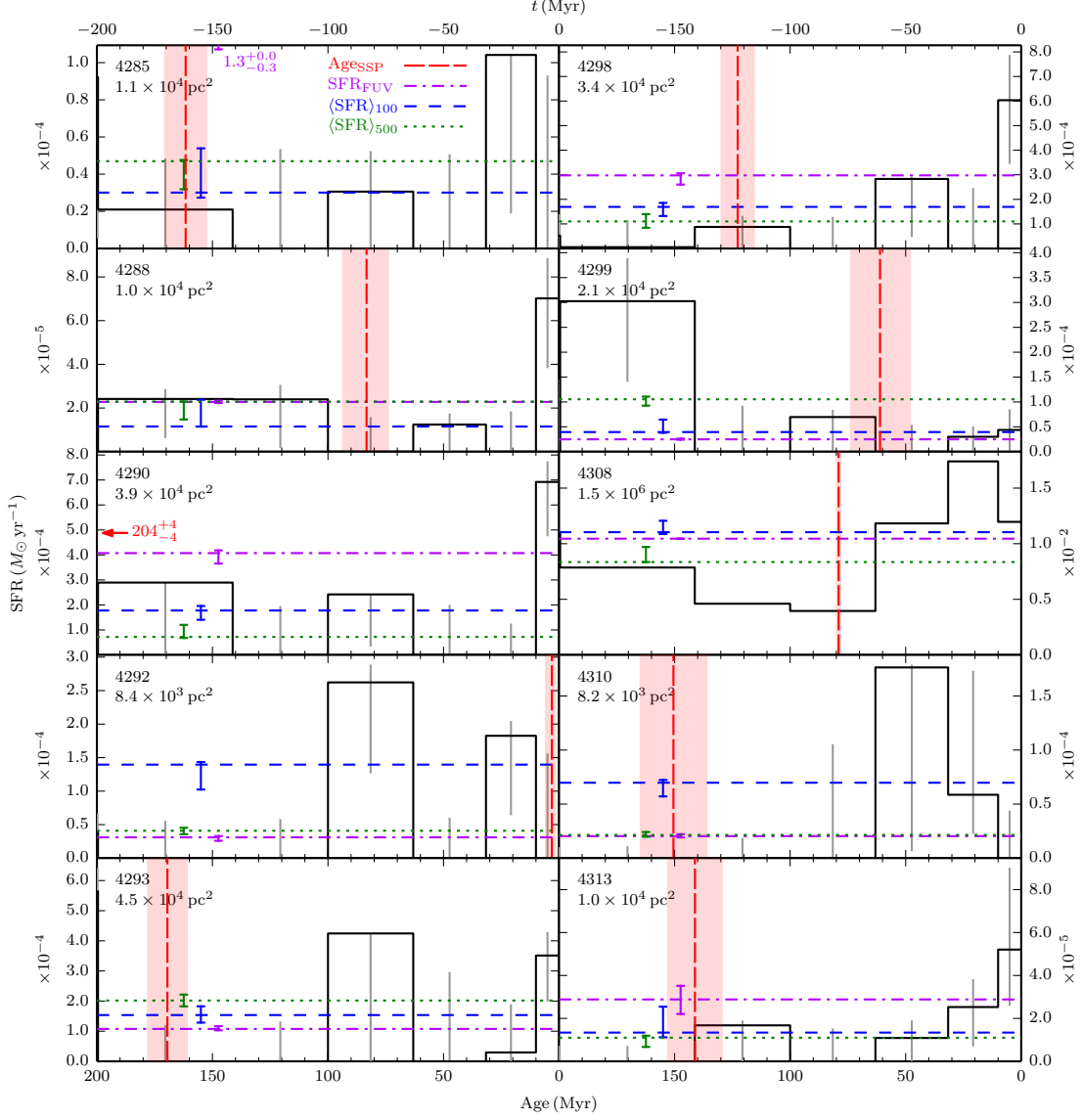
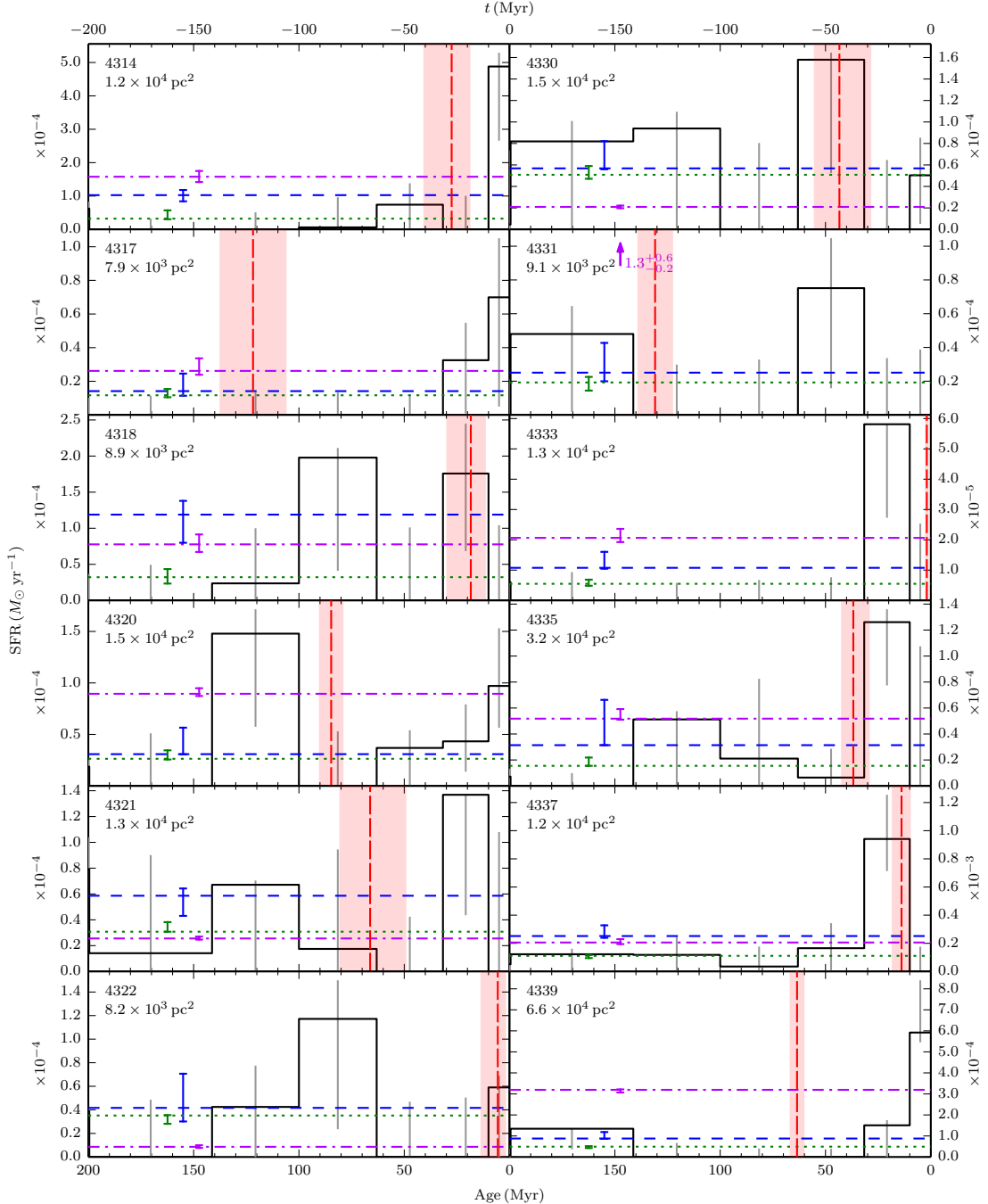


Figure 2.5 SFHs of UV-bright regions in M31 (SFR versus Age or time t , where the present is Age = $t = 0$; black histogram). The SFH for the combined region in Figure 2.3 was derived independently. The region ID number and deprojected area are given in each panel. The vertical long-dashed line (red in the color version) shows Age_{SSP}, the SSP age from Kang et al. (2009), which does not accurately describe the majority of the SFHs. The dashed-dotted line (purple in the color version) shows the constant SFR, SFR_{FUV}, obtained from the extinction-corrected observed FUV fluxes. The short-dashed and dotted lines (blue and green in the color version) show $\langle \text{SFR} \rangle_{100}$ and $\langle \text{SFR} \rangle_{500}$, the mean SFRs over the last 100 and 500 Myr, respectively.

Figure 2.5 *Cont.*

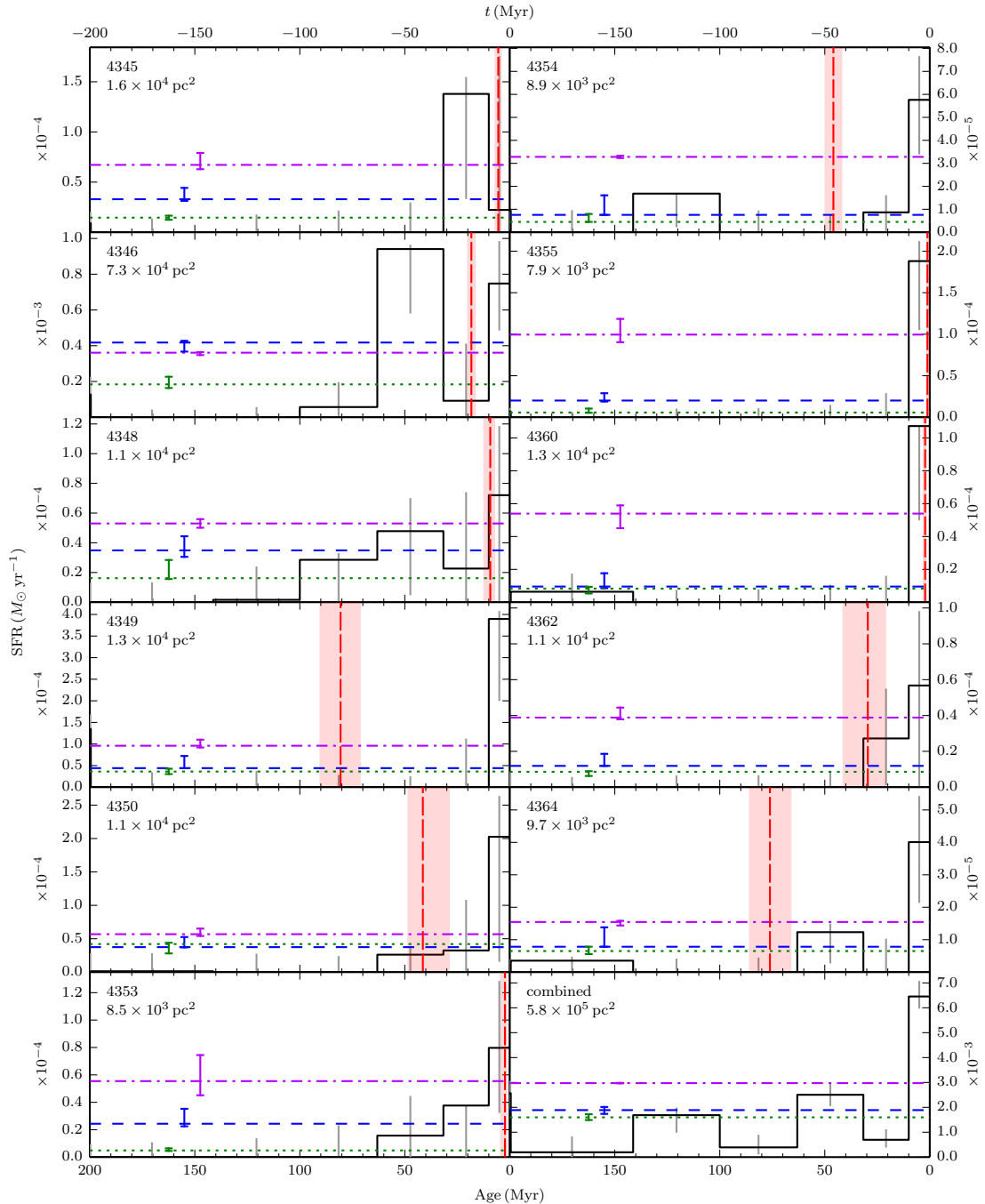
Figure 2.5 *Cont.*

Table 2.2. Region properties derived from the SFHs.

ID	A_{Vf}^a	dA_V^a	$M_{100}, \langle SFR \rangle_{100}^b$ ($10^3 M_\odot, 10^{-5} M_\odot \text{ Myr}^{-1}$)	M_{peak}^c ($10^3 M_\odot$)	M_{peak}/M_{100}	$\text{Age}_{\text{peak}}^d$ (Myr)
4285	$0.30^{+0.00}_{-0.05}$	$2.50^{+0.05}_{-0.25}$	$3.0^{+2.4}_{-0.3}$	$2.4^{+0.0}_{-1.8}$	0.78	$23.8^{+52.3}_{-8.8}$
4288	$0.60^{+0.00}_{-0.00}$	$0.00^{+0.00}_{-0.00}$	$1.2^{+1.2}_{-0.0}$	$0.6^{+0.0}_{-0.3}$	0.54	$6.7^{+54.0}_{-4.3}$
4290	$0.40^{+0.00}_{-0.05}$	$1.95^{+0.30}_{-0.05}$	$17.8^{+1.8}_{-3.7}$	$6.3^{+1.6}_{-3.7}$	0.35	$6.0^{+112.2}_{-0.7}$
4292	$0.70^{+0.00}_{-0.05}$	$1.10^{+0.05}_{-0.05}$	$14.0^{+0.4}_{-3.7}$	$10.4^{+0.3}_{-5.7}$	0.74	$75.1^{+21.5}_{-7.7}$
4293	$0.40^{+0.00}_{-0.00}$	$1.00^{+0.10}_{-0.05}$	$15.4^{+2.9}_{-2.5}$	$8.4^{+0.6}_{-5.7}$	0.55	$66.9^{+27.6}_{-11.5}$
4298	$0.45^{+0.00}_{-0.00}$	$1.95^{+0.05}_{-0.25}$	$16.9^{+1.6}_{-3.7}$	$9.4^{+0.4}_{-6.9}$	0.56	$47.4^{+5.7}_{-45.2}$
4299	$0.35^{+0.00}_{-0.00}$	$0.70^{+0.05}_{-0.00}$	$3.9^{+2.5}_{-0.1}$	$2.2^{+1.1}_{-1.4}$	0.55	$94.6^{+0.0}_{-42.1}$
4308	$0.50^{+0.00}_{-0.00}$	$1.55^{+0.00}_{-0.00}$	$1103.5^{+102.7}_{-16.6}$	$208.7^{+49.9}_{-37.3}$	0.19	$29.9^{+43.5}_{-1.5}$
4310	$0.40^{+0.05}_{-0.00}$	$0.45^{+0.00}_{-0.10}$	$7.0^{+0.2}_{-1.3}$	$4.3^{+0.0}_{-3.1}$	0.61	$59.7^{+7.4}_{-38.9}$
4313	$0.60^{+0.05}_{-0.10}$	$0.00^{+0.15}_{-0.00}$	$1.3^{+1.2}_{-0.2}$	$0.5^{+0.3}_{-0.3}$	0.38	$6.7^{+56.9}_{-2.0}$
4314	$0.95^{+0.05}_{-0.05}$	$1.50^{+0.10}_{-0.05}$	$10.3^{+1.5}_{-1.8}$	$4.0^{+0.4}_{-2.4}$	0.39	$2.2^{+80.5}_{-0.0}$
4317	$0.45^{+0.15}_{-0.10}$	$0.70^{+0.25}_{-0.15}$	$1.4^{+1.0}_{-0.3}$	$0.6^{+0.5}_{-0.3}$	0.44	$26.7^{+15.3}_{-32.4}$
4318	$0.70^{+0.15}_{-0.05}$	$1.85^{+0.30}_{-0.70}$	$11.9^{+1.9}_{-3.9}$	$7.1^{+0.9}_{-5.7}$	0.60	$75.1^{+9.2}_{-76.0}$
4320	$0.60^{+0.00}_{-0.05}$	$0.30^{+0.15}_{-0.00}$	$3.1^{+2.6}_{-0.0}$	$1.2^{+0.1}_{-0.7}$	0.39	$33.6^{+69.3}_{-26.9}$
4321	$0.50^{+0.00}_{-0.00}$	$0.80^{+0.05}_{-0.00}$	$5.9^{+0.6}_{-1.6}$	$3.2^{+0.0}_{-2.5}$	0.55	$94.6^{+0.0}_{-67.0}$
4322	$0.45^{+0.05}_{-0.00}$	$0.75^{+0.05}_{-0.15}$	$4.2^{+2.9}_{-1.2}$	$1.7^{+3.3}_{-1.1}$	0.40	$75.1^{+27.5}_{-15.2}$
4330	$0.45^{+0.00}_{-0.00}$	$0.75^{+0.05}_{-0.05}$	$5.7^{+2.5}_{-0.1}$	$3.9^{+0.7}_{-2.7}$	0.68	$53.2^{+41.4}_{-7.3}$
4331*	$0.35^{+0.15}_{-0.05}$	$1.90^{+0.15}_{-0.15}$	$2.5^{+1.8}_{-0.5}$	$2.5^{+1.1}_{-2.0}$	1.00	$47.4^{+7.2}_{-42.9}$
4333*	$0.40^{+0.05}_{-0.05}$	$0.00^{+0.10}_{-0.00}$	$1.1^{+0.5}_{-0.0}$	$1.0^{+0.1}_{-0.8}$	0.90	$16.8^{+12.2}_{-8.5}$
4335	$0.50^{+0.05}_{-0.00}$	$0.05^{+0.05}_{-0.00}$	$3.1^{+3.5}_{-0.0}$	$1.2^{+1.7}_{-0.6}$	0.38	$23.8^{+87.5}_{-18.9}$
4337	$0.80^{+0.05}_{-0.00}$	$2.00^{+0.00}_{-0.10}$	$25.2^{+7.6}_{-1.2}$	$10.8^{+0.0}_{-5.7}$	0.43	$29.9^{+12.3}_{-14.1}$
4339	$0.25^{+0.00}_{-0.00}$	$1.05^{+0.00}_{-0.05}$	$8.8^{+3.1}_{-0.2}$	$3.5^{+1.0}_{-1.7}$	0.39	$8.4^{+6.6}_{-6.2}$
4345*	$0.25^{+0.05}_{-0.00}$	$1.50^{+0.10}_{-0.10}$	$3.3^{+1.1}_{-0.2}$	$3.2^{+0.0}_{-3.0}$	0.96	$16.8^{+17.0}_{-15.4}$
4346	$0.45^{+0.00}_{-0.00}$	$1.25^{+0.00}_{-0.05}$	$41.8^{+0.9}_{-5.1}$	$12.6^{+0.0}_{-6.2}$	0.30	$42.2^{+18.5}_{-14.8}$
4348	$0.50^{+0.00}_{-0.00}$	$0.50^{+0.05}_{-0.05}$	$3.5^{+0.9}_{-0.4}$	$2.2^{+0.0}_{-1.6}$	0.64	$59.7^{+1.0}_{-51.3}$
4349	$0.70^{+0.05}_{-0.00}$	$1.20^{+0.05}_{-0.10}$	$4.4^{+2.8}_{-0.0}$	$2.4^{+0.9}_{-1.4}$	0.55	$4.7^{+22.3}_{-3.5}$
4350	$0.60^{+0.05}_{-0.00}$	$1.10^{+0.05}_{-0.05}$	$3.7^{+1.5}_{-0.0}$	$1.6^{+1.4}_{-0.9}$	0.42	$11.9^{+22.2}_{-10.3}$
4353	$0.75^{+0.15}_{-0.05}$	$1.35^{+0.15}_{-0.35}$	$2.4^{+1.1}_{-0.2}$	$1.0^{+0.5}_{-0.7}$	0.42	$37.6^{+1.5}_{-49.6}$
4354	$0.45^{+0.00}_{-0.00}$	$0.00^{+0.00}_{-0.00}$	$0.8^{+0.8}_{-0.0}$	$0.4^{+0.0}_{-0.2}$	0.52	$6.0^{+24.0}_{-0.9}$
4355*	$0.65^{+0.05}_{-0.05}$	$1.05^{+0.15}_{-0.05}$	$2.0^{+0.9}_{-0.1}$	$2.0^{+0.1}_{-1.8}$	1.00	$9.5^{+2.0}_{-6.6}$
4360*	$0.35^{+0.05}_{-0.05}$	$0.75^{+0.05}_{-0.15}$	$1.0^{+0.8}_{-0.1}$	$1.0^{+0.0}_{-0.8}$	1.00	$5.3^{+6.4}_{-4.4}$

Table 2.2 (cont'd)

ID	A_{Vf}^a	dA_V^a	$M_{100}, \langle \text{SFR} \rangle_{100}^b$ ($10^3 M_\odot$, $10^{-5} M_\odot \text{ Myr}^{-1}$)	M_{peak}^c ($10^3 M_\odot$)	M_{peak}/M_{100}	$\text{Age}_{\text{peak}}^d$ (Myr)
4362*	$0.55^{+0.05}_{-0.00}$	$0.65^{+0.05}_{-0.05}$	$1.2^{+0.7}_{-0.0}$	$1.2^{+0.0}_{-1.0}$	1.00	$15.0^{+2.6}_{-12.1}$
4364	$0.45^{+0.00}_{-0.00}$	$0.05^{+0.00}_{-0.05}$	$0.8^{+0.6}_{-0.0}$	$0.4^{+0.0}_{-0.2}$	0.53	$7.5^{+55.9}_{-2.2}$
comb. ^e	$0.35^{+0.00}_{-0.00}$	$1.45^{+0.00}_{-0.00}$	$188.9^{+12.6}_{-15.1}$	$61.6^{+0.0}_{-29.5}$	0.33	$42.2^{+32.8}_{-6.2}$

^aBest-fit foreground and differential extinction parameters. Uncertainties are zero if the best-fit value equals the minimum or maximum estimate, or if there are no other solutions within 1σ of the best-fit SFH.

^bTotal mass formed over the past 100 Myr of the SFHs. The corresponding mean SFR is $\langle \text{SFR} \rangle_{100} = M_{100} \times 10^{-8} \text{ yr}^{-1}$.

^cThe mass of the age bin with the highest SFR over the last 100 Myr of the SFH at full time resolution.

^dThe mean age of the bin corresponding to M_{peak} .

^eThe combination of all regions except for region 4308.

*SSP-like region (§2.6.3).

2.3.4 Uncertainties

The random uncertainties of the SFHs were evaluated using the Hybrid Monte Carlo (HMC) method described in Dolphin (2013). With this method, the SFH probability density function (PDF) is estimated from a sequence (or chain) of samples in SFH space, which is parameterized by age, metallicity, and SFR. Each sample in the chain is proposed and then either accepted or rejected using Hamiltonian dynamics to efficiently obtain a set of samples that are distributed according to the underlying PDF. For each region, we ran the HMC algorithm for a total of 10^4 accepted proposals and calculated the 1σ random uncertainties from the narrowest interval containing 68% of the area under the PDF.

The process of minimizing the SFHs with respect to the extinction model resulted in irregular grids of fit values on the A_{Vf}, dA_V surface (§2.3.1). For each region, we selected all SFHs in the grid within 1σ of the best-fit SFH using the condition $\text{fit} - \text{fit}_{\min} \leq 1$. The distribution for this set of SFHs was then used to estimate the 1σ systematic uncertainties in the best-fit SFH related to the measurement of A_{Vf} and dA_V .

The error bars in Figure 2.5 correspond to the combination of the random and systematic uncertainties. We did not assess the systematic uncertainties related to the

stellar evolution models used with MATCH.

We use the HMC tests and the “ 1σ ” set of SFHs to estimate the random and systematic uncertainties for all quantities derived from the SFHs (FUV magnitudes, total masses, etc.). For example, the mass of recently-formed stars in a region (see §2.5) was calculated for all of the HMC SFHs, and the random uncertainty was calculated from the distribution of the resulting masses. The systematic uncertainty was estimated from the minimum and maximum masses derived from the set of 1σ SFHs for the region. We then added the random and systematic components in quadrature to get the total uncertainty for the mass of the best-fit SFH.

2.4 UV flux modeling

We used the SFHs in Figure 2.5 as a basis for modeling the total present-day UV fluxes for each region. This technique was pioneered by Gogarten et al. (2009) in their study of UV-bright regions in the outer disk of M81, and has recently been extended to several dozen dwarf galaxies in the Local Volume (Johnson et al., 2013).

Following the procedure described in Johnson et al. (2013), the intrinsic (unreddened) FUV and NUV fluxes were modeled from the SFHs using the Flexible Stellar Population Synthesis (FSPS) code (Conroy et al., 2009; Conroy & Gunn, 2010). FSPS was run using the Padova isochrones (Girardi et al., 2010) and a Kroupa IMF (Kroupa, 2001). The metallicity for all regions was set to a constant $[M/H] = -0.3$ dex, based on the approximate final metallicities of the SFH solutions (§2.3.3). The effect of assuming a homogeneous metallicity value is discussed in §2.6.1.

The modeled FUV and NUV fluxes were converted into AB magnitudes using the formulae in Morrissey et al. (2007), and the uncertainties were calculated as described in §2.3.4. The intrinsic FUV magnitudes, $FUV_{SFH,0}$, and UV colors, $(FUV - NUV)_{SFH,0}$, of the regions are listed in Table 2.3.

We also modeled the reddened FUV and NUV fluxes using the extinction model described in §2.3.2, the best-fit A_{Vf} and dA_V values in Table 2.2, and the Cardelli et al. (1989, see §2.6.1) extinction curve. These fluxes were converted into AB magnitudes and the uncertainties were evaluated in the same manner as the intrinsic fluxes. We list the reddened FUV magnitudes, FUV_{SFH} , and the reddened UV colors, $(FUV - NUV)_{SFH}$,

in Table 2.3, and plot the difference between FUV_{SFH} and FUV_{obs} versus deprojected region area in Figure 2.6. The comparison between the modeled and observed FUV magnitudes is discussed in §2.6.1.

Table 2.3. FUV and NUV magnitudes modeled from the SFHs.

ID	FUV _{SFH,0} ^a (AB mag)	(FUV – NUV) _{SFH,0} ^a (AB mag)	FUV _{SFH} ^b (AB mag)	(FUV – NUV) _{SFH} ^b (AB mag)	A_{FUV}^c
4285	17.51 ^{+0.02} _{-0.23}	0.03 ^{+0.01} _{-0.00}	20.45 ^{+0.05} _{-0.04}	0.07 ^{+0.01} _{-0.16}	2.94 ^{+0.00} _{-0.24}
4288	17.18 ^{+0.44} _{-0.11}	-0.14 ^{+0.04} _{-0.00}	18.92 ^{+0.45} _{-0.11}	-0.13 ^{+0.05} _{-0.00}	1.73 ^{+0.00} _{-0.00}
4290	14.63 ^{+0.06} _{-0.40}	-0.15 ^{+0.04} _{-0.01}	17.59 ^{+0.07} _{-0.37}	-0.11 ^{+0.04} _{-0.02}	2.96 ^{+0.03} _{-0.12}
4292	16.59 ^{+0.95} _{-0.32}	-0.00 ^{+0.02} _{-0.11}	19.83 ^{+0.94} _{-0.13}	0.07 ^{+0.01} _{-0.12}	3.24 ^{+0.04} _{-0.19}
4293	15.43 ^{+0.55} _{-0.05}	-0.05 ^{+0.00} _{-0.06}	17.73 ^{+0.50} _{-0.00}	-0.02 ^{+0.00} _{-0.06}	2.30 ^{+0.09} _{-0.04}
4298	15.11 ^{+0.51} _{-0.02}	-0.09 ^{+0.00} _{-0.07}	18.21 ^{+0.56} _{-0.00}	-0.05 ^{+0.00} _{-0.07}	3.10 ^{+0.03} _{-0.14}
4299	17.11 ^{+0.90} _{-0.00}	0.11 ^{+0.00} _{-0.16}	18.98 ^{+0.89} _{-0.00}	0.13 ^{+0.00} _{-0.16}	1.87 ^{+0.05} _{-0.00}
4308	10.81 ^{+0.08} _{-0.03}	-0.08 ^{+0.01} _{-0.01}	13.81 ^{+0.07} _{-0.04}	-0.03 ^{+0.02} _{-0.00}	3.00 ^{+0.00} _{-0.00}
4310	17.21 ^{+0.92} _{-0.12}	-0.01 ^{+0.01} _{-0.10}	18.95 ^{+0.90} _{-0.06}	0.00 ^{+0.01} _{-0.10}	1.74 ^{+0.09} _{-0.06}
4313	17.29 ^{+0.77} _{-1.15}	-0.14 ^{+0.09} _{-0.01}	19.02 ^{+0.62} _{-0.86}	-0.13 ^{+0.09} _{-0.01}	1.73 ^{+0.21} _{-0.29}
4314	14.59 ^{+0.04} _{-0.76}	-0.26 ^{+0.12} _{-0.00}	18.86 ^{+0.04} _{-0.76}	-0.17 ^{+0.13} _{-0.01}	4.27 ^{+0.11} _{-0.11}
4317	16.89 ^{+0.28} _{-0.77}	-0.20 ^{+0.14} _{-0.00}	19.05 ^{+0.25} _{-0.89}	-0.18 ^{+0.15} _{-0.00}	2.16 ^{+0.27} _{-0.09}
4318	16.75 ^{+0.30} _{-0.16}	-0.01 ^{+0.01} _{-0.10}	20.51 ^{+0.78} _{-0.03}	0.07 ^{+0.00} _{-0.10}	3.76 ^{+0.17} _{-0.15}
4320	16.52 ^{+0.52} _{-0.00}	-0.11 ^{+0.02} _{-0.02}	18.65 ^{+0.50} _{-0.00}	-0.09 ^{+0.02} _{-0.02}	2.14 ^{+0.06} _{-0.02}
4321	16.94 ^{+0.81} _{-0.00}	-0.03 ^{+0.00} _{-0.09}	19.34 ^{+0.81} _{-0.03}	0.00 ^{+0.00} _{-0.09}	2.40 ^{+0.05} _{-0.00}
4322	17.45 ^{+1.03} _{-0.06}	0.01 ^{+0.01} _{-0.12}	19.66 ^{+1.02} _{-0.06}	0.04 ^{+0.01} _{-0.13}	2.21 ^{+0.14} _{-0.10}
4330	16.87 ^{+0.82} _{-0.05}	-0.02 ^{+0.00} _{-0.08}	19.08 ^{+0.82} _{-0.00}	0.01 ^{+0.00} _{-0.08}	2.21 ^{+0.05} _{-0.05}
4331*	18.44 ^{+0.63} _{-0.13}	0.08 ^{+0.01} _{-0.07}	21.23 ^{+0.26} _{-0.01}	0.12 ^{+0.01} _{-0.06}	2.78 ^{+0.38} _{-0.14}
4333*	18.18 ^{+0.81} _{-0.27}	-0.07 ^{+0.02} _{-0.07}	19.33 ^{+0.75} _{-0.20}	-0.07 ^{+0.02} _{-0.07}	1.16 ^{+0.15} _{-0.07}
4335	17.03 ^{+0.84} _{-0.00}	-0.06 ^{+0.00} _{-0.07}	18.54 ^{+0.74} _{-0.00}	-0.05 ^{+0.00} _{-0.07}	1.51 ^{+0.14} _{-0.00}
4337	15.14 ^{+0.09} _{-0.07}	-0.04 ^{+0.00} _{-0.00}	19.27 ^{+0.65} _{-0.03}	0.06 ^{+0.01} _{-0.08}	4.13 ^{+0.12} _{-0.06}
4339	14.79 ^{+0.15} _{-0.32}	-0.15 ^{+0.02} _{-0.02}	16.70 ^{+0.15} _{-0.30}	-0.14 ^{+0.02} _{-0.02}	1.91 ^{+0.00} _{-0.04}
4345*	16.95 ^{+0.84} _{-0.10}	-0.08 ^{+0.00} _{-0.07}	19.20 ^{+0.78} _{-0.03}	-0.06 ^{+0.00} _{-0.07}	2.25 ^{+0.18} _{-0.07}
4346	14.54 ^{+0.40} _{-0.12}	-0.09 ^{+0.02} _{-0.04}	17.18 ^{+0.40} _{-0.08}	-0.05 ^{+0.02} _{-0.04}	2.65 ^{+0.00} _{-0.04}
4348	17.23 ^{+0.79} _{-0.05}	-0.06 ^{+0.01} _{-0.07}	19.32 ^{+0.78} _{-0.01}	-0.04 ^{+0.01} _{-0.07}	2.08 ^{+0.06} _{-0.06}
4349	15.11 ^{+0.35} _{-0.57}	-0.15 ^{+0.02} _{-0.11}	18.43 ^{+0.20} _{-0.57}	-0.09 ^{+0.03} _{-0.11}	3.33 ^{+0.15} _{-0.04}
4350	16.40 ^{+0.63} _{-0.19}	-0.10 ^{+0.02} _{-0.06}	19.35 ^{+0.57} _{-0.14}	-0.05 ^{+0.02} _{-0.06}	2.96 ^{+0.15} _{-0.04}
4353	16.41 ^{+0.49} _{-0.89}	-0.25 ^{+0.17} _{-0.01}	20.00 ^{+0.27} _{-0.87}	-0.19 ^{+0.20} _{-0.00}	3.58 ^{+0.32} _{-0.22}
4354	17.38 ^{+0.53} _{-0.10}	-0.16 ^{+0.03} _{-0.01}	18.68 ^{+0.53} _{-0.10}	-0.15 ^{+0.03} _{-0.01}	1.30 ^{+0.00} _{-0.00}
4355*	16.73 ^{+0.95} _{-0.08}	-0.13 ^{+0.00} _{-0.07}	19.79 ^{+0.81} _{-0.05}	-0.08 ^{+0.00} _{-0.06}	3.06 ^{+0.19} _{-0.10}
4360*	16.66 ^{+0.55} _{-0.99}	-0.16 ^{+0.03} _{-0.11}	18.58 ^{+0.46} _{-0.83}	-0.15 ^{+0.04} _{-0.11}	1.92 ^{+0.10} _{-0.19}

Table 2.3 (cont'd)

ID	$FUV_{SFH,0}^a$ (AB mag)	$(FUV - NUV)_{SFH,0}^a$ (AB mag)	FUV_{SFH}^b (AB mag)	$(FUV - NUV)_{SFH}^b$ (AB mag)	A_{FUV}^c
4362*	$17.87^{+1.23}_{-0.00}$	$-0.08^{+0.00}_{-0.09}$	$20.27^{+1.12}_{-0.03}$	$-0.05^{+0.00}_{-0.09}$	$2.39^{+0.14}_{-0.00}$
4364	$18.03^{+0.69}_{-0.14}$	$-0.15^{+0.03}_{-0.01}$	$19.40^{+0.69}_{-0.07}$	$-0.14^{+0.03}_{-0.01}$	$1.37^{+0.00}_{-0.07}$
comb. ^d	$12.03^{+0.10}_{-0.11}$	$-0.13^{+0.01}_{-0.02}$	$14.53^{+0.09}_{-0.11}$	$-0.10^{+0.01}_{-0.02}$	$2.50^{+0.00}_{-0.00}$

^aIntrinsic (unreddened) FUV and NUV magnitudes modeled from the SFHs.

^bReddened FUV and NUV magnitudes modeled from the SFHs and the best-fit extinction parameters in Table 2.2.

^cFUV extinction correction, from the difference between FUV_{SFH} and $FUV_{SFH,0}$. Uncertainties smaller than half the reported precision are rounded to zero.

^dThe combination of all regions except for region 4308.

*SSP-like region (§2.6.3).

2.5 SFR estimates

The usual procedure for converting FUV flux into a SFR is to correct the observed flux for extinction, calculate the luminosity, and then apply the proper calibration. To test this method, we derived FUV extinction corrections, A_{FUV} , from the differences between FUV_{SFH} and $FUV_{SFH,0}$. The uncertainties in A_{FUV} were calculated as described in §2.3.4. The resulting values, listed in Table 2.3, were used to correct FUV_{obs} .

The extinction-corrected observed FUV magnitudes were converted into SFRs, SFR_{FUV} , using the flux calibration from Kennicutt (1998) with updates by Hao et al. (2011) and Murphy et al. (2011) (see Kennicutt & Evans, 2012):

$$\left(\frac{SFR_{FUV}}{M_{\odot} \text{ yr}^{-1}} \right) = 10^{-43.35} \left(\frac{L_{FUV}}{\text{erg s}^{-1}} \right) \quad (2.1)$$

where L_{FUV} is the FUV luminosity in erg s^{-1} . This calibration was derived using the stellar population synthesis code Starburst99 (Leitherer et al., 1999) assuming that the SFR has been constant over the last 100 Myr. It also assumes a fully populated Kroupa IMF (Kroupa, 2001) and solar metallicity.

Although more sophisticated tracers exist for calculating SFRs (e.g., hybrid tracers discussed in Leroy et al., 2012), none of them can be used with GALEX FUV and NUV

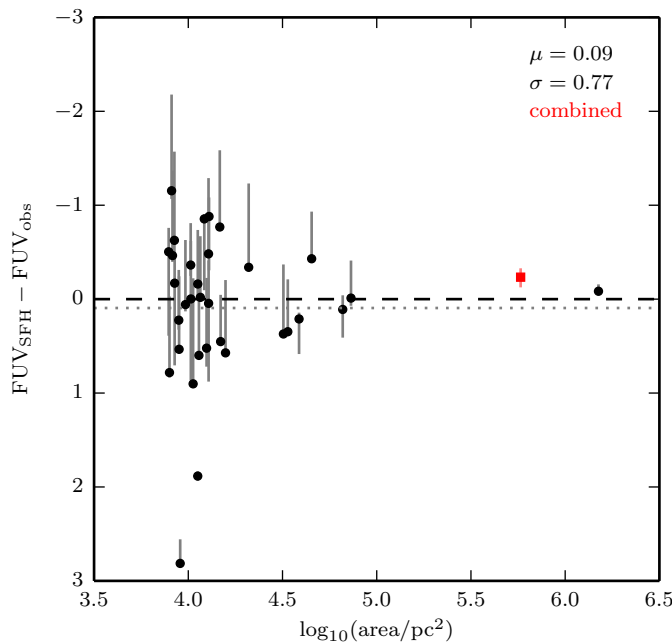


Figure 2.6 The difference between the modeled reddened (FUV_{SFH}) and observed (FUV_{obs} , Kang et al., 2009) FUV magnitudes (proportional to the log of the modeled-to-observed flux ratio) versus deprojected area. The dashed line indicates where the magnitudes are equal. On average, the FUV_{SFH} values are ~ 0.1 mag fainter than FUV_{obs} (dotted line). This difference is consistent with zero to within the 1σ scatter of ~ 0.8 mag. The scatter is greatest among the smallest regions and indicates that discrete sampling of the IMF is important on these scales. The combined region from Figure 2.3, indicated by the gray square (red in the color version), shows much better agreement between FUV_{SFH} and FUV_{obs} than the individual regions it comprises.

data alone and such calculations are therefore outside the scope of this study.

The total uncertainties in SFR_{FUV} are the quadrature sum of the photometric uncertainties propagated from FUV_{obs} and the random and systematic uncertainties derived according to §2.3.4 (where SFR_{FUV} was calculated for each value of A_{FUV} from the HMC and 1σ SFHs). The SFR_{FUV} values are listed in Table 2.4 and are shown against the SFHs in Figure 2.5.

To compare with the flux-based SFRs, we calculated the mean SFR over the last 100 Myr of the SFH, $\langle \text{SFR} \rangle_{100} = M_{100} \times 10^{-8} \text{ yr}^{-1}$, where M_{100} is the total mass formed over the same time period. The $\langle \text{SFR} \rangle_{100}$ values are shown in Figure 2.5, and both M_{100} and $\langle \text{SFR} \rangle_{100}$ are listed in Table 2.2. The uncertainties were derived as described in §2.3.4. We also calculated the mean SFR over the last 500 Myr, $\langle \text{SFR} \rangle_{500}$ (Figure 2.5). The 500 Myr timescale (the practical age limit of the SFHs, §2.3.3) is useful for understanding the overall behavior of the regions and illustrates the significance of the SF activity in the last 100 Myr with respect to the broader history. Figure 2.7 shows the log ratio of SFR_{FUV} to $\langle \text{SFR} \rangle_{100}$ versus deprojected region area, and is discussed in §2.6.2.

Table 2.4. SFRs, ages, and masses from FUV and NUV fluxes.

ID	SFR _{FUV,0} ^a ($\times 10^{-5} M_{\odot} \text{ yr}^{-1}$)	SFR _{FUV} ^b ($\times 10^{-5} M_{\odot} \text{ yr}^{-1}$)	Age _{SSP} ^c (Myr)	$M_{\text{SSP}}^{\text{c}}$ ($\times 10^3 M_{\odot}$)
4285	$2.4^{+0.0}_{-0.4}$	$13.3^{+0.2}_{-2.6}$	$161.6^{+8.9}_{-8.9}$	$160.00^{+0.00}_{-0.00}$
4288	$3.2^{+1.4}_{-0.5}$	$2.3^{+0.1}_{-0.1}$	$83.3^{+10.2}_{-9.3}$	$14.00^{+3.00}_{-2.00}$
4290	$33.5^{+1.1}_{-11.5}$	$40.7^{+1.1}_{-4.2}$	$203.9^{+4.0}_{-4.0}$	$2000.00^{+0.00}_{-0.00}$
4292	$5.5^{+7.7}_{-1.4}$	$3.1^{+0.2}_{-0.5}$	$3.1^{+2.6}_{-1.5}$	$1.30^{+1.70}$
4293	$16.0^{+9.8}_{-0.7}$	$10.8^{+0.9}_{-0.7}$	$169.5^{+8.4}_{-8.4}$	$900.00^{+0.00}_{-0.00}$
4298	$21.6^{+12.9}_{-0.4}$	$29.8^{+0.9}_{-3.7}$	$122.7^{+7.0}_{-7.0}$	$150.00^{+0.00}_{-0.00}$
4299	$3.4^{+4.4}_{-0.0}$	$2.5^{+0.1}_{-0.1}$	$61.1^{+12.6}_{-12.9}$	$12.00^{+3.00}_{-2.20}$
4308	$1129.2^{+80.5}_{-37.5}$	$1045.1^{+1.9}_{-2.1}$	$79.0^{+0.8}_{-0.7}$	$9800.00^{+0.00}_{-0.00}$
4310	$3.1^{+4.1}_{-0.3}$	$2.0^{+0.2}_{-0.1}$	$150.5^{+14.2}_{-14.3}$	$77.00^{+0.00}_{-51.00}$
4313	$2.9^{+2.6}_{-1.9}$	$2.9^{+0.6}_{-0.7}$	$141.2^{+11.7}_{-11.6}$	$48.00^{+102.00}_{-0.00}$
4314	$34.6^{+1.3}_{-17.6}$	$15.8^{+1.7}_{-1.6}$	$27.5^{+13.0}_{-8.5}$	$64.00^{+21.00}_{-26.00}$
4317	$4.2^{+1.0}_{-2.4}$	$2.6^{+0.7}_{-0.2}$	$121.8^{+15.5}_{-15.5}$	$40.00^{+0.00}_{-0.00}$
4318	$4.8^{+1.5}_{-0.6}$	$7.8^{+1.4}_{-1.1}$	$18.4^{+11.2}_{-6.7}$	$1.60^{+1.20}_{-0.91}$
4320	$5.9^{+3.2}_{-0.3}$	$8.9^{+0.5}_{-0.2}$	$84.7^{+5.4}_{-5.4}$	$180.00^{+20.00}_{-0.00}$
4321	$4.0^{+4.4}_{-0.0}$	$2.6^{+0.1}_{-0.1}$	$66.2^{+14.2}_{-16.8}$	$19.00^{+3.00}_{-7.00}$
4322	$2.5^{+3.8}_{-0.1}$	$0.9^{+0.1}_{-0.1}$	$5.6^{+7.8}_{-3.5}$	$0.24^{+0.32}_{-0.12}$
4330	$4.2^{+4.8}_{-0.2}$	$2.1^{+0.1}_{-0.1}$	$43.4^{+11.7}_{-14.7}$	$23.00^{+16.00}_{-6.00}$
4331*	$1.0^{+0.8}_{-0.1}$	$13.3^{+5.5}_{-1.7}$	$130.9^{+8.0}_{-8.1}$	$2000.00^{+0.00}_{-0.00}$
4333*	$1.3^{+1.3}_{-0.3}$	$2.1^{+0.3}_{-0.1}$	$1.9^{+0.5}_{-0.4}$	$0.40^{+0.00}_{-0.00}$
4335	$3.7^{+3.8}_{-0.0}$	$5.2^{+0.7}_{-0.1}$	$36.8^{+5.4}_{-7.4}$	$46.00^{+0.00}_{-12.00}$
4337	$20.9^{+1.9}_{-1.2}$	$20.6^{+2.4}_{-1.1}$	$13.9^{+4.2}_{-4.0}$	$16.00^{+22.00}_{-0.00}$
4339	$28.9^{+3.0}_{-8.5}$	$31.9^{+0.2}_{-1.3}$	$63.5^{+3.1}_{-3.1}$	$96.00^{+24.00}_{-0.00}$
4345*	$4.0^{+4.3}_{-0.3}$	$6.7^{+1.2}_{-0.4}$	$5.5^{+1.3}_{-1.2}$	$0.46^{+0.28}_{-0.12}$
4346	$36.5^{+16.4}_{-3.8}$	$36.1^{+0.3}_{-1.3}$	$18.3^{+1.6}_{-1.7}$	$110.00^{+0.00}_{-0.00}$
4348	$3.1^{+3.2}_{-0.1}$	$5.3^{+0.3}_{-0.3}$	$9.3^{+2.9}_{-1.9}$	$0.76^{+0.10}_{-0.25}$
4349	$21.6^{+8.1}_{-8.9}$	$9.6^{+1.4}_{-0.4}$	$80.6^{+9.6}_{-9.2}$	$190.00^{+40.00}_{-30.00}$
4350	$6.6^{+4.9}_{-1.0}$	$5.7^{+0.8}_{-0.3}$	$41.4^{+6.9}_{-12.4}$	$23.00^{+9.00}_{-6.00}$
4353	$6.5^{+3.5}_{-4.3}$	$5.5^{+1.9}_{-1.0}$	$2.3^{+1.9}_{-0.8}$	$0.21^{+0.05}_{-0.05}$
4354	$2.7^{+1.3}_{-0.5}$	$3.3^{+0.0}_{-0.0}$	$45.9^{+3.8}_{-3.8}$	$17.00^{+0.00}_{-4.00}$
4355*	$4.8^{+5.8}_{-0.4}$	$10.0^{+1.9}_{-0.9}$	$1.1^{+0.3}_{-0.3}$	$1.90^{+0.00}_{-0.00}$
4360*	$5.2^{+3.2}_{-3.7}$	$5.4^{+0.5}_{-0.9}$	$2.2^{+0.8}_{-0.4}$	$0.28^{+0.00}_{-0.00}$

Table 2.4 (cont'd)

ID	$\text{SFR}_{\text{FUV},0}^{\text{a}}$ ($\times 10^{-5} M_{\odot} \text{ yr}^{-1}$)	$\text{SFR}_{\text{FUV}}^{\text{b}}$ ($\times 10^{-5} M_{\odot} \text{ yr}^{-1}$)	$\text{Age}_{\text{SSP}}^{\text{c}}$ (Myr)	$M_{\text{SSP}}^{\text{c}}$ ($\times 10^3 M_{\odot}$)
4362*	$1.7^{+2.9}_{-0.0}$	$3.9^{+0.6}_{-0.1}$	$29.5^{+11.6}_{-8.3}$	$5.80^{+2.00}_{-2.30}$
4364	$1.5^{+1.3}_{-0.2}$	$1.5^{+0.0}_{-0.1}$	$76.1^{+9.6}_{-9.8}$	$9.80^{+2.20}_{-1.50}$
comb. ^d	$368.8^{+31.8}_{-36.4}$	$297.3^{+0.9}_{-0.9}$		

^aSFR derived using the modeled intrinsic FUV magnitudes and the flux calibration from Kennicutt & Evans (2012).

^bSFR derived using the extinction-corrected observed FUV magnitudes and the flux calibration from Kennicutt & Evans (2012). Uncertainties smaller than half the reported precision are rounded to zero.

^cSSP ages and masses from Kang et al. (2009). Missing uncertainties indicate that the minimum/maximum value either is not available (4355) or is larger/smaller than the best value (4292, 4353, 4360). The uncertainty is zero where the minimum/maximum value equals the best value.

^dThe combination of all regions except for region 4308.

*SSP-like region (§2.6.3).

2.6 Discussion

2.6.1 FUV magnitudes

The differences between the reddened FUV magnitudes modeled from the SFHs and the observed FUV magnitudes of the regions, $\text{FUV}_{\text{SFH}} - \text{FUV}_{\text{obs}}$, shown in Figure 2.6 are normally distributed with a mean and standard deviation of $\mu = 0.09 \text{ mag}$ and $\sigma = 0.8 \text{ mag}$, respectively. The FUV_{SFH} values are consistent with the FUV_{obs} values on average, demonstrating that the FUV magnitudes are largely free of several potential systematic effects, such as scattering of FUV photons from or into the regions or misinterpretation of the CMDs by MATCH.

The consistency of μ with zero supports the hypothesis from §2.3.2 that the A_{Vf} , dA_V extinction model adequately describes the dust affecting the MS stars in the regions. Because A_{FUV} is derived by extrapolating A_{Vf} and dA_V along an extinction curve, the lack of a significant offset between FUV_{SFH} and FUV_{obs} justifies our adoption of the average Galactic extinction curve from Cardelli et al. (1989) with the standard value of $R_V = 3.1$. This is consistent with results from Barmby et al. (2000) and Bianchi et al.

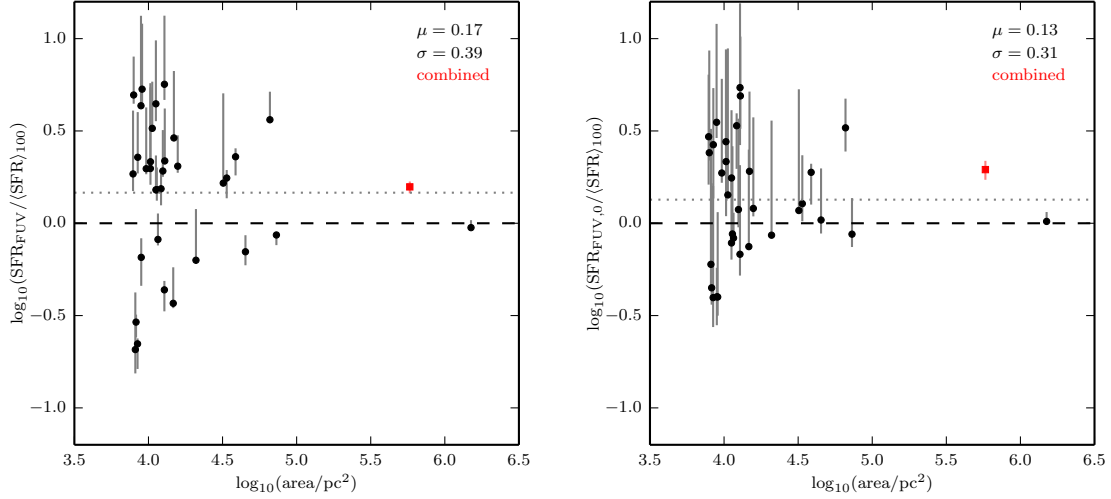


Figure 2.7 The log ratio of the FUV flux-based SFRs to $\langle \text{SFR} \rangle_{100}$, the 100 Myr mean SFR of the SFHs, versus deprojected region area. The dashed lines indicate where the SFRs are equal, and the mean and standard deviation of each log ratio is shown in its respective panel. On the left, the flux-based SFRs, SFR_{FUV} , were derived from the extinction-corrected observed FUV magnitudes. The SFR_{FUV} values are consistent with $\langle \text{SFR} \rangle_{100}$ to within the 1σ scatter, though variations from the metallicity assumed by the flux calibration can explain approximately one third of the total offset (this effect also applies to the right panel). The primary sources of the scatter are discrete sampling of the IMF and variability in the SFHs. The flux-based SFRs in the right panel, $\text{SFR}_{\text{FUV},0}$, were derived from the intrinsic FUV magnitudes modeled from the SFHs. The scatter is primarily due to SFH variability, as IMF sampling is not important for $\text{SFR}_{\text{FUV},0}$. In both panels, the combined region from Figure 2.3, indicated by the gray square (red in the color version), shows much better agreement between the flux-based and mean SFRs than the individual regions it comprises.

(1996), who found that the overall extinction curves of M31 and the Galaxy are similar for optical and UV wavelengths, respectively.

It is somewhat surprising that assuming the Cardelli et al. (1989) extinction curve does not produce a larger systematic offset between FUV_{SFH} and FUV_{obs} . Previous studies have shown that local dust properties and the shape of the extinction curve strongly depend on environment (Fitzpatrick & Massa, 2007; Bianchi et al., 2011; Efremova et al., 2011), which brings into question the applicability of any galaxy-averaged extinction curve to specific locations within a galaxy. Furthermore, results from Bianchi et al. (2011) and Efremova et al. (2011) indicate that areas of intense SF, such as UV-bright regions, tend to have extinction curves that are steeper in the UV regime. Despite these details, we find that, given a mean visual extinction of $A_{\text{V}} + dA_{\text{V}} \approx 1.5$ in the regions, the $\mu = 0.09$ mag offset is consistent with a value of R_{V} between 3.1 and 3.2. This is well within the range of R_{V} values obtained by Fitzpatrick & Massa (2007) for 328 lines of sight in the Galaxy, for which the mean and standard deviation was 3.0 and 0.3, respectively.

Although the modeled and the observed FUV magnitudes agree on average, Figure 2.6 shows that the scatter in $\text{FUV}_{\text{SFH}} - \text{FUV}_{\text{obs}}$ about the mean is larger than the uncertainties. A possible source of this scatter is the assumption of a homogeneous metallicity for the modeled FUV magnitudes, $[\text{M}/\text{H}] = -0.3$ dex, whereas the actual final metallicity values for most of the regions varied between $[\text{M}/\text{H}] = -0.6$ and 0.0 dex (§2.3.3). Figure 6 in Johnson et al. (2013) illustrates how the FUV luminosity of a constant SFR model changes as a function of input metallicity. Near $[\text{M}/\text{H}] = -0.3$ dex ($\log_{10}(Z/Z_{\odot}) \approx -0.3$, assuming the helium-to-metals enrichment law from Bressan et al., 2012), changing $[\text{M}/\text{H}]$ by ± 0.1 dex causes the modeled FUV flux to change by ∓ 0.015 dex, or ± 0.038 mag in terms of FUV magnitudes. Given a metallicity dispersion of 0.3 dex, variations from the assumed metallicity therefore lead to an uncertainty of about 0.1 mag in FUV_{SFH} . The effect of assuming a homogeneous metallicity contributes only a small amount to the total scatter.

Figure 2.6 shows that the scatter in $\text{FUV}_{\text{SFH}} - \text{FUV}_{\text{obs}}$ appears to increase with decreasing region area. Because the regions are all defined to have the same minimum FUV surface brightness, the masses of the regions roughly scale with area, implying that the scatter is greatest for the regions with the lowest masses. A well-known characteristic

of low-mass systems is that the distribution of stellar masses is noticeably discrete, particularly with respect to the high-mass end of the IMF where the relative probability of star formation is low. As a result, the sampling of stellar masses from the IMF is not as complete in such systems as for higher-mass systems. This is illustrated in the CMDs in Figure 2.3, which show the upper MS in many of the regions to be sparsely populated compared with the much larger region 4308.

To model UV fluxes from the SFHs, FSPS assumes that the stellar mass formed in each age bin represents a full sampling of the IMF, which is inconsistent with the actual sampling of stellar masses in the regions. Therefore, the modeled flux is underestimated in regions that have an apparent excess of massive MS stars relative to the number expected from a fully populated IMF, and is overestimated in regions with an apparent lack of massive MS stars. The size of this discrepancy should be larger for regions with lower masses due to the sampling of the IMF becoming more discrete.² Given that area is a proxy for mass in our sample, the scatter in Figure 2.6 is indeed consistent with this expectation. We therefore consider the scatter in the magnitudes to be caused by the application of the full-IMF assumption where the effect of discrete sampling is important.

To further test the impact of region size on the magnitude discrepancy, we constructed a larger effective region by combining the photometry of all regions, excluding region 4308 (the largest region). We then measured the SFH of the combined region and modeled the total FUV magnitude following the same procedure used for the other regions. The total area and effective observed FUV magnitude (from the combination of the observed magnitudes of the individual regions) are given in Table 2.1, and the CMD is shown in Figure 2.3. We show the SFH and the corresponding best-fit extinction parameters in Figure 2.5 and Table 2.2, respectively. The modeled FUV magnitude is listed in Table 2.3.

The combined region in Figure 2.6 has a magnitude difference similar to region 4308 and is more consistent with the sample mean than the majority of the individual regions it comprises. The combined region apparently produces a much better representation of stellar masses in the IMF than when the regions are considered individually, making the combined region more consistent with the full-IMF assumption. This result supports

² This effect is often associated with the term, “stochasticity”.

our hypothesis that the scatter in the magnitudes is largely explained as a sampling effect of the IMF.

We estimate that discrete sampling becomes important for the UV-bright regions below an area of $\sim 10^5 \text{ pc}^2$, and amounts to an uncertainty of $\sigma = 0.8 \text{ mag}$ in the modeled FUV magnitudes, or a factor of $10^{|-0.4\sigma|} = 2$ in flux. Determining a characteristic area threshold from our sample is difficult, however, due to the lack of regions with areas between 10^5 and 10^6 pc^2 .

2.6.2 SFR estimates from FUV flux

Figure 2.7 shows many of the same features as Figure 2.6, namely log-normally distributed ratios with a mean offset and scatter that is largest among the smallest regions (see §2.6.1). The log-normal distribution for the $\text{SFR}_{\text{FUV}}/\langle \text{SFR} \rangle_{100}$ values shown in Figure 2.7 has $\mu = 0.2$ and $\sigma = 0.4$.

The offset in Figure 2.7 is less than the scatter, thus the SFR_{FUV} values are, on average, consistent with the $\langle \text{SFR} \rangle_{100}$ values, although the offset is somewhat larger relative to the scatter than in Figure 2.6. The consistency of the FUV magnitudes in Figure 2.6 shows that the offset in the SFR ratios is not due to scattering of FUV photons, misinterpretation of the CMDs by MATCH, a deficiency in the extinction model, or an inaccurate extinction curve. Additionally, both SFR_{FUV} and $\langle \text{SFR} \rangle_{100}$ assume a timescale of 100 Myr, so the offset is also not due to inconsistent timescales.

One difference between SFR_{FUV} and $\langle \text{SFR} \rangle_{100}$, however, is that the FUV flux calibration was derived assuming solar metallicity. The FUV brightness of a stellar population decreases with increasing metallicity (see §2.6.1), so the SFR of a high-metallicity population would need to be higher than that of a low-metallicity population with the same FUV flux and SFH. Specifically, overestimating [M/H] by 0.1 dex causes the SFR to be overestimated by 0.015 dex.

Because nearly all of the final metallicities were subsolar, the majority of the SFR_{FUV} values are overestimated to some degree. Solar metallicity is higher than the mean final metallicity from MATCH by 0.3 dex, so the FUV-based SFRs are overestimated by about 0.05 dex on average. Variations from the metallicity assumed by the flux calibration therefore account for approximately one third of the $\mu = 0.2$ offset in Figure 2.7. With no other obvious systematic effects at work, we attribute the remaining offset

to low-number statistics.

Like FSPS, the FUV flux calibration from Kennicutt (1998) assumes that the IMF is fully populated, so discrete sampling of the IMF should produce a similar amount of scatter in Figures 2.6 and 2.7. Regions that are brighter for their mass than expected from the full-IMF assumption will have their FUV-based SFRs overestimated, and regions that are fainter than expected will have their SFRs underestimated. As in Figure 2.6, Figure 2.7 shows that this discrepancy increases with decreasing area. The scatter in the SFR ratios therefore appears consistent with the application of the full-IMF assumption to low-mass regions. By comparing the σ parameters of the log-normal distributions in Figures 2.6 and 2.7 ($| -0.4 \times 0.8 | = 0.3$ and 0.4, respectively), however, we find that the SFR ratios are somewhat more scattered than the magnitude differences. This suggests that there is an additional factor contributing to the scatter.

In addition to the full-IMF assumption, the FUV flux calibration assumes a constant SFR over at least the past ~ 100 Myr. It is clear from the SFHs in Figure 2.3 that none of the regions are consistent with this assumption. To test how the inconsistency with the constant-SFR assumption affects the SFR estimates, we used the FUV flux calibration to derive another set of SFRs from the modeled intrinsic magnitudes in Table 2.3, $SFR_{FUV,0}$. Both FSPS and the flux calibration assume a fully populated IMF, so $SFR_{FUV,0}$ is determined self-consistently. Also, despite the fact that the regions are largely inconsistent with the full-IMF assumption, $\langle SFR \rangle_{100}$ depends only on the total mass formed in the SFH, not on how the stellar masses were sampled from the IMF. Therefore, any discrepancies between $SFR_{FUV,0}$ and $\langle SFR \rangle_{100}$ beyond the measured uncertainties are not due to discrete IMF sampling.

The log ratios of $SFR_{FUV,0}$ to $\langle SFR \rangle_{100}$ are shown versus deprojected region area in Figure 2.7. As for the SFR ratios from the observed FUV magnitudes, we assumed a log-normal distribution and calculated μ and σ to be 0.1 and 0.3, respectively. As expected, we find that the FUV-based SFRs are consistent with the mean SFRs on average. The SFR ratios are widely scattered, indicating that the accuracy of the FUV-based SFR estimates is strongly affected by variations in the SFHs. In the extreme case of an SSP, Leroy et al. (2012) found that FUV-based SFR estimates are intrinsically scattered by a factor of ~ 3 to 4 ($\sigma \approx 0.5$ to 0.6 in log space) due to uncertainty about the age of the SSP within a 100 Myr timescale. The uncertainty we measure, $\sigma = 0.3$,

is within the intrinsic limit, which we expect given that the regions are more complex than SSPs (see §2.6.3).

The dependence of the flux-based SFRs on the SFHs is further illustrated by the combined region in Figure 2.7. The $\text{SFR}_{\text{FUV},0}/\langle \text{SFR} \rangle_{100}$ ratio for the combined region is similar to that of region 4308 (the largest region) and is more consistent with unity than for most of the individual regions it comprises. By combining the regions, many of the variations in the individual SFHs are averaged out and the combined SFH is more constant by comparison.

Taken together, the uncertainties due to discrete sampling of the IMF and variability in the SFHs account for the total amount of scatter in the $\text{SFR}_{\text{FUV},0}/\langle \text{SFR} \rangle_{100}$ ratios, as shown from the quadrature sum of the σ values of the log-normals, $0.3^2 + 0.3^2 \approx 0.4^2$. The uncertainty components are also the same size, demonstrating that satisfying the full-IMF assumption and satisfying the constant-SFR assumption are equally important for obtaining precise SFR estimates from the FUV flux calibration. Inconsistencies with the full-IMF and constant-SFR assumptions appear to become important in UV-bright regions smaller than $\sim 10^5 \text{ pc}^2$. Assuming that one has a robust FUV extinction correction, FUV-based SFRs estimated for regions smaller than this limit are uncertain by a factor of about 2.5. We stress that this factor represents the best case uncertainty, as the dust corrections for integrated UV flux are often unclear and substantial. Our results are consistent with warnings from Murphy et al. (2011), Kennicutt & Evans (2012), and Leroy et al. (2012) that flux calibrations become problematic on sub-kpc scales.

Perhaps the most important assumptions behind the flux calibration method are the assumed SFH and that SFR has a clear relationship with observed flux. However, it is ambiguous whether the difference in flux between two populations is due to a simple difference in SFR because the observed flux strongly depends on the underlying SFH. This dependence is observed on scales both large and small, e.g., as demonstrated for UV color in spiral galaxies by Barnes et al. (2011) and for FUV flux in our sample of UV-bright regions. We find, for example, that although region 4299 and 4350 have total masses (and thus mean SFRs) within 5%, their SFHs are quite different and the FUV flux of region 4350 is more than a factor of 2 brighter than that of 4299. We also find that FUV flux is often degenerate with SFH (a wide range of SFHs can give rise to

the same FUV flux), such as the case for regions 4318 and 4330. These complexities illustrate the inherent difficulty of using integrated flux alone to characterize SF.

2.6.3 SSP ages and masses

Because the integrated UV spectrum of an SSP evolves significantly over relatively short timescales (\sim few Myr, as indicated in SSP models from Leitherer et al., 1999), the integrated FUV – NUV color can, in principle, be used to estimate age through population synthesis modeling. Clearly, this technique rests on the assumption that the population approximates an SSP, i.e., that the population can be characterized by a single age. The SSP assumption is typically acceptable for stellar clusters where stars form at effectively the same time, but it becomes untenable whenever the SFH is more complex than a single SF event.

K09 estimated SSP ages, Age_{SSP} , for the regions by comparing the observed FUV – NUV colors with Padova stellar evolution models (Girardi et al., 2010) for a range of metallicities and dust types. The models were reddened according to the average $E(B - V)$ measured in the regions (see §2.3.2). The ages derived for solar metallicity and $R_V = 3.1$ are shown with the SFHs in Figure 2.5 and are listed in Table 2.4. It is immediately clear from the SFHs that the majority of the regions do not approximate SSPs and that the very concept of assigning single ages to these regions is invalid. Furthermore, the Age_{SSP} values often do not correspond to the main episodes of SF.

The corresponding SSP masses, M_{SSP} , were estimated by K09 from Age_{SSP} and the FUV luminosity. We list the M_{SSP} values in Table 2.4 and show the log of M_{SSP}/M_{100} versus deprojected region area in Figure 2.8. Most of the M_{SSP} values are within one or two orders of magnitude of M_{100} . This large uncertainty range is a consequence of applying the SSP assumption to regions that are generally not SSPs. By coloring each point in Figure 2.8 by Age_{SSP} , we find that the masses for regions determined to be young are underestimated, and the masses for regions determined to be older are overestimated (an old SSP must be more massive than a young SSP to have the same UV luminosity). This trend is observed independent of region size.

Although most of the regions are not SSPs, we do find that the SSP assumption is justified in some cases. To identify SSP-like regions, we calculated the ratio of the mass formed in the age bin with the highest SFR over the last 100 Myr, M_{peak} , to the

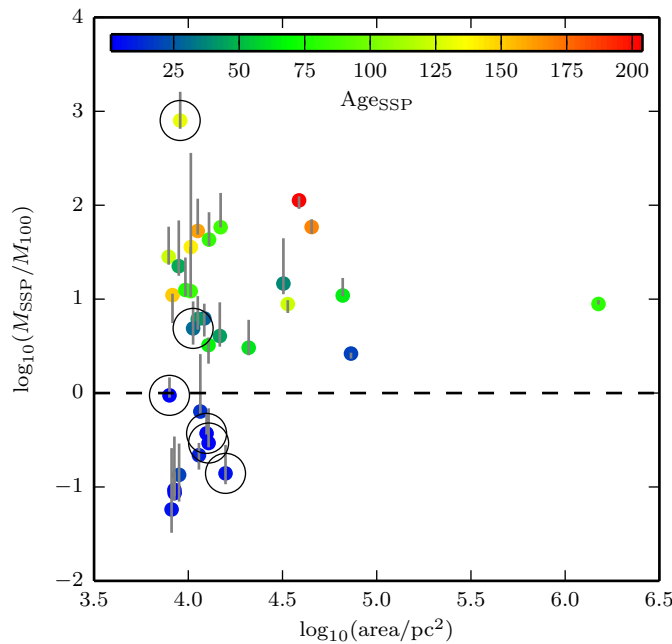


Figure 2.8 The log ratio of the SSP masses based on UV color and luminosity, M_{SSP} , to the total mass formed over the last 100 Myr of the SFHs, M_{100} , versus deprojected region area. The markers are shaded (colored in the color version) according to the SSP age, Age_{SSP} , corresponding to M_{SSP} . The dashed line indicates where the masses are equal. SSP masses are underestimated and overestimated for regions that are estimated to be young and old, respectively. The circled points indicate the most SSP-like regions identified in the sample (§2.6.3). At $\log_{10}(M_{\text{SSP}}/M_{100}) \approx 3$, region 4331 is extremely discrepant and we do not include it in our SSP analysis. The M_{SSP} values for the other SSP-like regions indicate a factor of 3 to 4 uncertainty with respect to the M_{100} values.

total mass formed over the same time period, M_{100} . The values of M_{peak} , M_{peak}/M_{100} , and Age_{peak} (the mean age of the bin containing M_{peak}) are listed in Table 2.2. We considered any region with $M_{\text{peak}}/M_{100} \geq 0.9$ to be consistent with an SSP, i.e., any region that has formed more than 90% of its total mass in a single age bin over the last 100 Myr. We found that 18% of the regions (6 of 33; 4331, 4333, 4345, 4355, 4360, and 4362) meet this criterion and we indicate them in Tables 2.1, 2.2, 2.3 and 2.4.

Except for region 4331, the mean discrepancy between Age_{SSP} and Age_{peak} for the SSP-like regions is 10 Myr. On average, M_{SSP} is consistent with M_{100} to within a factor of 3 or 4 (excluding region 4331). These age and mass discrepancies are often larger than the error bars shown in Figures 2.5 and 2.8. Region 4331 is extremely discrepant in both age ($\text{Age}_{\text{SSP}} - \text{Age}_{\text{peak}} = 80$ Myr) and mass ($M_{\text{SSP}}/M_{100} = 800$) for reasons that are unclear, and we do not include it in the remaining analyses.

The uncertainties in Age_{SSP} are about 3 Myr, on average, and are propagated solely from the photometric uncertainties. We suggest that these uncertainties are underreported, given that metallicity and extinction can potentially introduce systematics that are much larger than the uncertainties in FUV luminosity and FUV – NUV color. We consider below how metallicity and extinction affect the age and mass estimates.

Metallicity increases the rate at which an SSP becomes redder with age (Bianchi et al., 2011; Kang et al., 2009). Therefore, if metallicity is overestimated, then Age_{SSP} will be underestimated. To test how significantly metallicity affects the ages of the SSP-like regions, we compared the ages for solar metal abundance with the ages derived by K09 for $Z = 0.05$. The change in metallicity decreased the SSP age estimates by an average of 6 Myr. We also compared the corresponding masses and found that the masses for solar metal abundance were, on average, a factor of 2 larger than the those for $Z = 0.05$.

Since UV flux is highly susceptible to dust extinction, any errors in the applied reddening values can significantly affect the derived SSP ages and masses. Namely, if $E(B - V)$ is underestimated, then the corrected FUV – NUV color will be redder than it should be (assuming the extinction curve of Cardelli et al., 1989, although this is another potential source of uncertainty), causing an overestimate in Age_{SSP} . The change in M_{SSP} is less clear because underestimating the FUV luminosity and overestimating the age have opposite effects.

To quantify the impact of changes in FUV – NUV color on Age_{SSP} and M_{SSP} , we used FSPS (see §2.4) to model the time evolution of the UV magnitudes of an SSP with solar metallicity. For a 10 Myr old SSP ($\text{FUV} - \text{NUV} \approx -0.09$), we found that a 0.1 mag reduction in $E(B - V)$ causes the age to be overestimated by 25 Myr and the mass to be overestimated by a factor of 2.6. Age_{SSP} and M_{SSP} are therefore highly sensitive to changes in FUV – NUV.

Systematics from the assumed metallicity and the extinction correction can plausibly account for the observed age and mass discrepancies among the SSP-like regions. From these discrepancies, we propose that more realistic uncertainties for the ages and the masses derived from UV flux are 10 Myr and a factor of 3 to 4, respectively, though the limited number of regions resembling SSPs makes more precise uncertainties difficult to determine. The most striking aspect of this analysis is that over 80% of the regions in the sample are entirely inconsistent with the SSP assumption in the first place, a fact that could not be known without measuring the SFHs, calling into question the practice of deriving ages and masses for populations that are not confirmed SSPs.

2.7 Conclusion

In this study, we have derived the recent (< 500 Myr) SFHs of 33 UV-bright regions in M31 using optical HST observations from PHAT. The regions were defined by K09 based on GALEX FUV surface brightness and have areas ranging from 8×10^3 to 1.5×10^6 pc 2 . We used the SFH code MATCH to fit the CMDs of the regions and measure their the SFHs based on the resolved stars from the PHAT photometry. We modeled the extinction in the regions using a foreground parameter and a differential parameter, which were optimized for each region to find the best-fit SFH.

We used FSPS to model both the intrinsic and reddened FUV and NUV magnitudes of the regions based on their SFHs. The differences between the modeled reddened and the observed FUV magnitudes, $\text{FUV}_{\text{SFH}} - \text{FUV}_{\text{obs}}$, followed a normal distribution with $\mu = 0.09$ and $\sigma = 0.3$. On average, the FUV_{SFH} values were consistent with the FUV_{obs} values, confirming the reliability of the SFHs, our extinction model, and the Cardelli et al. (1989) extinction curve. We attribute the scatter in the flux ratios to the assumption made by FSPS that the IMF is fully populated while the actual distribution

of stellar masses becomes more discrete as smaller regions are considered.

The observed, extinction-corrected FUV magnitudes were converted into SFRs, SFR_{FUV} , using the FUV flux calibration from Kennicutt (1998) with updates by Hao et al. (2011) and Murphy et al. (2011). We also derived the mean SFRs for the last 100 Myr of the SFHs, $\langle \text{SFR} \rangle_{100}$. The $\text{SFR}_{\text{FUV}}/\langle \text{SFR} \rangle_{100}$ ratios were log-normally distributed with $\mu = 0.2$ and $\sigma = 0.4$. Overall, the SFR_{FUV} values were consistent with the $\langle \text{SFR} \rangle_{100}$ values, though a small amount of the offset was attributable to inconsistencies with the metallicity assumed by the flux calibration.

The intrinsic modeled FUV magnitudes were also converted into SFRs, $\text{SFR}_{\text{FUV},0}$, which were free from biases due to extinction corrections and IMF sampling. The log-normal for the $\text{SFR}_{\text{FUV},0}/\langle \text{SFR} \rangle_{100}$ ratios had $\mu = 0.1$ and $\sigma = 0.3$, indicating that assuming a constant SFR (implicit in the flux calibration) for regions with highly variable SFHs is an important source of scatter. We conclude that the total scatter in the $\text{SFR}_{\text{FUV}}/\langle \text{SFR} \rangle_{100}$ ratio is due to the assumptions of a full IMF and a constant SFR in regions where discrete sampling of the IMF and high variability in the SFHs are important. Combined, these effects result in a factor of 2.5 uncertainty in the FUV-based SFRs. Although there is a significant lack of regions in our sample with areas between 10^5 and 10^6 pc^2 , we estimate that discrete IMF sampling and SFH variability become important below 10^5 pc^2 , or scales of a few hundred pc.

Ages and masses were derived for the regions by K09 from observed FUV–NUV color and FUV luminosity, using the assumption that the regions are SSPs. By comparing the ages to the SFHs, we found that most of the regions are entirely inconsistent with the SSP assumption. Furthermore, the ages often did not correspond to the main episodes of SF, and the masses were discrepant with the masses integrated from the SFHs by up to 2 orders of magnitude. These results call into question the practice of deriving ages and masses for populations that are not confirmed SSPs.

We identified SSP-like regions as regions which formed 90% or more of their mass over the past 100 Myr in a single age bin of their SFH. These regions accounted for 18% of our sample (6 of 33). Among this subset, we found discrepancies of 10 Myr in the ages and a factor of 3 – 4 in the masses derived from UV flux, most likely due to systematics in metallicity and extinction. We propose that these discrepancies represent realistic uncertainties in the SSP ages and masses, though the limited number of SSP-like regions

in our sample makes the uncertainties difficult to determine. Finally, identification of the SSP-like regions was not possible from integrated FUV flux.

We thank Y. Kang for his assistance in understanding the results presented in Kang et al. (2009). This research has made use of NASA’s Astrophysics Data System Bibliographic Services and the NASA/IPAC Extragalactic Database (NED), which is operated by the Jet Propulsion Laboratory, California Institute of Technology, under contract with the National Aeronautics and Space Administration. This work was supported by the Space Telescope Science Institute through GO-12055. Support for D. R. W is provided by NASA through Hubble Fellowship grant HST-HF-51331.01 awarded by the Space Telescope Science Institute, which is operated by the Association of Universities for Research in Astronomy, Inc., under NASA contract NAS 5-26555. This research made use of Astropy, a community-developed core Python package for Astronomy (Astropy Collaboration et al., 2013), as well as NumPy and SciPy (Oliphant, 2007), IPython (Pérez & Granger, 2007), and Matplotlib (Hunter, 2007).

Chapter 3

Synthetic ultraviolet flux maps of M31 from resolved optical photometry.

Abstract

Starting from star formation histories based on color magnitude diagrams, we have used stellar population synthesis to create maps of synthetic far- and near-ultraviolet (FUV and NUV) flux at sub-kpc resolution for the northeast quadrant of M31. The synthetic maps reproduced all of the main morphological features found in corresponding maps of observed FUV and NUV flux, including rings and large star-forming complexes. Comparing the flux maps pixel-by-pixel, we found the median synthetic-to-observed flux ratios to be $1.02 +0.74/-0.43$ in FUV and $0.79 +0.35/-0.24$ in NUV. The synthetic fluxes were therefore consistent overall with the observed fluxes in both filters. We used the observed fluxes and standard flux calibrations to derive star formation rate (SFR) maps, which we compared with a map of the mean SFRs over the last 100 Myr of the star formation histories (SFHs). We determined a lower limit of $\text{SFR} \sim 10^{-5} M_{\odot} \text{ yr}^{-1}$ below which the commonly assumed linear relationship between UV flux and SFR appears to break down. Above this limit, we found the median ratios of the flux-based SFRs to

the mean SFRs to be $0.57 +0.47/-0.26$ in FUV and $1.24 +0.88/-0.52$ in NUV. Both the FUV and NUV flux-based SFRs were therefore consistent overall with the mean SFRs derived from the SFHs. Integrating over the entire mean SFR map, we found a global SFR of $0.3 M_{\odot} \text{ yr}^{-1}$. The corresponding measurements from the flux-based SFR maps were factors of 0.74 (FUV) and 1.45 (NUV) of the global mean SFR value. It is not yet understood why the SFR ratios in the global case are larger than the median pixel-wise ratios. The primary source of uncertainty in both the synthetic flux maps and the flux-based SFR maps was most likely incomplete IMF sampling due to the small pixel areas. With the exception of the faintest areas of the galaxy, we did not identify any trends for flux or SFR with environment.

3.1 Introduction

M31 is a well-studied, $\sim L_*$ galaxy and has been observed at a variety of wavelengths, e.g., in the ultraviolet (UV) by the Galaxy Evolution Explorer (GALEX; Morrissey et al., 2007), in the optical, including H α , for the Local Group Galaxies Survey (Massey et al., 2006), and in the infrared by the Spitzer Space Telescope (Gordon et al., 2006). The wealth of high-quality data available for M31 provides a valuable opportunity to model various observations and test our current understanding of stellar astrophysics. In particular, the initial mass function (IMF), stellar evolution and spectra models, and extinction curves are all required to model the light produced by a galaxy.

A critical ingredient for modeling the flux from a galaxy is a detailed knowledge of its underlying star formation history (SFH). Deriving SFHs by color-magnitude diagram (CMD) analysis is a reliable method that can be used whenever photometry of resolved stars is available. An extensive optical photometric catalog for M31 has been compiled by the Panchromatic Hubble Andromeda Treasury (PHAT Dalcanton et al., 2012), and Lewis et al. (2014) have used these data to derive the spatially-resolved SFH of the northeast quadrant. With sub-kpc resolution, this SFH dataset is the ideal input for stellar population synthesis codes that model total flux given a population's star formation rate (SFR) and metallicity evolution. The result is a set of spatially-resolved maps of synthetic broadband flux in M31 which can be compared with observations.

The Lewis et al. (2014) SFHs can also be used to create temporally-averaged SFR maps. Because the SFHs were derived from the resolved stars without any prior assumptions about the SFHs, such maps provide a standard against which flux-based SFR estimates (e.g., using any of the calibrations from Kennicutt & Evans, 2012) can be tested. Using integrated flux to estimate SFRs for distant galaxies, where resolved stars are not available, is a common technique in extragalactic astronomy. Previous studies have investigated how flux-based SFR estimators hold up against resolved-star SFHs in sub-kpc UV-bright regions (Simones et al., 2014) and in low-metallicity dwarf galaxies (McQuinn et al., 2014). The SFHs of Lewis et al. (2014) based on data from PHAT make it possible to broaden this type of analysis to include a wide variety of environments in the most prominent local group spiral galaxy.

In this study, we have used the PHAT CMD-based SFHs and stellar population synthesis to create maps of synthetic ultraviolet (UV) flux at sub-kpc resolution for the northeast quadrant of M31. We then compared the synthetic flux maps with observations from GALEX. We have only focused on GALEX FUV and NUV (far and near UV), though this work can easily be extended to other wavelength regimes. In §3.2, we describe the SFH dataset and the production of the synthetic flux maps. §3.3 describes the process of producing observed flux maps from GALEX FUV and NUV images. The creation of SFR maps both from the SFHs and the observed fluxes using common flux-SFR calibrations are described in §3.4. In §3.5, we compare the synthetic maps with the observations and compare mean SFR maps with SFRs estimated from observed flux. We conclude in §3.6.

3.2 Synthetic UV flux maps

3.2.1 The spatially-resolved star formation history of M31

The PHAT survey (Dalcanton et al., 2012) measured multiband photometry for over 100 million resolved stars in M31 using the Hubble Space Telescope (HST). The PHAT survey area is shown in Figure 4.1. Lewis et al. (2014) used photometry in the two optical bands (F475W and F814W, observed with the Advanced Camera for Surveys, ACS, instrument) to derive spatially-resolved SFHs for the northeast quadrant of M31, excluding the crowded bulge area. To summarize their work, each brick (using PHAT

terminology; see Figure 4.1) in the PHAT survey (except bricks 1 and 3) was divided into 450 regions on a uniform 15×30 grid, with each region $\sim 24 \text{ arcsec} \times 27 \text{ arcsec}$ in size. The F475W,F814W CMD of each region was then fit using the SFH history code MATCH (Dolphin, 2002) to determine the most likely SFH under the following assumptions:

1. The Kroupa (2001) IMF.
2. The Padova isochrones (Marigo et al., 2008) with updated asymptotic giant branch tracks (Girardi et al., 2010).
3. A binary fraction of 0.35 with a uniform secondary mass distribution.
4. A distance modulus of 24.47 (McConnachie et al., 2005).
5. An age resolution of 0.1 dex over the range $6.60 \leq \log_{10}(\text{age}) \leq 9.90$.
6. A metallicity resolution of 0.1 dex over the range $-2.3 \leq [\text{M}/\text{H}] \leq 0.1$, constrained to increase over time.
7. A two-parameter extinction model with foreground (A_{Vf}) and differential (dA_V) components, where the A_{Vf} and dA_V parameters were optimized for each cell (see also Simones et al., 2014).

In addition, the modeled CMDs were optimized for the main sequence by excluding all stars with $\text{F475W} - \text{F814W} > 1.25$ and $\text{F475W} > 21$ from the fit.

3.2.2 Broadband UV flux modeling

We used the SFH dataset from Lewis et al. (2014) to model broadband fluxes in various filters, allowing us to create synthetic flux maps for the PHAT survey area. Past studies have used CMD-based SFHs to model fluxes, including Gogarten et al. (2009) for UV-bright regions in the outer disk of M81, Johnson et al. (2013) for dwarf galaxies in the Local Volume, and more recently Simones et al. (2014) for a small sample of UV-bright regions in M31. Our work builds directly on the analysis of Simones et al. (2014) by extending our coverage to the entire PHAT survey area to include a wide variety of environments. We chose to focus on modeling fluxes in the GALEX FUV and NUV

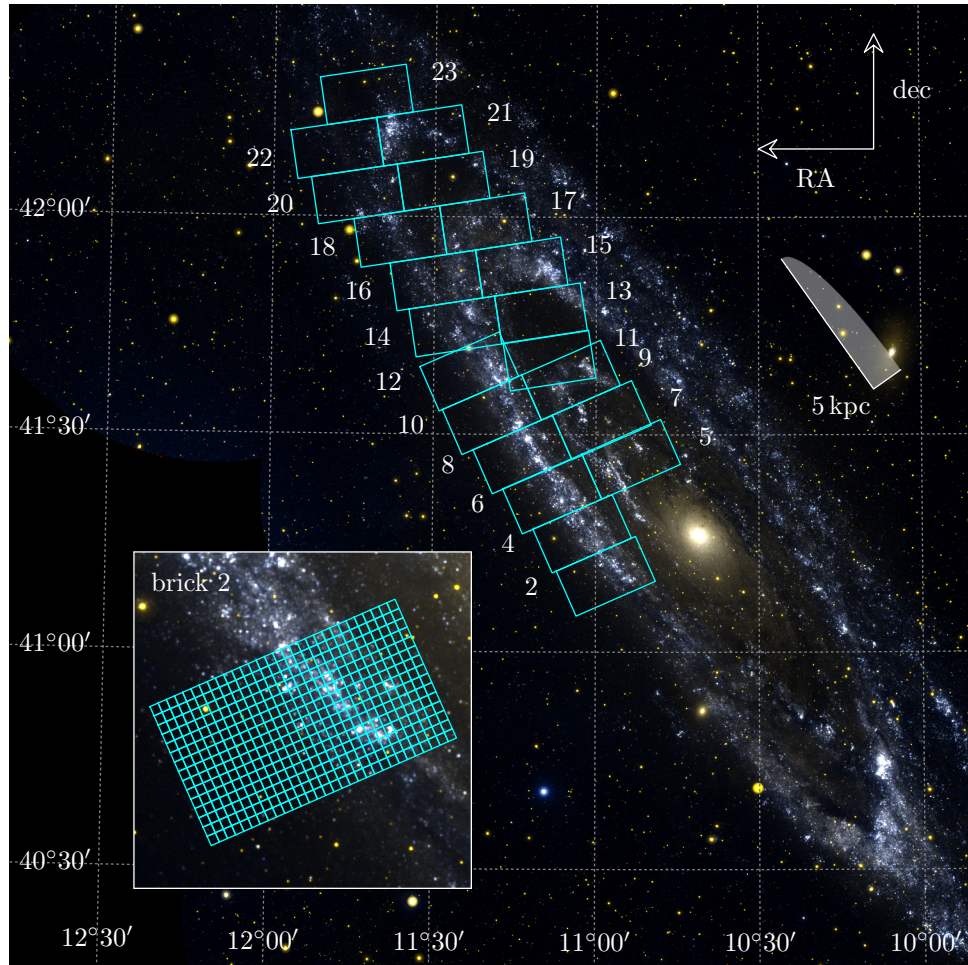


Figure 3.1 Map of the PHAT survey area. The 21 PHAT bricks analyzed in this study are outlined and numbered. Each brick was divided into 450 regions on a 15×30 grid, as shown for brick 2 in the inset panel. Lewis et al. (2014) derived the SFHs for all of the $\sim 24 \text{ arcsec} \times 27 \text{ arcsec}$ regions.

filters only (see Table 3.1). However, because we begin by modeling spectral energy distributions (SEDs), the process we describe below can easily be generalized to derive fluxes in any set of filters.

The modeling of broadband flux for a given region in the 15×30 grid of a given PHAT brick is based on the technique described in Johnson et al. (2013). We began with a set of simple stellar population (SSP) models generated using the Flexible Stellar Population Synthesis (FSPS) code (Conroy et al., 2009; Conroy & Gunn, 2010). For consistency with Lewis et al. (2014), we ran FSPS assuming the Kroupa (2001) IMF and the Padova isochrones (Marigo et al., 2008) with updated asymptotic giant branch tracks (Girardi et al., 2010). We also chose the were BaSeL 3.1 semi-empirical stellar SED library (Westera et al., 2002). The SSPs were aged from $\log(\text{age}) = 5.500$ to 10.175 in steps of 0.025 dex. We set the SSP metallicities independently for each region depending on its SFH as either the mean metallicity over the last 100 Myr of the SFH, or the most recent metallicity where $\text{SFR} > 0$ if all SFRs over the last 100 Myr were zero (we chose the 100 Myr timescale because it corresponds to the lifetime of UV emission).

We applied the SSP models to a region’s SFH to model its integrated SED. We first processed the SFH into a suitable form by rescaling the first age bin to include all ages up to the present (the Padova isochrones are only available for $\log_{10}(\text{age}) \geq 6.60$), and increasing the age resolution of the full SFH to 20 samples per age bin. The subsampled SFH was then interpolated to the series of ages in the set of SSP models. The SED of each SSP was weighted by its corresponding mass from the SFH, and the individual SSP SEDs were finally summed to derive the integrated intrinsic (i.e., unattenuated) model SED for the region.

We derived an attenuated SED for the region using the same two-component extinction model used by MATCH to fit the CMD together with the region’s best-fit A_{Vf} and dA_V parameters (Lewis et al., 2014). To do this, we divided the intrinsic SED into 30 identical component SEDs (larger numbers of components did not significantly improve the accuracy of our results). Each component was attenuated according to the Cardelli et al. (1989) extinction curve with a uniform random A_V drawn between A_{Vf} and $A_{Vf} + dA_V$. The Cardelli et al. (1989) extinction curve predicts the amount of extinction relative to that in the V band, A_V , as a function of wavelength and is based on the average extinction in the Galaxy with a total-to-selective extinction ratio

Table 3.1. Filter constants and image names.

Filter	$(\text{erg s}^{-1} \text{ cm}^{-2} \text{ \AA}^{-1}) / (\text{counts s}^{-1})$	AB mag zeropoint	Images
GALEX FUV	2.40×10^{-15} a	18.82 ^a	PS_M31_MOS00-fd-int.fits PS_M31_MOS07-fd-int.fits PS_M31_MOS08-fd-int.fits PS_M31_MOS09-fd-int.fits PS_M31_MOS10-fd-int.fits
GALEX NUV	2.06×10^{-16} a	20.08 ^a	PS_M31_MOS00-nd-int.fits PS_M31_MOS07-nd-int.fits PS_M31_MOS08-nd-int.fits PS_M31_MOS09-nd-int.fits PS_M31_MOS10-nd-int.fits

^ahttp://galexgi.gsfc.nasa.gov/docs/galex/FAQ/counts_background.html

of $R_V = 3.1$. Previous studies have shown that this extinction curve is overall applicable to M31 in both the UV (Bianchi et al., 1996) and the optical (Barmby et al., 2000) regimes. Finally, the attenuated SED components were summed back together to obtain the region’s integrated attenuated model SED.

The intrinsic and attenuated model SEDs were convolved with the response curves for the GALEX FUV and NUV filters to obtain absolute synthetic FUV and NUV magnitudes. These were converted into apparent magnitudes for the region by projecting to a distance modulus of 24.47 (McConnachie et al., 2005), consistent with Lewis et al. (2014). We used the apparent magnitudes and the appropriate magnitude-to-flux conversion formulae (see Table 3.1) to derive the intrinsic and attenuated broadband UV fluxes for the region. Hereafter, we will use a subscript (indicated here by X) to refer to either FUV or NUV and denote their intrinsic and attenuated fluxes by $f_{X,\text{SFH},0}$ and $f_{X,\text{SFH}}$, respectively.

After modeling the intrinsic and attenuated fluxes for all of the regions in a brick, we assembled the flux values (for a given filter) into a 15×30 array to form an image mapping the synthetic flux across the brick. The brick map was independently tied to a world coordinate system using a 2D least-squares optimization to find the best-fit CD matrix (Calabretta & Greisen, 2002) for a gnomonic tangent plane projection using the known RA and dec coordinates of the brick grid vertices measured by Lewis et al.

(2014). We repeated this process for all of the Lewis et al. (2014) bricks, resulting in a set of 21 brick maps. We then reprojected and added the brick maps using Montage¹ to create full maps, or mosaics, of synthetic FUV and NUV flux for the PHAT survey area.

All of the mosaic maps are registered to a grid defined by a template header that was automatically chosen by Montage as the best fit to the collection of input brick maps. The mosaic grid has a pixel scale of 23.75 arcsec, which is comparable to the sizes of the regions from the original brick grids defined in Lewis et al. (2014). Assuming a distance modulus of 24.47 (McConnachie et al., 2005), a disk inclination of 78 deg (Tully, 1994), and a major axis position angle of 35 deg (de Vaucouleurs et al., 1995), the pixel scale is deprojected to a linear size of $dx = 440$ pc and $dy = 100$ pc approximately along the minor and major axes of M31, respectively. The synthetic flux maps therefore have a resolution that is firmly in the sub-kpc regime.

The final synthetic flux maps, $f_{X,\text{SFH},0}$ and $f_{X,\text{SFH}}$, are shown in Figures 3.2 (FUV) and 3.3 (NUV).

We used the synthetic flux maps to derive maps of A_X , the total extinctions in the FUV and NUV bands. The intrinsic and attenuated flux maps were converted into AB magnitudes (Table 3.1), $m_{X,\text{SFH},0}$ and $m_{X,\text{SFH}}$. The extinction maps were then calculated as the difference between the intrinsic and attenuated magnitudes, $A_X = m_{X,\text{SFH}} - m_{X,\text{SFH},0}$. We show the synthetic extinction maps with their corresponding synthetic flux maps in Figures 3.2 and 3.3.

A pixel weight map representing the coverage of the available PHAT data was also produced during the mosaicking process. Mosaic pixels fully within the PHAT survey border (excluding bricks 1 and 2 near the bulge) have a weight of 1, pixels fully outside the border have a weight of 0, and all other pixels have weights between 0 and 1 depending on the fraction of the pixel area within the survey border. Throughout this study we used the weight map to mask out all pixels not fully within the survey border so that our comparisons with observations are done on a full-pixel basis.

¹ <http://montage.ipac.caltech.edu/>

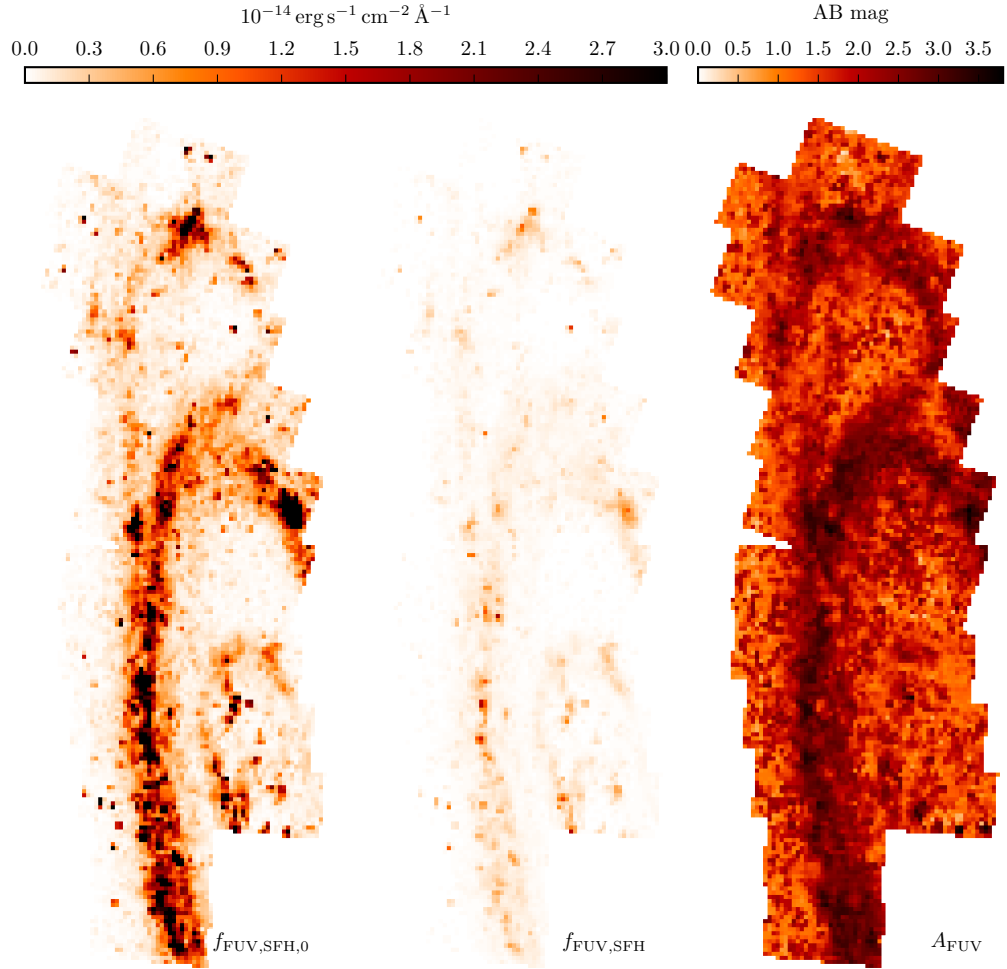


Figure 3.2 FUV flux modeled from the SFHs. The intrinsic flux, $f_{\text{FUV},\text{SFH},0}$, is shown in the left panel and the middle panel shows the flux attenuated according to the extinction model, $f_{\text{FUV},\text{SFH}}$ (also shown alongside the observed GALEX FUV flux in Figure 3.4). The FUV extinction, A_{FUV} , derived from $f_{\text{FUV},\text{SFH},0}$ and $f_{\text{FUV},\text{SFH}}$ is shown on the right.

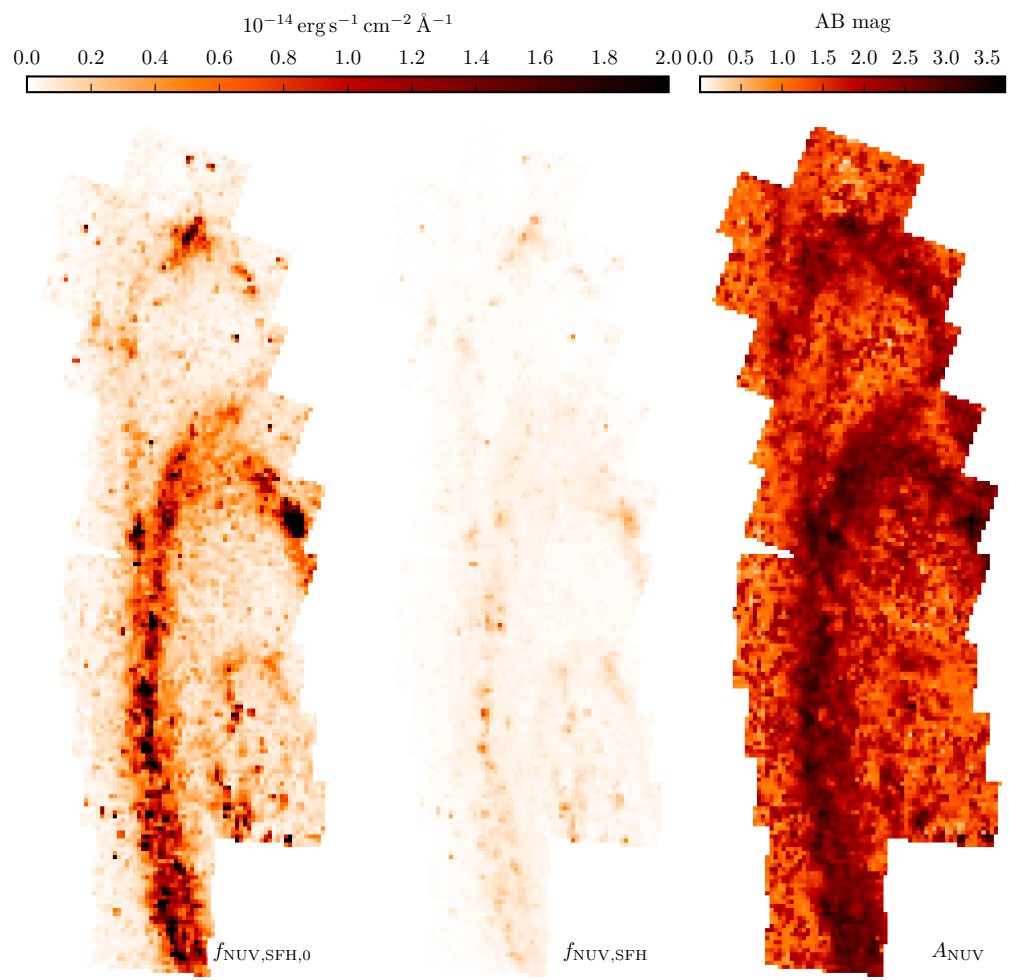


Figure 3.3 Same as Figure 3.2, but for the NUV filter.

3.3 Observations

We constructed maps of observed GALEX FUV and NUV flux, $f_{X,\text{obs}}$, to match the synthetic flux maps described in §3.2.2. We started with the intensity maps of four tiles in the GALEX Deep Imaging Survey (DIS Martin et al., 2005) covering the PHAT survey area (see Table 3.1). The tiles were converted from units of $\text{counts s}^{-1} \text{pixel}^{-1}$ into flux using the factors in Table 3.1. We then used Montage to reproject the flux tiles to the same template header as the synthetic flux mosaics (see §3.2). The individual tiles had slightly different background levels, so we had Montage automatically match the backgrounds before adding the tiles to form the final mosaic.

A small amount of background UV flux was present in the FUV and NUV mosaics, primarily due to scattering of UV photons from hot foreground stars in the Galaxy. We measured the mean background flux in a rectangular aperture in an off-galaxy area relatively devoid of stars in the reprojected, background matched tile PS.M31_MOS07. The measured background values were 5.22×10^{-19} and $3.47 \times 10^{-19} \text{ erg s}^{-1} \text{cm}^{-2} \text{\AA}^{-1} \text{arcsec}^{-2}$ (2.9×10^{-16} and $2.0 \times 10^{-16} \text{ erg s}^{-1} \text{cm}^{-2} \text{\AA}^{-1}$ per mosaic pixel) in FUV and NUV, respectively. We subtracted these values from the FUV and NUV mosaics to obtain the final observed UV flux maps for the PHAT survey area, $f_{X,\text{obs}}$, shown in Figures 3.4 (FUV) and Figure 3.5 (NUV).

3.4 SFR estimates

A common method for estimating the SFR of a target is to measure the integrated flux in one or more filters and then calculate the SFR using one of the flux-to-SFR calibrations available in the literature, e.g., (for UV flux) those discussed by Kennicutt (1998), Salim et al. (2007), Hao et al. (2011), Murphy et al. (2011), and Leroy et al. (2012); see also the review by Kennicutt & Evans (2012). We used this method to derive SFR maps for the PHAT survey area, which we can later compare with similar maps derived from the Lewis et al. (2014) SFH data, effectively extending the work of Simones et al. (2014) to a much larger and more diverse sample.

To calculate flux-based SFRs, we converted the $f_{X,\text{obs}}$ maps into AB magnitudes (Table 3.1), $m_{X,\text{obs}}$, which we corrected for extinction by subtracting the synthetic A_X maps (§3.2.2). The extinction-corrected maps were converted back into (specific) fluxes

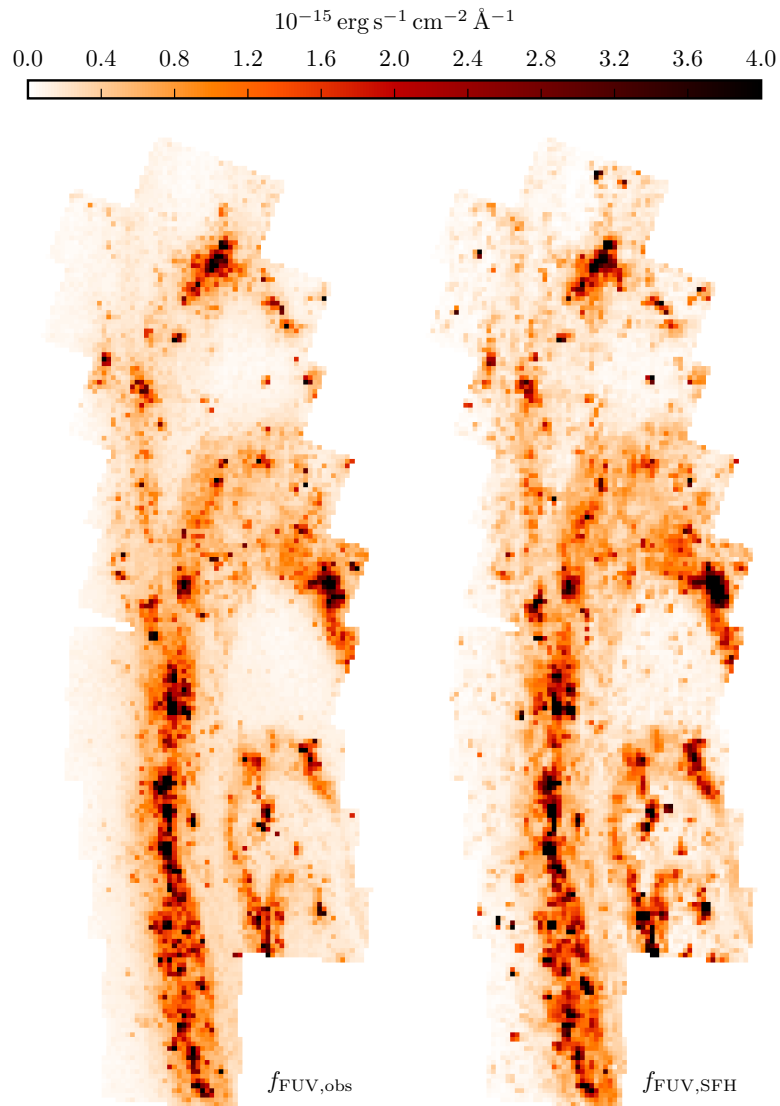


Figure 3.4 Observed FUV flux from GALEX, $f_{\text{FUV},\text{obs}}$ (left), and synthetic attenuated FUV flux from the SFHs, $f_{\text{FUV},\text{SFH}}$ (right). The observed map has been clipped to the PHAT survey border to match the synthetic map. The synthetic fluxes show excellent morphological agreement with the observed fluxes.

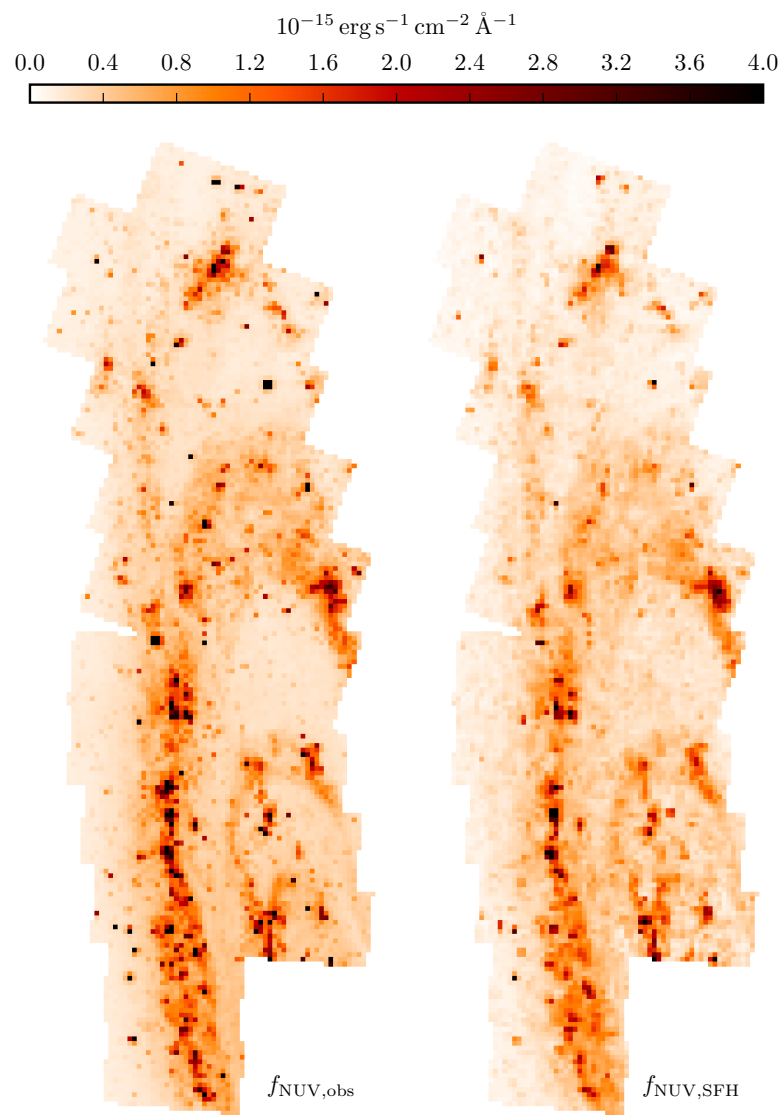


Figure 3.5 Same as Figure 3.4, but for the NUV filter.

($\text{erg s}^{-1} \text{cm}^{-2} \text{\AA}^{-1}$), then into total fluxes ($\text{erg s}^{-1} \text{cm}^{-2}$) by multiplying by the effective filter wavelength (1538.6 Å for FUV, 2315.7 Å for NUV; Morrissey et al., 2007). The total fluxes were converted into luminosities, L_X (erg s^{-1}), assuming a distance modulus of 24.47 (McConnachie et al., 2005). Finally, we applied the calibrations from Kennicutt (1998) with updates by Hao et al. (2011) and Murphy et al. (2011) (see the review by Kennicutt & Evans, 2012) to obtain the FUV and NUV flux-based SFR estimates, SFR_X , respectively:

$$\left(\frac{\text{SFR}_{\text{FUV}}}{M_\odot \text{yr}^{-1}} \right) = 10^{-43.35} \left(\frac{L_{\text{FUV}}}{\text{erg s}^{-1}} \right) \quad (3.1)$$

$$\left(\frac{\text{SFR}_{\text{NUV}}}{M_\odot \text{yr}^{-1}} \right) = 10^{-43.17} \left(\frac{L_{\text{NUV}}}{\text{erg s}^{-1}} \right) \quad (3.2)$$

These calibrations are based on stellar population synthesis using Starburst99 (Leitherer et al., 1999) and assuming a constant SFR over the last 100 Myr, the Kroupa (2001) IMF, a fully populated range of masses from 0.1 to $100 M_\odot$, and solar metallicity (Hao et al., 2011).

The most robust flux calibrations are those that rely on more than one part of the electromagnetic spectrum. An example of a hybrid estimator is the combination of GALEX FUV and Spitzer 24 μm fluxes, which simultaneously accounts for the direct starlight from newly-formed massive stars and the absorbed starlight processed and reradiated by dust (e.g., Leroy et al., 2012). However, we have limited our study to observations by GALEX, so we will only consider the simpler monochromatic FUV and NUV calibrations in Equations 3.1 and 3.2. We show the final SFR_X maps in Figure 3.6.

We also created a map for the mean SFR over the past 100 Myr of the SFHs, $\langle \text{SFR} \rangle_{100}$, which we show alongside the flux-based SFR maps in Figure 3.6. The 100 Myr limit represents the nominal timescale of UV emission and matches the timescale used by Hao et al. (2011) to derive the FUV and NUV flux calibrations.

Finally, we created another pair of flux-based SFR maps derived just as before, except instead we started with the intrinsic synthetic fluxes $f_{X,\text{SFH},0}$ described in §3.2.2. Because the fluxes were intrinsic, it was not necessary to apply an extinction correction before converting the fluxes into SFRs. The maps for the intrinsic flux-based SFR estimates, $\text{SFR}_{X,0}$, are shown in Figure 3.7.

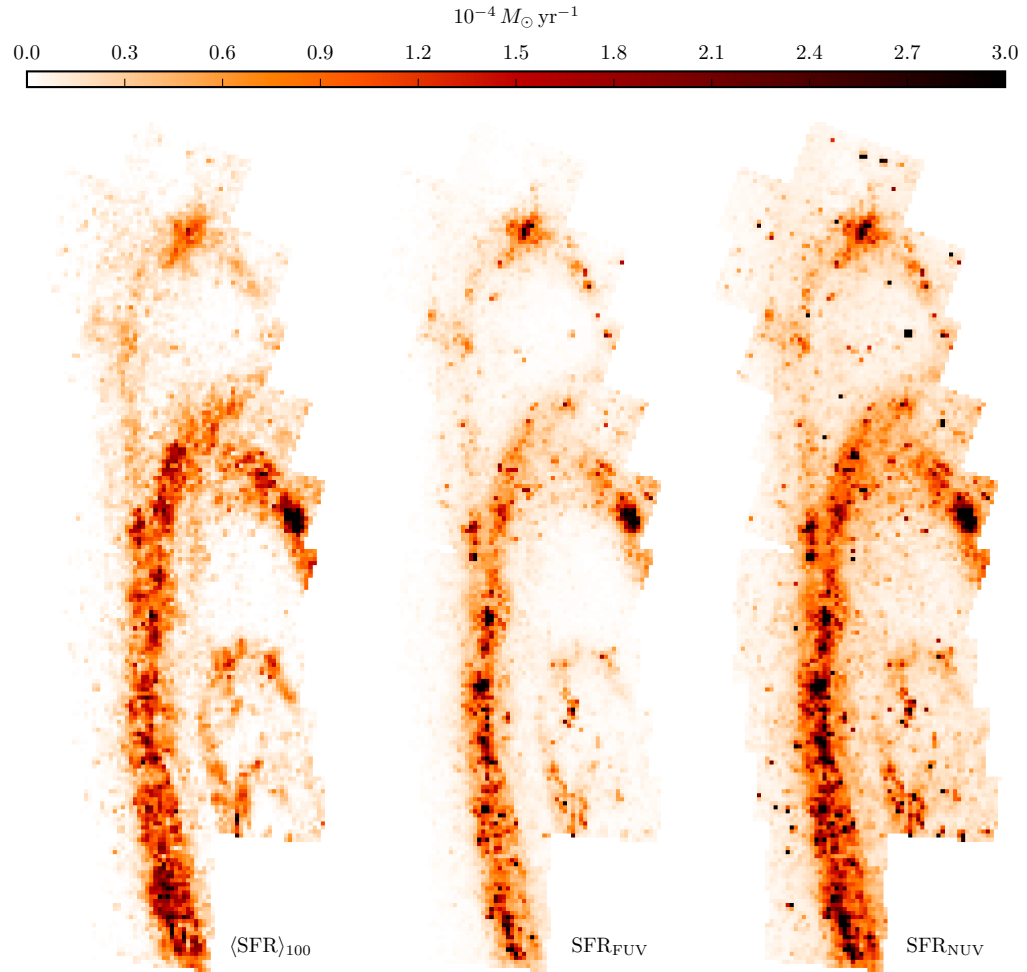


Figure 3.6 FUV and NUV flux-based SFRs, SFR_{FUV} (middle) and SFR_{NUV} (right), compared with $\langle \text{SFR} \rangle_{100}$ (left), the mean SFR over the last 100 Myr of the SFHs. The flux-based SFRs were derived from the observed GALEX fluxes, FUV_{obs} and NUV_{obs} (Figures 3.4 and 3.5), corrected for extinction using A_{FUV} and A_{NUV} (Figures 3.2 and 3.3). The SFR maps show good overall agreement.

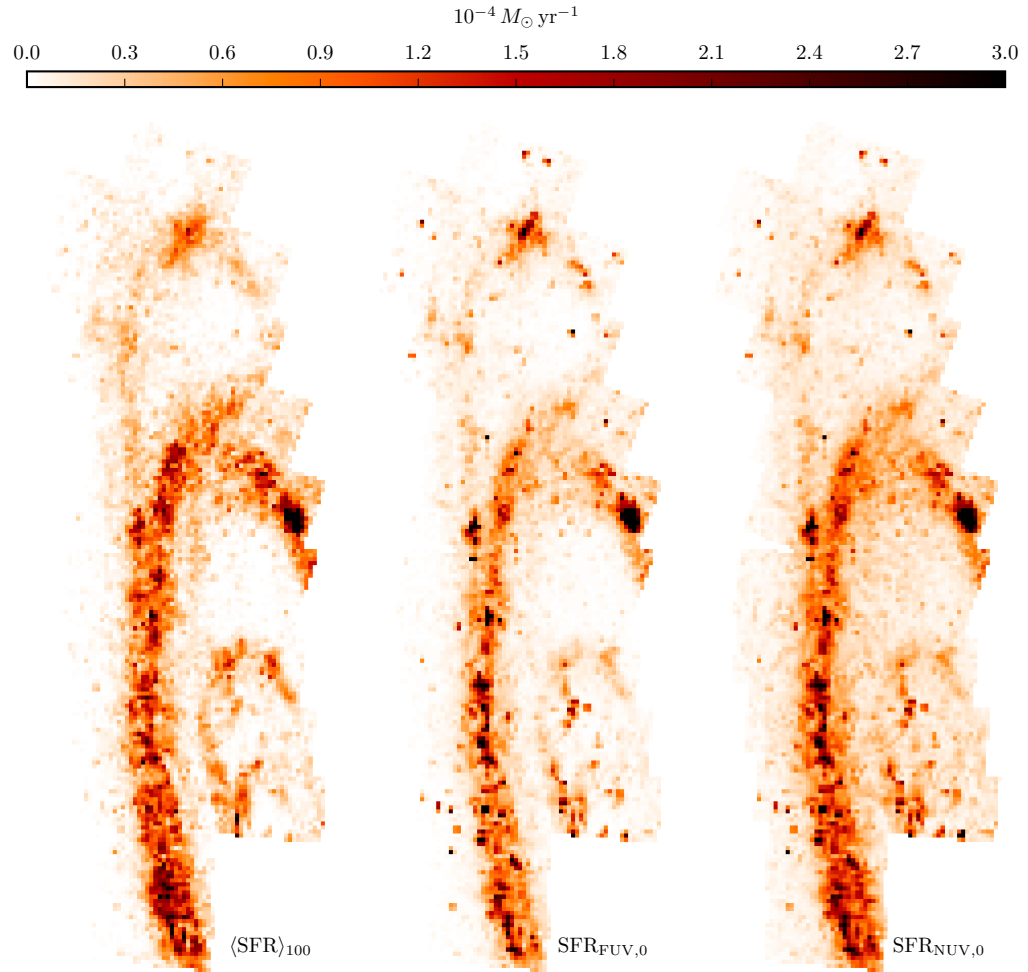


Figure 3.7 Same as Figure 3.6, but instead comparing $\langle \text{SFR} \rangle_{100}$ with $\text{SFR}_{\text{FUV},0}$ and $\text{SFR}_{\text{NUV},0}$, the SFRs from the synthetic intrinsic (i.e., unattenuated) fluxes from Figures 3.2 and 3.3. The synthetic intrinsic fluxes were derived assuming a fully populated IMF so there is no inconsistency with the flux calibration, which assumes the same. Like the SFRs based on observed flux, these SFRs also show good agreement with $\langle \text{SFR} \rangle_{100}$.

3.5 Discussion

3.5.1 Modeled flux

Figures 3.4 and 3.5 show remarkable overall qualitative agreement between the synthetic attenuated fluxes $f_{X,\text{SFH}}$ and the observed GALEX fluxes $f_{X,\text{obs}}$. In particular, all of the main features brighter than $\sim 10^{-15} \text{ erg s}^{-1} \text{ cm}^{-2} \text{ \AA}^{-1}$ in the observed maps are faithfully reproduced in the synthetic maps. This includes the main rings at ~ 5 , 10 , and 15 kpc from the bulge, and the large star-forming complexes found in PHAT bricks 15 and 21 . The $f_{\text{NUV},\text{obs}}$ map does show several point sources (most likely foreground stars) which are not present in the $f_{\text{NUV},\text{SFH}}$ map, but the synthetic maps were derived to simulate fluxes from *distributions* of stars in CMDs, not the stars individually.

We compare the synthetic and observed fluxes more quantitatively in Figures 3.8 (FUV) and 3.9 (NUV), which map the ratio of $f_{X,\text{SFH}}$ to $f_{X,\text{obs}}$ over the PHAT survey area. The Figures also show the flux ratios as a function of $f_{X,\text{obs}}$. We find that the log flux ratios follow normal distributions with mean $\mu = 7.62 \times 10^{-3}$ and standard deviation $\sigma = 2.37 \times 10^{-1}$ for FUV, and $\mu = -1.03 \times 10^{-1}$ and $\sigma = 1.59 \times 10^{-1}$ for NUV. In linear terms, the median flux ratios are 1.02 in FUV and 0.79 in NUV, with 68% confidence limits of 0.59 and 1.76 (FUV) and 0.55 and 1.14 (NUV). Note that in both filters, the median ratio is within the confidence interval of 1 , indicating that $f_{X,\text{SFH}}$ is consistent with $f_{X,\text{obs}}$ on average.

The overall agreement between $f_{X,\text{SFH}}$ and $f_{X,\text{obs}}$ shows that our modeling procedure is generally robust and justifies the several key assumptions that we and Lewis et al. (2014) used to derive $f_{X,\text{SFH}}$ from the CMDs. Specifically, we assumed an IMF, models describing stellar spectra and evolution, and an extinction model as well as an extinction curve. These form the foundation for much research in astronomy and encompass our current best understanding of stellar astrophysics and star formation. It is therefore reassuring that we can use all of this knowledge to derive SFHs, synthesize SEDs, and successfully recreate detailed maps of a galaxy, all from photometry in just two optical bands.

The Poisson uncertainties in $f_{X,\text{obs}}$ are relatively small. Assuming an average exposure time of 7×10^3 s in the FUV channel for the five DIS images in our study, the uncertainties are only a few percent at $f_{\text{FUV},\text{obs}} \sim 10^{-16} \text{ erg s}^{-1} \text{ cm}^{-2} \text{ \AA}^{-1}$ and a few

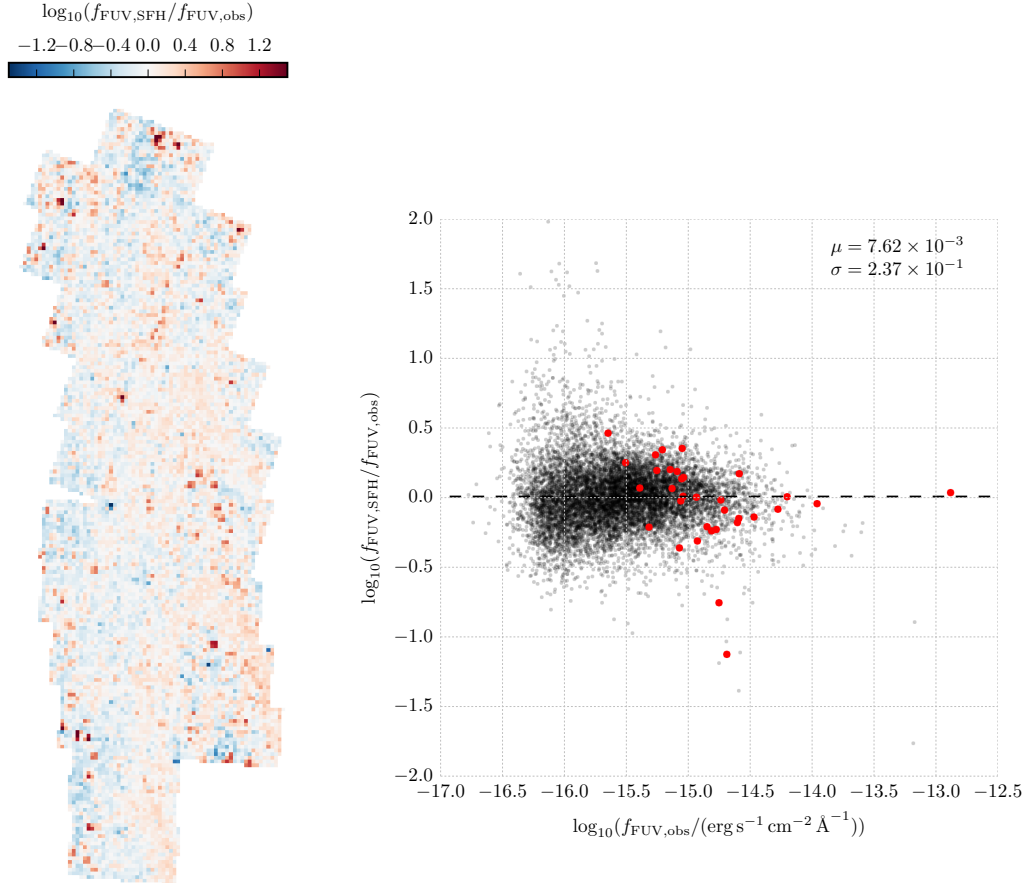


Figure 3.8 Ratio of the synthetic attenuated flux, $f_{\text{FUV,SFH}}$, to the GALEX observed flux, $f_{\text{FUV,obs}}$, in the FUV filter. The log flux ratios in the scatter plot follow a normal distribution with $\mu = 7.62 \times 10^{-3}$ (horizontal dashed line) and $\sigma = 2.37 \times 10^{-1}$. The median ratio is 1.02 with 68% confidence limits of 0.59 and 1.76. $f_{\text{FUV,SFH}}$ and $f_{\text{FUV,obs}}$ are therefore consistent on average. The flux ratio variance increases with decreasing observed flux, suggesting that the uncertainties are dominated by incomplete IMF sampling. The large red circles represent flux ratios for the UV-bright regions from Simones et al. (2014) and are consistent with the main sample. The map shows a fairly even spatial distribution for the flux ratios, with the most severely overestimated and underestimated pixels occurring primarily in the faint, off-arm areas of the galaxy, as shown in the scatter plot.

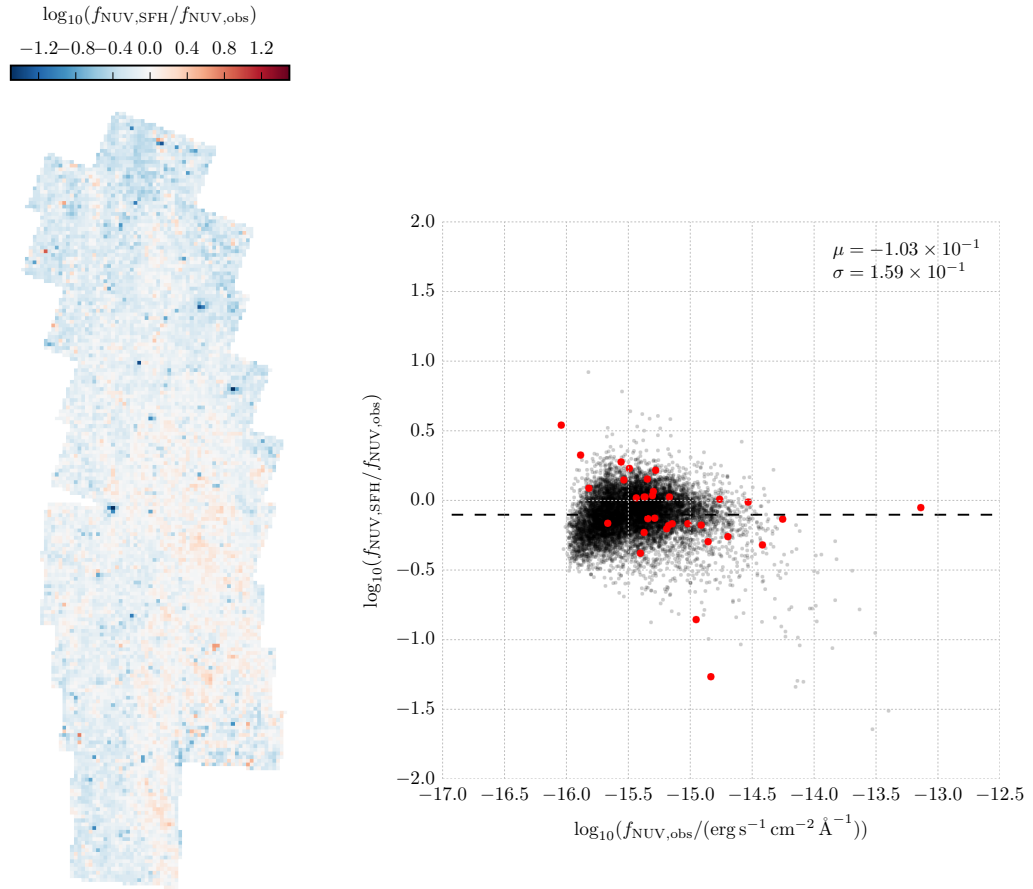


Figure 3.9 Same as Figure 3.8, but for the NUV filter. In this case, the log-normal distribution is characterized by $\mu = -1.03 \times 10^{-1}$ and $\sigma = 1.59 \times 10^{-1}$. The median ratio is 0.79 with 68% confidence limits of 0.55 and 1.14. $f_{\text{NUV,SFH}}$ and $f_{\text{NUV,obs}}$ are therefore consistent on average. The role of IMF sampling is not as important for $f_{\text{NUV,obs}}$, so the uncertainties in $f_{\text{NUV,SFH}}$ are somewhat smaller.

tenths of a percent at $f_{\text{FUV,obs}} \sim 10^{-14} \text{ erg s}^{-1} \text{ cm}^{-2} \text{ \AA}^{-1}$. The corresponding NUV uncertainties for an average exposure time of $6 \times 10^4 \text{ s}$ in the NUV channel are about one tenth of those in the FUV. However, Figures 3.8 and 3.9 show variances that are much larger than the Poisson uncertainties allow. These variances are therefore due essentially exclusively to systematic effects in the modeling process.

The primary systematic effect at play is most likely incomplete sampling of the IMF (Elmegreen, 1999; Bastian et al., 2010; Fumagalli et al., 2011; da Silva et al., 2012, 2014). This is supported by the observation that the variance in the flux ratios increases with decreasing pixel brightness, especially in the FUV filter. Also, the $f_{X,\text{SFH}}$ maps show somewhat more uneven, noisy backgrounds, i.e., faint pixels in the off-arm areas of M31, compared with the $f_{X,\text{obs}}$ maps. The faint pixels are associated with low star formation (SF) activity and, because all pixels are the same size, have fewer stars than the brighter pixels covering the arms and main star-forming regions. This leads to a violation of the full-IMF assumption used by FSPS and other stellar population synthesis codes.

Whenever the number of stars in a population is sufficiently small, the discreteness of the stellar mass distribution becomes important in determining the observed luminosity compared with other populations of the same total mass. This is because any given sampling of the total mass can easily have a higher (or lower) proportion of high-mass stars than expected for a fully populated IMF. There will therefore be more (or less) high-energy photons than stellar population synthesis models suggest, and the synthetic UV flux will be underestimated (or overestimated). In other words, when a stellar population is small, the same total mass could be produced by a variety of mass functions (samplings of the IMF), where each mass function has its own unique luminosity. This results in a variance in the flux ratios that increases with decreasing surface brightness. We observe this trend to be more pronounced in FUV, as mentioned above, and is caused by the increased sensitivity of $f_{\text{FUV,obs}}$ to slight variations in the number of high-mass stars relative to $f_{\text{NUV,obs}}$.

Although IMF sampling more severely affects the fainter pixels, the sub-kpc resolution of our flux maps results in small pixel areas such that IMF sampling is likely the dominant source of the variance for all of the flux ratios. Accounting for projection effects in the disk, the physical area of each pixel is $4.4 \times 10^4 \text{ pc}^2$ (§3.2.2). This

is approximately equal to the average area of the UV-bright regions considered by Simones et al. (2014), who showed that the uncertainties in fluxes modeled for UV-bright regions tapers off with increasing area. They also showed that combining several small regions into a larger \sim kpc-sized region greatly improved the agreement between the synthetic and observed fluxes. These results show that the best way to comply with the full-IMF assumption and reduce the uncertainties in $f_{X,\text{SFH}}$ is to make the mosaic pixel size larger. Naturally, reducing uncertainties this way comes at the cost of decreased spatial resolution in the flux maps. Exploring simultaneously the effects of both surface brightness *and* pixel area on this fundamental, stochastic variance is an interesting topic for future study.

We have added to Figures 3.8 and 3.9 the flux ratios for the sample of UV-bright regions in Simones et al. (2014). Although the UV-bright regions vary in size and come from one small part of M31, their flux ratios appear to agree with the overall distribution for the rest of the galaxy. Also, other than the increased variance in the faint areas, we find no obvious trends in the mean or variance of the flux ratios with respect to environment or distance from the bulge. Therefore, we conclude that the flux modeling procedure may be successfully applied to any population in environments similar to M31. We estimate the uncertainties in synthesizing fluxes for sub-kpc regions to be $+0.74/-0.43$ and $+0.35/-0.24$ times the observed flux in FUV and NUV, respectively, driven mostly by incomplete sampling of the IMF. The $f_{\text{FUV,SFH}}$ uncertainties are consistent with Simones et al. (2014), who found an uncertainties of $+0.95/-0.47$ for the synthetic FUV fluxes of the UV-bright regions.

3.5.2 SFR estimates from FUV flux

As with the synthetic and observed fluxes, the flux-based SFR maps in Figures 3.6 and 3.7 show good overall morphological agreement with the $\langle \text{SFR} \rangle_{100}$ map. We compare the SFRs more closely in Figures 3.10 and 3.11, in which we map the ratio of SFR_X to $\langle \text{SFR} \rangle_{100}$ and plot the SFR ratio as a function of $\langle \text{SFR} \rangle_{100}$. A major feature in both figures is the marked contrast in the SFR ratios between the high and low SFR areas. The areas with low $\langle \text{SFR} \rangle_{100}$, corresponding to the faint areas in Figures 3.4 and 3.5, host nearly all of the very highest SFR ratios in the entire survey area and none of the low or moderate ratios. The pixels in these areas make up the downward sloping tails

seen at low $\langle \text{SFR} \rangle_{100}$ in the scatter plots in Figures 3.6 and 3.7.

The low-SFR tails are distinctly linear, with slopes of -1 and intercepts of -6.0 and -5.4 for the FUV and NUV SFR ratios, respectively. In log space, a straight line with -1 slope indicates that SFR_X becomes constant with a value equal to $10^{-6.0} = 9.8 \times 10^{-7} M_\odot \text{ yr}^{-1}$ for FUV and $10^{-5.4} = 4.1 \times 10^{-6} M_\odot \text{ yr}^{-1}$ for NUV. Because SFR_X is directly proportional to $f_{X,\text{obs}}$, these SFR constants suggest that there must be a constant baseline flux present in the galaxy that becomes more apparent as $\langle \text{SFR} \rangle_{100}$ decreases to very small values. In other words, the linear relationship between flux and SFR assumed by the flux calibrations in Equations 3.1 and 3.2 appear to break down completely below $\langle \text{SFR} \rangle_{100}$ approximately one to a few $\times 10^{-6} M_\odot \text{ yr}^{-1}$.

Using the flux calibrations in reverse, we find that the above SFR constants translate into $f_{\text{FUV},\text{obs}} \sim 2 \times 10^{-16} \text{ erg s}^{-1} \text{ cm}^{-2} \text{ \AA}^{-1}$ and $f_{\text{NUV},\text{obs}} \sim 8 \times 10^{-16} \text{ erg s}^{-1} \text{ cm}^{-2} \text{ \AA}^{-1}$ (or -15.7 and -15.1 in log flux, respectively). All of Figures 3.6, 3.7, 3.8, and 3.9 show that these flux and SFR limits make the FUV and NUV flux-to-SFR calibrations completely unreliable for approximately half of the pixels in the survey area. This demonstrates the importance of warnings in the literature (e.g., Murphy et al., 2011; Kennicutt & Evans, 2012; Leroy et al., 2012) that flux calibrations are problematic on sub-kpc scales. We therefore limit our analysis of the SFR ratios in Figures 3.10 and 3.11 to pixels with $\langle \text{SFR} \rangle_{100}$ greater than a conservative threshold of $10^{-5} M_\odot \text{ yr}^{-1}$.

Considering only pixels with $\langle \text{SFR} \rangle_{100} \geq 10^{-5} M_\odot \text{ yr}^{-1}$, we treat the SFR ratios as having log-normal distributions with $\mu = -2.46 \times 10^{-1}$ and $\sigma = 2.61 \times 10^{-1}$ for FUV, and $\mu = 9.27 \times 10^{-2}$ and $\sigma = 2.33 \times 10^{-1}$ for NUV. The median ratios are 0.57 (FUV) and 1.24 (NUV), with 68% confidence limits of 0.31 and 1.04 (FUV) and 0.72 and 2.12 (NUV), indicating that SFR_X is consistent with $\langle \text{SFR} \rangle_{100}$ on average. However, given the small uncertainties for the observed fluxes (§3.2.2) the large variances of the SFR ratios suggest that significant systematic effects are involved in the flux-to-SFR conversion process.

One of the assumptions made by the flux calibrations in Equations 3.1 and 3.2 is that the input flux is produced by a stellar population with solar metallicity. The mean metallicity of the brick grid regions (§3.2.2) is $[\text{M}/\text{H}] = -0.06$ with a standard deviation of 0.09, so the mosaic pixels are consistent with solar metallicity on average. From Simones et al. (2014), overestimating $[\text{M}/\text{H}]$ by 0.1 dex causes the SFR to be

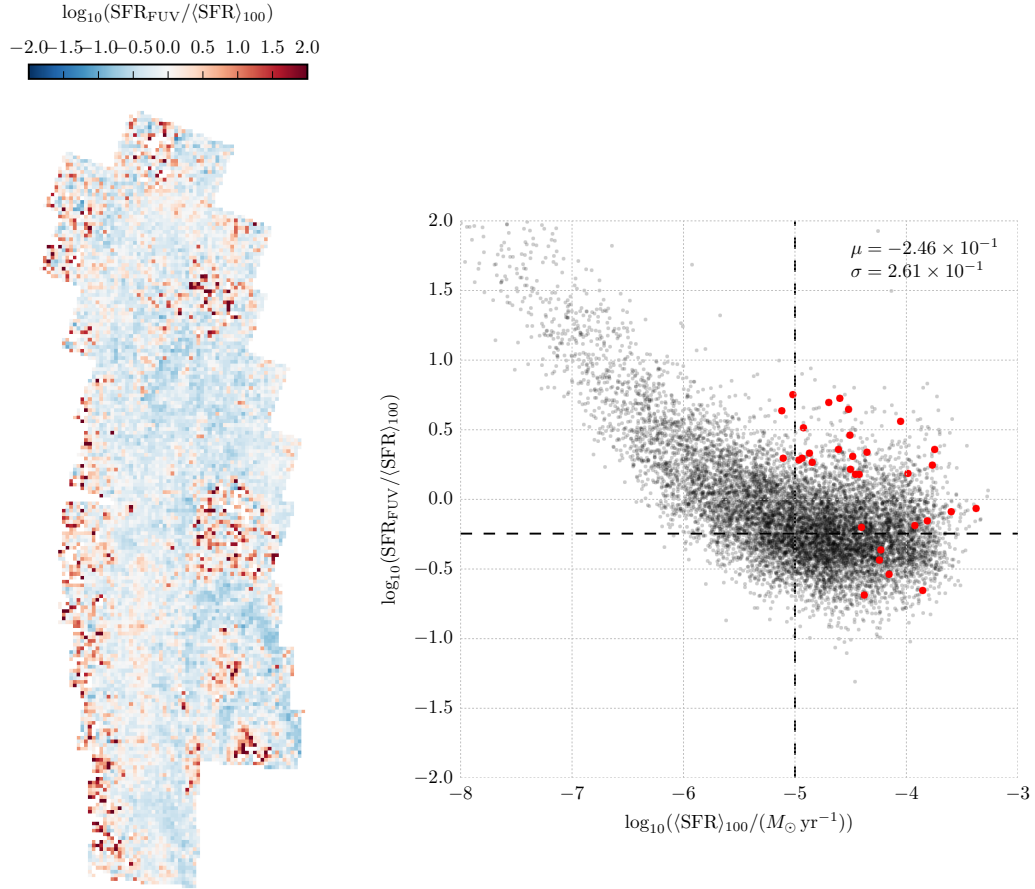


Figure 3.10 Ratio of the SFR based on the observed extinction-corrected FUV flux, SFR_{FUV} , to the 100 Myr mean of the SFH, $\langle \text{SFR} \rangle_{100}$. The log SFR ratios show a linear tail feature with -1 slope and -6.0 intercept, implying that SFR_{FUV} becomes constant for $\langle \text{SFR} \rangle_{100} < 9.8 \times 10^{-7} M_{\odot} \text{ yr}^{-1}$. We constrain our analysis to pixels with $\langle \text{SFR} \rangle_{100} 10^{-5} M_{\odot} \text{ yr}^{-1}$ (vertical dashed line). Above this limit, the log SFR ratios follow a normal distribution with $\mu = -2.46 \times 10^{-1}$ (horizontal dashed line) and $\sigma = 2.61 \times 10^{-1}$. The median ratio is 0.57 with 68% confidence limits of 0.31 and 1.04, most likely due to incomplete IMF sampling. SFR_{FUV} and $\langle \text{SFR} \rangle_{100}$ are therefore consistent on average. The large red circles represent SFR ratios for the UV-bright regions from Simones et al. (2014) and are consistent with the main sample. Apart from the faint, off-arm areas responsible for the tail feature, the map shows a fairly even spatial distribution for the SFR ratios.

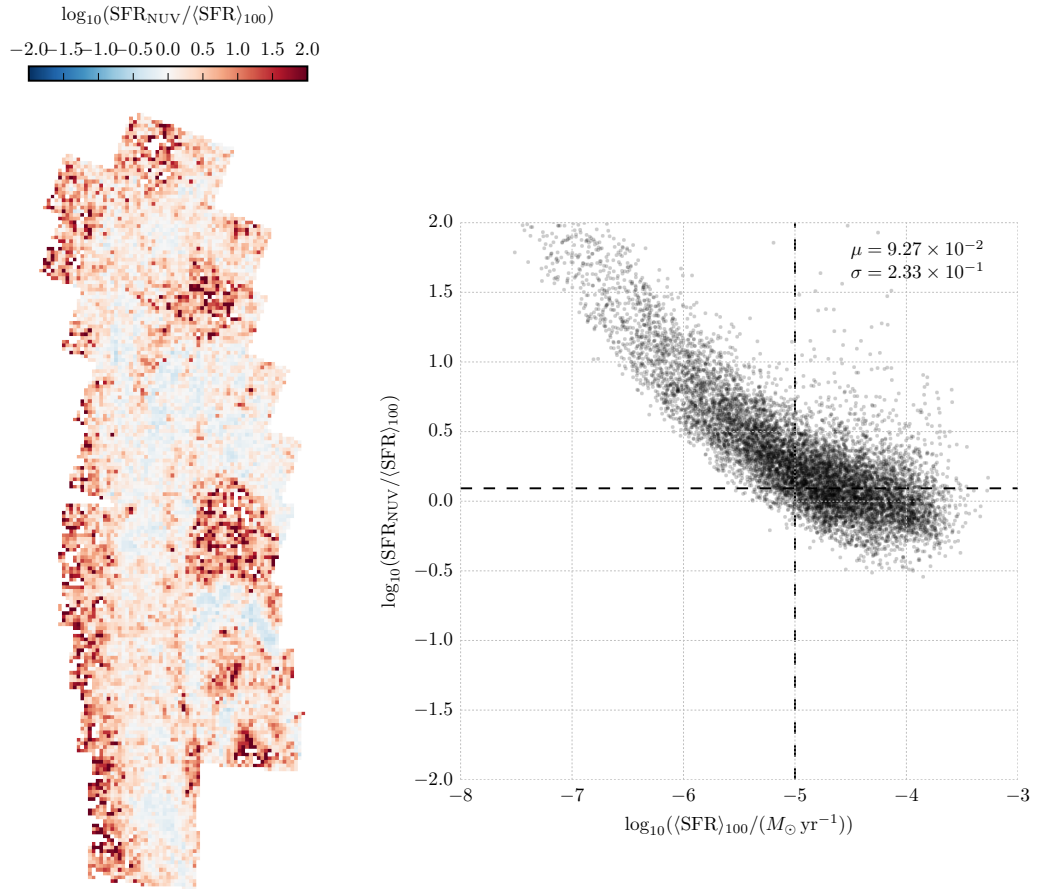


Figure 3.11 Same as Figure 3.10, but for the NUV filter. In this case, the linear tail has an intercept of -5.4 such that SFR_{NUV} becomes constant for $\langle \text{SFR} \rangle_{100} < 4.1 \times 10^{-6} M_\odot \text{yr}^{-1}$. The log-normal distribution is characterized by $\mu = 9.27 \times 10^{-2}$ and $\sigma = 2.33 \times 10^{-1}$. The median ratio is 1.24 with 68% confidence limits of 0.72 and 2.12. SFR_{NUV} and $\langle \text{SFR} \rangle_{100}$ are therefore consistent on average.

overestimated by 0.015 dex. Therefore, the variation in the metallicities contributes only 0.01 dex to the variation in the log SFR ratios, making metallicity unimportant for the overall SFR ratio distribution.

Like the modeled fluxes in §3.5.1, the flux calibrations also assume a fully populated IMF, causing SFR_X to be overestimated (or underestimated) for pixels with an apparent excess (or lack) of massive stars. Also, if incomplete IMF sampling is the primary source of the variance in the log SFR ratios, as it is for the log flux ratios, then the σ parameters of the log-normal distributions should be similar. Indeed, we find consistent variances between Figures 3.8 and 3.10 and between Figure 3.9 and 3.11.

The flux calibrations also assume a constant SFH over the last 100 Myr. The analysis of UV-bright regions in Simones et al. (2014) showed that inconsistencies with this assumption can contribute at least as much to the total uncertainty in SFR_{FUV} as incomplete IMF sampling. To isolate the effect of SFH variability, we recreate in Figures 3.12 and 3.13 the maps and plots of Figures 3.10 and 3.11 using $\text{SFR}_{X,0}$, the SFRs derived from the synthetic intrinsic fluxes (see §3.2.2) instead of SFR_X .

$\text{SFR}_{X,0}$ is a useful quantity because it is determined self-consistently. Converting a SFR (e.g., for an age bin in a SFH) into a flux as demonstrated in §3.2.2 is conceptually the inverse of converting a flux into a SFR via Equations 3.1 and 3.2. Also, both the synthetic fluxes and the flux calibrations assume a well-sampled IMF from Kroupa (2001). The only effect that would cause a difference between $\langle \text{SFR} \rangle_{100}$ and $\text{SFR}_{X,0}$ for a given SFH is variability in the SFH itself. We find little difference between the SFR ratio distributions in Figures 3.10 and 3.12 and in Figures 3.11 and 3.13. If SFH variability does play a role in the SFR ratio variances, then we cannot detect it on a statistically significant basis and it is therefore not a major contributor to the SFR_X and $\text{SFR}_{X,0}$ uncertainties.

The FUV SFR ratios from Simones et al. (2014) are shown in Figures 3.10 and 3.12 and appear to follow the main distributions for the main sample. Comparing the μ and σ values between the two samples, we find that the means are consistent. Part of the discussion in Simones et al. (2014) concerned possible explanations for the apparent overestimation of SFRs relative to $\langle \text{SFR} \rangle_{100}$. However, in the context of our larger, survey-wide sample we see that the SFR ratios of the UV-bright regions really are consistent on average.

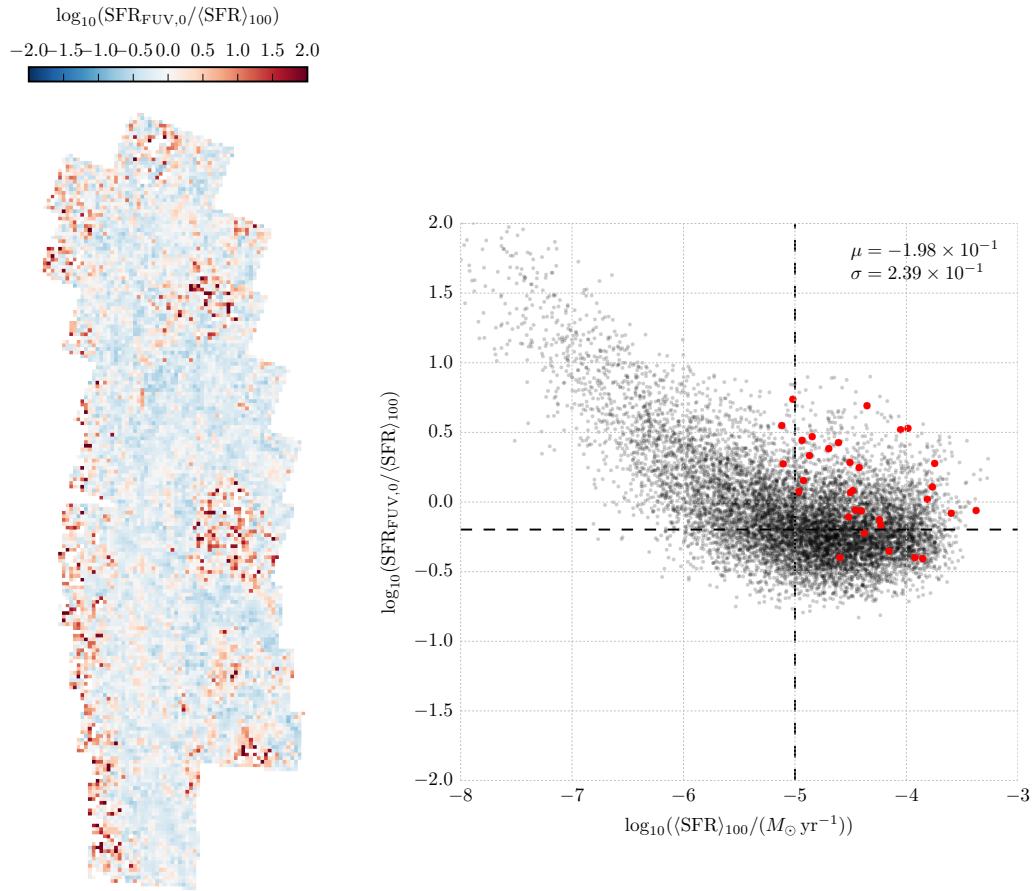


Figure 3.12 Same as Figure 3.10, but based on synthetic intrinsic flux, $\text{SFR}_{\text{FUV},0}$. The log-normal distribution is characterized by $\mu = -1.98 \times 10^{-1}$ and $\sigma = 2.39 \times 10^{-1}$. The median ratio is 0.63 with 68% confidence limits of 0.37 and 1.10. $\text{SFR}_{\text{FUV},0}$ and $\langle \text{SFR} \rangle_{100}$ are therefore consistent on average. The results here are similar to Figure 3.10, suggesting that SFH variability does not significantly affect the SFR_{FUV} uncertainties.

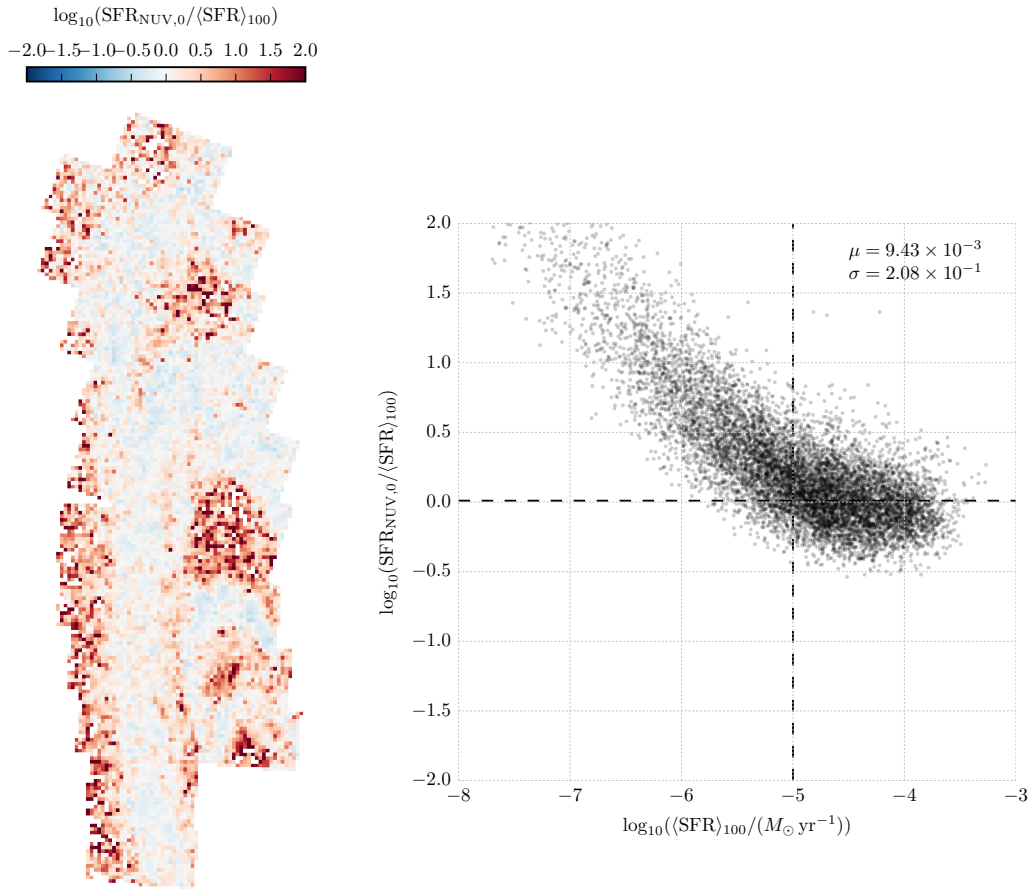


Figure 3.13 Same as Figure 3.11, but based on synthetic intrinsic flux, $\text{SFR}_{\text{NUV},0}$. The log-normal distribution is characterized by $\mu = 9.43 \times 10^{-3}$ and $\sigma = 2.08 \times 10^{-1}$. The median ratio is 1.02 with 68% confidence limits of 0.63 and 1.65. $\text{SFR}_{\text{NUV},0}$ and $\langle \text{SFR} \rangle_{100}$ are therefore consistent on average. The results here are similar to Figure 3.11, suggesting that SFH variability does not significantly affect the SFR_{NUV} uncertainties.

We do not observe in Figures 3.10, 3.11, 3.12, or 3.13 any environmental trends for the mean or variance of SFR_X and $\text{SFR}_{X,0}$, with the exception of the faintest areas of the galaxy responsible for the tails in the log SFR ratios distributions. Deriving SFRs from published flux calibrations is therefore generally a safe practice for environments like M31, *but only as long as the resulting SFRs are greater than $\sim 10^{-5} M_\odot \text{ yr}^{-1}$* . When applied to sub-kpc regions, we estimate the resulting uncertainties to be $+0.47/-0.26$ (FUV) and $+0.88/-0.52$ (NUV) times the true, underlying 100 Myr-mean SFR. The SFR_{FUV} uncertainty is rather less than the $+2.15/-0.88$ uncertainty found by Simones et al. (2014).

Finally, we evaluate the flux calibrations in Equations 3.1 and 3.2 for \sim galaxy-sized scales, as they are perhaps more commonly be used, by measuring the global SFR for the entire PHAT survey area. Summing up all of the pixels in Figure 3.6, we find that $\langle \text{SFR} \rangle_{100} = 0.30 M_\odot \text{ yr}^{-1}$, consistent with Lewis et al. (2014). In comparison, the global flux-based SFRs are $0.22 M_\odot \text{ yr}^{-1}$ for FUV and $0.43 M_\odot \text{ yr}^{-1}$ for NUV. If we adopt the estimated uncertainties mentioned earlier in this section, then the global flux-based SFRs are well within uncertainty of $\langle \text{SFR} \rangle_{100}$. However, as larger areas are considered, IMF sampling effects should eventually disappear and the variances in the SFR ratios should correspondingly decrease. Therefore, our estimated uncertainties should be considered firm upper limits when applied to galaxies. The global SFR ratios (flux-based to mean) are 0.73 and 1.43 for FUV and NUV, respectively. Why these ratios are larger than the median ratios above is not yet understood.

3.6 Conclusion

We have used star formation histories (SFHs) to model the spectral energy distributions (SEDs) of over 9000 sub-kpc regions in M31 and produce detailed maps of synthetic UV flux across the entire area covered by the Panchromatic Hubble Andromeda Treasury (PHAT). This work is an extensive follow-up to the analysis of Simones et al. (2014), which involved only 33 ultraviolet (UV)-bright regions from a small portion of the galaxy. The SFHs were derived by Lewis et al. (2014) using F475W and F814W photometry from the PHAT survey. Both intrinsic and attenuated SEDs were derived from the SFHs using the Flexible Stellar Population Synthesis (FSPS) code. These were convolved with

the Galaxy Evolution Explorer (GALEX) FUV and NUV response curves to obtain the synthetic intrinsic fluxes, $f_{X,\text{SFH},0}$, as well as the synthetic attenuated fluxes, $f_{X,\text{SFH}}$. All of the flux values were then assembled into an overall map, or mosaic, using Montage. The mosaic pixels corresponded to physical areas of $4.4 \times 10^4 \text{ pc}^2$. We constructed corresponding maps for the observed flux, $f_{X,\text{obs}}$, using GALEX Deep Imaging Survey (DIS) images.

The $f_{X,\text{SFH}}$ maps agreed with the $f_{X,\text{obs}}$ maps very well with respect to the broad morphology of M31, faithfully reproducing all of the main features brighter than $\sim 10^{-15} \text{ erg s}^{-1} \text{ cm}^{-2} \text{ \AA}^{-1}$. We found the log ratios of $f_{X,\text{SFH}}$ to $f_{X,\text{obs}}$ to be log-normally distributed with $\mu = 7.62 \times 10^{-3}$ and $\sigma = 2.37 \times 10^{-1}$ for FUV, and $\mu = -1.03 \times 10^{-1}$ and $\sigma = 1.59 \times 10^{-1}$ for NUV. The median flux ratios were 1.02 in FUV and 0.79 in NUV, with 68% confidence limits of 0.59 and 1.76 (FUV) and 0.55 and 1.14 (NUV). In both filters, the median ratio was within the confidence interval of 1, indicating that $f_{X,\text{SFH}}$ was consistent with $f_{X,\text{obs}}$ on average. Due to the small pixel areas, the primary source of the variance in the log flux ratios was most likely related to incomplete sampling of the IMF.

We found no obvious trends in the flux ratios with respect to environment, except for in the faintest, off-arm areas of the M31 where the variances in the flux ratios were noticeably larger. We conclude that fluxes may be successfully modeled from SFHs for any population in environments similar to M31. For our sub-kpc regions, we estimate the synthetic flux uncertainties to be $+0.74/-0.43$ and $+0.35/-0.24$ in FUV and NUV, respectively. Results from previous work on UV-bright regions by Simones et al. (2014) were consistent with our results.

The overall agreement between the observed and synthetic fluxes is remarkable considering that our flux modeling procedure was dependent on several key assumptions. Specifically, we assumed an IMF, models describing stellar spectra and evolution, and an extinction model as well as an extinction curve. These form the foundation for much research in astronomy and encompass our current best understanding of stellar astrophysics and star formation. It is reassuring that we can use all of this knowledge to successfully recreate detailed maps of a galaxy from photometry in just two optical bands.

We used flux calibrations from Kennicutt (1998) with updates by Hao et al. (2011)

and Murphy et al. (2011) to estimate SFRs based on observed UV flux, SFR_X . The $f_{X,\text{obs}}$ maps were first corrected for extinction using the synthetic attenuated and intrinsic fluxes. We also calculated the 100 Myr mean SFR from the SFHs, $\langle \text{SFR} \rangle_{100}$. We found that the faintest areas of M31 had the highest ratios of SFR_X to $\langle \text{SFR} \rangle_{100}$ and formed a linear tail feature in plots of the SFR ratio versus $\langle \text{SFR} \rangle_{100}$. These tails were the result of a distinct breakdown of the linear relationship between flux and SFR which underpins the flux calibration method. We estimated a conservative threshold of $\text{SFR} \sim 10^{-5} M_\odot \text{ yr}^{-1}$ below which flux calibration should not be used.

For the pixels above this threshold, we found the SFR ratios to be log-normally distributed with $\mu = -2.46 \times 10^{-1}$ and $\sigma = 2.61 \times 10^{-1}$ for FUV, and $\mu = 9.27 \times 10^{-2}$ and $\sigma = 2.33 \times 10^{-1}$ for NUV. The median ratios are 0.57 (FUV) and 1.24 (NUV), with 68% confidence limits of 0.31 and 1.04 (FUV) and 0.72 and 2.12 (NUV), indicating that SFR_X is consistent with $\langle \text{SFR} \rangle_{100}$ on average. As with the flux ratios, incomplete sampling of the IMF was the main source of the variance in the SFR ratios. We also considered deviations from solar metallicity as well as SFH variability, and found that they were far less important for the overall variances in the SFR ratios than IMF sampling.

Other than the faintest, off-arm areas which responsible for the tail feature in the SFR ratio distributions, there were no found no obvious trends in the SFR ratios with respect to environment. We determine that the flux calibration method is safely applicable to environments similar to M31, *but only as long as the resulting SFRs are greater than $\sim 10^{-5} M_\odot \text{ yr}^{-1}$* . We estimate the SFR uncertainties for our sub-kpc regions to be $+0.47/-0.26$ (FUV) and $+0.88/-0.52$ (NUV) times the true, underlying 100 Myr-mean SFR. The SFR_{FUV} uncertainty is rather less than the $+2.15/-0.88$ uncertainty previously found by Simones et al. (2014).

We also measured global SFRs for the entire PHAT survey area. The global $\langle \text{SFR} \rangle_{100}$ value was $0.30 M_\odot \text{ yr}^{-1}$, while the UV flux-based values were $SFR_{\text{FUV}} = 0.22 M_\odot \text{ yr}^{-1}$ and $SFR_{\text{NUV}} = 0.43 M_\odot \text{ yr}^{-1}$. The flux-based global SFRs are consistent with the global $\langle \text{SFR} \rangle_{100}$ value to within the uncertainties derived from the SFR maps. However, the variances in the SFR ratios due to IMF sampling is expected to decrease for larger areas, so our estimated uncertainties should be considered firm upper limits when applied to galaxies. The global SFR ratios (flux-based to mean) are 0.73 and 1.43 for FUV and

NUV, respectively. Why these ratios are larger than the median ratios above is not yet understood.

This research has made use of NASA’s Astrophysics Data System Bibliographic Services and the NASA/IPAC Extragalactic Database (NED), which is operated by the Jet Propulsion Laboratory, California Institute of Technology, under contract with the National Aeronautics and Space Administration. This work was supported by the Space Telescope Science Institute through GO-12055. Support for D. R. W is provided by NASA through Hubble Fellowship grant HST-HF-51331.01 awarded by the Space Telescope Science Institute, which is operated by the Association of Universities for Research in Astronomy, Inc., under NASA contract NAS 5-26555. This research made use of Astropy, a community-developed core Python package for Astronomy (Astropy Collaboration et al., 2013), as well as NumPy and SciPy (Oliphant, 2007), IPython (Pérez & Granger, 2007), and Matplotlib (Hunter, 2007). This research made use of Montage, funded by the National Aeronautics and Space Administration’s Earth Science Technology Office, Computation Technologies Project, under Cooperative Agreement Number NCC5-626 between NASA and the California Institute of Technology. Montage is maintained by the NASA/IPAC Infrared Science Archive.

Chapter 4

Summary

4.1 Tracing star formation with ultraviolet flux: results from sub-kpc regions

In this study, we have derived the recent (< 500 Myr) SFHs of 33 UV-bright regions in M31 using optical HST observations from PHAT. The regions were defined by K09 based on GALEX FUV surface brightness and have areas ranging from 8×10^3 to 1.5×10^6 pc 2 . We used the SFH code MATCH to fit the CMDs of the regions and measure their the SFHs based on the resolved stars from the PHAT photometry. We modeled the extinction in the regions using a foreground parameter and a differential parameter, which were optimized for each region to find the best-fit SFH.

We used FSPS to model both the intrinsic and reddened FUV and NUV magnitudes of the regions based on their SFHs. The differences between the modeled reddened and the observed FUV magnitudes, $\text{FUV}_{\text{SFH}} - \text{FUV}_{\text{obs}}$, followed a normal distribution with $\mu = 0.09$ and $\sigma = 0.3$. On average, the FUV_{SFH} values were consistent with the FUV_{obs} values, confirming the reliability of the SFHs, our extinction model, and the Cardelli et al. (1989) extinction curve. We attribute the scatter in the flux ratios to the assumption made by FSPS that the IMF is fully populated while the actual distribution of stellar masses becomes more discrete as smaller regions are considered.

The observed, extinction-corrected FUV magnitudes were converted into SFRs, SFR_{FUV} , using the FUV flux calibration from Kennicutt (1998) with updates by Hao

et al. (2011) and Murphy et al. (2011). We also derived the mean SFRs for the last 100 Myr of the SFHs, $\langle \text{SFR} \rangle_{100}$. The $\text{SFR}_{\text{FUV}}/\langle \text{SFR} \rangle_{100}$ ratios were log-normally distributed with $\mu = 0.2$ and $\sigma = 0.4$. Overall, the SFR_{FUV} values were consistent with the $\langle \text{SFR} \rangle_{100}$ values, though a small amount of the offset was attributable to inconsistencies with the metallicity assumed by the flux calibration.

The intrinsic modeled FUV magnitudes were also converted into SFRs, $\text{SFR}_{\text{FUV},0}$, which were free from biases due to extinction corrections and IMF sampling. The log-normal for the $\text{SFR}_{\text{FUV},0}/\langle \text{SFR} \rangle_{100}$ ratios had $\mu = 0.1$ and $\sigma = 0.3$, indicating that assuming a constant SFR (implicit in the flux calibration) for regions with highly variable SFHs is an important source of scatter. We conclude that the total scatter in the $\text{SFR}_{\text{FUV}}/\langle \text{SFR} \rangle_{100}$ ratio is due to the assumptions of a full IMF and a constant SFR in regions where discrete sampling of the IMF and high variability in the SFHs are important. Combined, these effects result in a factor of 2.5 uncertainty in the FUV-based SFRs. Although there is a significant lack of regions in our sample with areas between 10^5 and 10^6 pc^2 , we estimate that discrete IMF sampling and SFH variability become important below 10^5 pc^2 , or scales of a few hundred pc.

Ages and masses were derived for the regions by K09 from observed FUV–NUV color and FUV luminosity, using the assumption that the regions are SSPs. By comparing the ages to the SFHs, we found that most of the regions are entirely inconsistent with the SSP assumption. Furthermore, the ages often did not correspond to the main episodes of SF, and the masses were discrepant with the masses integrated from the SFHs by up to 2 orders of magnitude. These results call into question the practice of deriving ages and masses for populations that are not confirmed SSPs.

We identified SSP-like regions as regions which formed 90% or more of their mass over the past 100 Myr in a single age bin of their SFH. These regions accounted for 18% of our sample (6 of 33). Among this subset, we found discrepancies of 10 Myr in the ages and a factor of 3 – 4 in the masses derived from UV flux, most likely due to systematics in metallicity and extinction. We propose that these discrepancies represent realistic uncertainties in the SSP ages and masses, though the limited number of SSP-like regions in our sample makes the uncertainties difficult to determine. Finally, identification of the SSP-like regions was not possible from integrated FUV flux.

4.2 Modeling ultraviolet flux on sub-kpc scales and galactic scales simultaneously

We have used star formation histories (SFHs) to model the spectral energy distributions (SEDs) of over 9000 sub-kpc regions in M31 and produce detailed maps of synthetic UV flux across the entire area covered by the Panchromatic Hubble Andromeda Treasury (PHAT). This work is an extensive follow-up to the analysis of Simones et al. (2014), which involved only 33 ultraviolet (UV)-bright regions from a small portion of the galaxy. The SFHs were derived by Lewis et al. (2014) using F475W and F814W photometry from the PHAT survey. Both intrinsic and attenuated SEDs were derived from the SFHs using the Flexible Stellar Population Synthesis (FSPS) code. These were convolved with the Galaxy Evolution Explorer (GALEX) FUV and NUV response curves to obtain the synthetic intrinsic fluxes, $f_{X,\text{SFH},0}$, as well as the synthetic attenuated fluxes, $f_{X,\text{SFH}}$. All of the flux values were then assembled into an overall map, or mosaic, using Montage. The mosaic pixels corresponded to physical areas of $4.4 \times 10^4 \text{ pc}^2$. We constructed corresponding maps for the observed flux, $f_{X,\text{obs}}$, using GALEX Deep Imaging Survey (DIS) images.

The $f_{X,\text{SFH}}$ maps agreed with the $f_{X,\text{obs}}$ maps very well with respect to the broad morphology of M31, faithfully reproducing all of the main features brighter than $\sim 10^{-15} \text{ erg s}^{-1} \text{ cm}^{-2} \text{ \AA}^{-1}$. We found the log ratios of $f_{X,\text{SFH}}$ to $f_{X,\text{obs}}$ to be log-normally distributed with $\mu = 7.62 \times 10^{-3}$ and $\sigma = 2.37 \times 10^{-1}$ for FUV, and $\mu = -1.03 \times 10^{-1}$ and $\sigma = 1.59 \times 10^{-1}$ for NUV. The median flux ratios were 1.02 in FUV and 0.79 in NUV, with 68% confidence limits of 0.59 and 1.76 (FUV) and 0.55 and 1.14 (NUV). In both filters, the median ratio was within the confidence interval of 1, indicating that $f_{X,\text{SFH}}$ was consistent with $f_{X,\text{obs}}$ on average. Due to the small pixel areas, the primary source of the variance in the log flux ratios was most likely related to incomplete sampling of the IMF.

We found no obvious trends in the flux ratios with respect to environment, except for in the faintest, off-arm areas of the M31 where the variances in the flux ratios were noticeably larger. We conclude that fluxes may be successfully modeled from SFHs for any population in environments similar to M31. For our sub-kpc regions, we estimate the synthetic flux uncertainties to be $+0.74/-0.43$ and $+0.35/-0.24$ in FUV and NUV,

respectively. Results from previous work on UV-bright regions by Simones et al. (2014) were consistent with our results.

The overall agreement between the observed and synthetic fluxes is remarkable considering that our flux modeling procedure was dependent on several key assumptions. Specifically, we assumed an IMF, models describing stellar spectra and evolution, and an extinction model as well as an extinction curve. These form the foundation for much research in astronomy and encompass our current best understanding of stellar astrophysics and star formation. It is reassuring that we can use all of this knowledge to successfully recreate detailed maps of a galaxy from photometry in just two optical bands.

We used flux calibrations from Kennicutt (1998) with updates by Hao et al. (2011) and Murphy et al. (2011) to estimate SFRs based on observed UV flux, SFR_X . The $f_{X,\text{obs}}$ maps were first corrected for extinction using the synthetic attenuated and intrinsic fluxes. We also calculated the 100 Myr mean SFR from the SFHs, $\langle \text{SFR} \rangle_{100}$. We found that the faintest areas of M31 had the highest ratios of SFR_X to $\langle \text{SFR} \rangle_{100}$ and formed a linear tail feature in plots of the SFR ratio versus $\langle \text{SFR} \rangle_{100}$. These tails were the result of a distinct breakdown of the linear relationship between flux and SFR which underpins the flux calibration method. We estimated a conservative threshold of $\text{SFR} \sim 10^{-5} M_\odot \text{ yr}^{-1}$ below which flux calibration should not be used.

For the pixels above this threshold, we found the SFR ratios to be log-normally distributed with $\mu = -2.46 \times 10^{-1}$ and $\sigma = 2.61 \times 10^{-1}$ for FUV, and $\mu = 9.27 \times 10^{-2}$ and $\sigma = 2.33 \times 10^{-1}$ for NUV. The median ratios are 0.57 (FUV) and 1.24 (NUV), with 68% confidence limits of 0.31 and 1.04 (FUV) and 0.72 and 2.12 (NUV), indicating that SFR_X is consistent with $\langle \text{SFR} \rangle_{100}$ on average. As with the flux ratios, incomplete sampling of the IMF was the main source of the variance in the SFR ratios. We also considered deviations from solar metallicity as well as SFH variability, and found that they were far less important for the overall variances in the SFR ratios than IMF sampling.

Other than the faintest, off-arm areas which responsible for the tail feature in the SFR ratio distributions, there were no found no obvious trends in the SFR ratios with respect to environment. We determine that the flux calibration method is safely applicable to environments similar to M31, *but only as long as the resulting SFRs are greater*

than $\sim 10^{-5} M_{\odot} \text{yr}^{-1}$. We estimate the SFR uncertainties for our sub-kpc regions to be $+0.47/-0.26$ (FUV) and $+0.88/-0.52$ (NUV) times the true, underlying 100 Myr-mean SFR. The SFR_{FUV} uncertainty is rather less than the $+2.15/-0.88$ uncertainty previously found by Simones et al. (2014).

We also measured global SFRs for the entire PHAT survey area. The global $\langle \text{SFR} \rangle_{100}$ value was $0.30 M_{\odot} \text{yr}^{-1}$, while the UV flux-based values were $\text{SFR}_{\text{FUV}} = 0.22 M_{\odot} \text{yr}^{-1}$ and $\text{SFR}_{\text{NUV}} = 0.43 M_{\odot} \text{yr}^{-1}$. The flux-based global SFRs are consistent with the global $\langle \text{SFR} \rangle_{100}$ value to within the uncertainties derived from the SFR maps. However, the variances in the SFR ratios due to IMF sampling is expected to decrease for larger areas, so our estimated uncertainties should be considered firm upper limits when applied to galaxies. The global SFR ratios (flux-based to mean) are 0.73 and 1.43 for FUV and NUV, respectively. Why these ratios are larger than the median ratios above is not yet understood.

4.3 Future work

4.3.1 More precise quantification and attribution of uncertainties

The two studies presented here share some key similarities. First, they both show the importance of stochasticity in both the modeling of observed flux and in the estimation of SFRs. The large variations in the derived fluxes and SFRs with respect to their expected values due to incomplete IMF sampling significantly limited the precision to which each could be determined (more so in Chapter 3 than Chapter 2). While arguably not as important when considering galaxies as a whole, care must be taken when analyzing and comparing the flux content of stellar populations on much smaller scales.

Second, the work here demonstrates that sample design has a critical influence on the results of any given study. For example, the sample studied in Chapter 2 only included only a small subset of the UV-bright regions in one small portion of M31. It was not until the full PHAT dataset was considered in Chapter 3 that the unexpected nonlinearity between UV flux and SFR was found for SFRs below $\sim 10^{-5} M_{\odot} \text{yr}^{-1}$.

The PHAT photometry and the SFHs derived from it make up such an incredibly rich dataset that the work presented in this thesis is far from complete. An interesting

possibility for the future is to investigate more deeply the variance in the flux and SFR ratios discussed in Chapter 3. Specifically, an in-depth CMD analysis of the stellar populations behind each map pixel would lead to a better understanding of the degree to which IMF sampling really affects the total uncertainty in each data point. A simple census of the main sequence stars in each CMD would be a good starting point. A follow-up analysis involving models of stellar populations with different numbers of stars would help to determine the inherent uncertainty that can be expected for the fluxes and SFRs derived in Chapter 3. Any discrepancies between the total variances observed in the data and the expected contribution from incomplete IMF sampling alone could provide clues about other possible sources of uncertainty not yet recognized.

4.3.2 Putative flux ratio and SFR ratio outliers

A thorough investigation of the putative outliers in the flux and SFR ratio distributions would be another interesting topic for the future. It is unknown at this time whether the most discrepant data points are simply extreme cases of the same dispersion affecting all of the data, or if such points are genuine outliers. Similar to the analysis of IMF sampling proposed above, the simplest places to look for clues are the CMDs. It is certainly possible that a small subset of the putative outliers are genuine due to the contamination of foreground stars in their CMDs. Once identified, such stars could be cleaned from the photometry to improve the SFHs of Lewis et al. (2014), and presumably the synthetic fluxes and flux-based SFR estimates as well, leading to a more accurate characterization of the uncertainties involved in flux modeling and SFR estimation. The large discrepancies in the flux-based SFRs may also be explained by high variability in the derived SFHs. While such variability was not found to be important for M31 overall as discussed in Chapter 3, it was found in Chapter 2 to be a significant source of uncertainty in the flux-based SFRs of UV-bright regions. The only definitive answer to whether the SFR outliers are caused by non-constant SFHs is to look at their SFHs directly.

4.3.3 Synthetic flux and flux-based SFR uncertainties as a function of scale

Chapters 2 and 3 looked at flux modeling and SFR estimation on both sub-kpc scales and galactic scales. These represent the endpoints of a wide range of sizes, yet none of the intermediate scales (e.g., ~ 1 to 10 kpc) have been considered. It was shown in Chapter 2 that the uncertainties in both the synthetic fluxes and the estimated SFRs decreased with increasing area, presumably due to more complete IMF sampling and an overall averaging out of SFH variations. However, the sample was severely limited and it was not possible in that study to examine the trend for scales larger than ~ 1 kpc. In contrast, the maps presented in Chapter 3 are an ideal dataset for exploring quantitatively how the uncertainties in the synthetic fluxes and the flux-based SFRs decrease with area. By grouping the map pixels together into successively larger regions, a complete distribution of sizes ranging from sub-kpc through galactic scales can be studied.

4.3.4 Synthetic flux and flux-based SFR uncertainties as a function of environment

Another possibility is to group the map pixels by surface brightness and environment (or radius), as shown in the prototype sample in Figure ???. This would result in a two-dimensional sample where each region represents a much larger fraction of the total survey area than a single pixel, tempering the uncertainties due to IMF sampling. It would therefore be possible to investigate more precisely how different conditions within M31 influence the outcome of flux modeling and the agreement between flux-based SFRs and the derived SFHs. It might then be possible to use the resulting environment-specific uncertainties for UV flux analyses of more distant galaxies for which resolved stars are not available.

4.3.5 Infrared flux as a test of dust emission models and as a SFR indicator

Finally, the set of synthetic flux maps presented in Chapter 3 can be extended to include maps for other instrument/filter combinations. Perhaps the most interesting

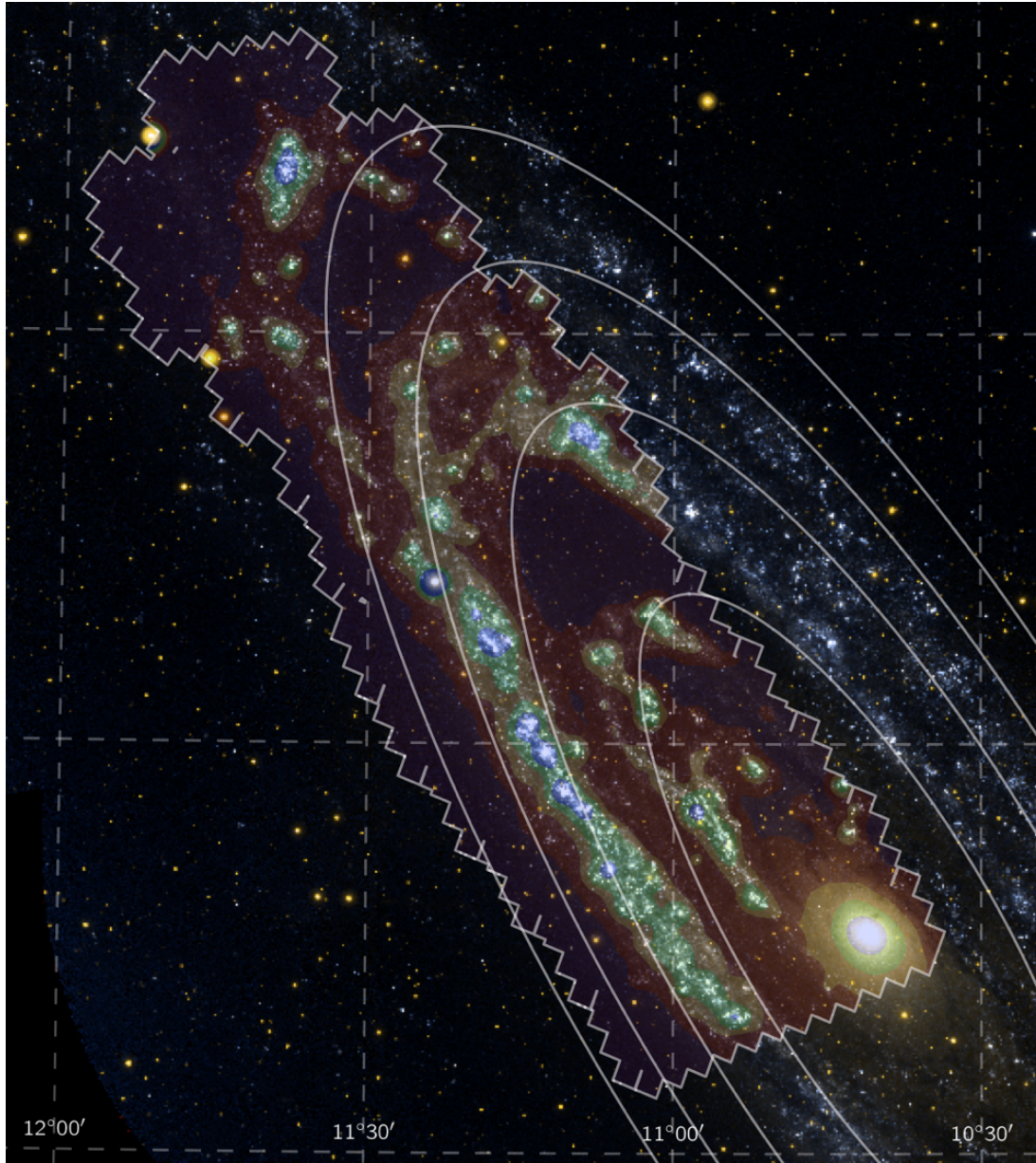


Figure 4.1 Two-dimensional prototype sample for future investigation of the accuracy of flux modeling and flux-based SFR estimation as a function of both surface brightness and galactocentric radius. This example shows the PHAT survey divided into five levels of FUV surface brightness (purple, red, orange, green, and blue shaded regions, from faintest to brightest) and again into five radial bins of approximately equal area.

choice would be to model the flux in M31 as seen through the $24\mu\text{m}$ channel of the Spitzer Space Telescope. Developing such a map would require an SED for the infrared (IR) dust emission in addition to the stellar SED described in Chapter 3. This would therefore present an opportunity to test the accuracy of different dust emission models in M31, e.g., the silicate-graphite-PAH model by Draine & Li (2007).

$24\mu\text{m}$ flux is also conspicuous tracer of star formation and therefore has been calibrated for predicting SFRs (see the review by Kennicutt & Evans, 2012, and references therein). The first interesting comparison with respect to the work presented in Chapter 3 would be between the UV flux-based SFRs and the $24\mu\text{m}$ flux-based SFRs in terms of how well they agree with the mean SFRs derived from the SFHs. So-called “hybrid” calibrations also exist, which predict SFRs using fluxes from multiple wavelengths. In principle, hybrid calibrations are more robust than their monochromatic counterparts because they account for more complex physics that processes the observed light. For example, the combination of FUV flux with $24\mu\text{m}$ flux accounts for both the direct starlight from massive stars and the starlight that is absorbed by dust and reradiated in the IR. The UV extinction correction is therefore built-in, in a sense, so the observed UV and IR fluxes can be used directly without modification. Comparing a map of hybrid FUV + $24\mu\text{m}$ flux-based SFRs with the mean SFH-based SFRs would be very interesting indeed, especially with respect to environments that are particularly dusty versus those that are not.

References

- Astropy Collaboration, Robitaille, T. P., Tollerud, E. J., et al. 2013, A&A, 558, A33
- Ballesteros-Paredes, J., Vázquez-Semadeni, E., Gazol, A., et al. 2011, MNRAS, 416, 1436
- Barmby, P., Huchra, J. P., Brodie, J. P., et al. 2000, AJ, 119, 727
- Barnes, K. L., van Zee, L., & Skillman, E. D. 2011, ApJ, 743, 137
- Bastian, N., Covey, K. R., & Meyer, M. R. 2010, ARA&A, 48, 339
- Berkhuijsen, E. M., & Fletcher, A. 2008, MNRAS, 390, L19
- Bianchi, L., Clayton, G. C., Bohlin, R. C., Hutchings, J. B., & Massey, P. 1996, ApJ, 471, 203
- Bianchi, L., Kang, Y. B., Efremova, B., et al. 2011, Ap&SS, 335, 249
- Bressan, A., Marigo, P., Girardi, L., et al. 2012, MNRAS, 427, 127
- Calabretta, M. R., & Greisen, E. W. 2002, A&A, 395, 1077
- Cardelli, J. A., Clayton, G. C., & Mathis, J. S. 1989, ApJ, 345, 245
- Conroy, C., & Gunn, J. E. 2010, ApJ, 712, 833
- Conroy, C., Gunn, J. E., & White, M. 2009, ApJ, 699, 486
- da Silva, R. L., Fumagalli, M., & Krumholz, M. 2012, ApJ, 745, 145
- da Silva, R. L., Fumagalli, M., & Krumholz, M. R. 2014, MNRAS, 444, 3275

- Dalcanton, J. J., Williams, B. F., Lang, D., et al. 2012, ApJS, 200, 18
- Dalcanton, J. J., Fouesneau, M., Hogg, D. W., et al. 2014, submitted
- de Vaucouleurs, G., de Vaucouleurs, A., Corwin, H. G., et al. 1995, VizieR Online Data Catalog, 7155, 0
- Dolphin, A. E. 2000, PASP, 112, 1383
- . 2002, MNRAS, 332, 91
- . 2013, ApJ, 775, 76
- Draine, B. T., & Li, A. 2007, ApJ, 657, 810
- Efremova, B. V., Bianchi, L., Thilker, D. A., et al. 2011, ApJ, 730, 88
- Elmegreen, B. G. 1999, ApJ, 515, 323
- Fitzpatrick, E. L., & Massa, D. 2007, ApJ, 663, 320
- Fumagalli, M., da Silva, R. L., & Krumholz, M. R. 2011, ApJ, 741, L26
- Girardi, L., Groenewegen, M. A. T., Hatziminaoglou, E., & da Costa, L. 2005, A&A, 436, 895
- Girardi, L., Williams, B. F., Gilbert, K. M., et al. 2010, ApJ, 724, 1030
- Gogarten, S. M., Dalcanton, J. J., Williams, B. F., et al. 2009, ApJ, 691, 115
- Gordon, K. D., Bailin, J., Engelbracht, C. W., et al. 2006, ApJ, 638, L87
- Hao, C.-N., Kennicutt, R. C., Johnson, B. D., et al. 2011, ApJ, 741, 124
- Hill, A. S., Benjamin, R. A., Kowal, G., et al. 2008, ApJ, 686, 363
- Hunter, J. D. 2007, Computing in Science and Engineering, 9, 90
- Johnson, B. D., Weisz, D. R., Dalcanton, J. J., et al. 2013, ApJ, 772, 8
- Kang, Y., Bianchi, L., & Rey, S.-C. 2009, ApJ, 703, 614

- Kennicutt, R. C., & Evans, N. J. 2012, ARA&A, 50, 531
- Kennicutt, Jr., R. C. 1998, ARA&A, 36, 189
- Kroupa, P. 2001, MNRAS, 322, 231
- Leitherer, C., Schaerer, D., Goldader, J. D., et al. 1999, ApJS, 123, 3
- Leroy, A. K., Bigiel, F., de Blok, W. J. G., et al. 2012, AJ, 144, 3
- Lewis, A. R., Dalcanton, J. J., Dolphin, A. E., Weisz, D. R., & Williams, B. F. 2014, preprint
- Marigo, P., Girardi, L., Bressan, A., et al. 2008, A&A, 482, 883
- Martin, D. C., Fanson, J., Schiminovich, D., et al. 2005, ApJ, 619, L1
- Massey, P., Olsen, K. A. G., Hodge, P. W., et al. 2006, AJ, 131, 2478
- McConnachie, A. W., Irwin, M. J., Ferguson, A. M. N., et al. 2005, MNRAS, 356, 979
- McQuinn, K. B. W., Skillman, E. D., Mitchell, N. P., & Dolphin, A. E. 2014, preprint
- Morrissey, P., Conrow, T., Barlow, T. A., et al. 2007, ApJS, 173, 682
- Murphy, E. J., Condon, J. J., Schinnerer, E., et al. 2011, ApJ, 737, 67
- Oliphant, T. E. 2007, Computing in Science and Engineering, 9, 10
- Pérez, F., & Granger, B. E. 2007, Computing in Science and Engineering, 9, 21
- Salim, S., Rich, R. M., Charlot, S., et al. 2007, ApJS, 173, 267
- Shetty, R., Glover, S. C., Dullemond, C. P., & Klessen, R. S. 2011, MNRAS, 412, 1686
- Simones, J. E., Weisz, D. R., Skillman, E. D., et al. 2014, ApJ, 788, 12
- Tully, R. B. 1994, VizieR Online Data Catalog, 7145, 0
- Westera, P., Lejeune, T., Buser, R., Cuisinier, F., & Bruzual, G. 2002, A&A, 381, 524